Contribution of locally tangential CMB-mantle flow and cold-source subducting plates to ULVZ formation and morphology

Jie Xin[1], Huai Zhang[1], Yaolin Shi[2], Felipe Orellana-Rovirosa[3], Zhen Zhang[4], and Yimin Jin[5]

[1]University of Chinese Academy of Sciences
[2]University of Chinese Academy of Science
[3]Southern University of Science and Technology
[4]Institute of Geology, China Earthquake Administration
[5]Institute of Geophysics, China Earthquake Administration

November 22, 2023

Abstract

Ultra-low velocity zones (ULVZs) above the core-mantle boundary (CMB) are significant structures that connect the lowermost mantle and outer core. As "thin patches" of dramatically low seismic-wave velocity, they are occasionally found near the base of mantle plumes and in-or-near high seismic-wave speed regions above the CMB. The causes of their morphological distribution and geodynamics remain unclear, and simulation results of high-density melts diverge from seismic observations. We introduced a two-dimensional time-dependent Stokes two-phase flow (with melt migration) numerical model to investigate the formation and morphological characteristics of ULVZs caused by CMB-mantle tangential flows and a neighboring cold source (subducted plate). We discovered that (a) the participation of cold sources with temperature differences between ~4000 K at the plume central regions to $<$~3900 K at the plume-cooling mantle region, separated by horizontal distances of approximately 100 ($\pm<50$) km are necessary for the stable existence of dense melts with mass-density difference $>+1$–2% (even +10%) with respect to the surrounding mantle; additionally, (b) an enhanced tangential flow coincident with the internal reverse circulation within the broad plume base (with speeds >3 times the lowermost-mantle characteristic flow speed) are necessary for higher aspect-ratio-morphology lenses compatible with seismic observations. The CMB-mantle tangential flow and/or outer-core interacting with CMB-topography may help generate mega-ULVZs, particularly if they appear along the edges of large low-shear-wave-velocity provinces (LLSVPs) and in/near high seismic-speed "cold" zones. Thus, we infer that a strong link exists between ULVZ morphology and the dynamic environment of the lowermost mantle and uppermost outer core.

Hosted file

`979226_0_supp_11582248_s3zxyl.docx` available at https://authorea.com/users/557382/articles/686759-contribution-of-locally-tangential-cmb-mantle-flow-and-cold-source-subducting-plates-to-ulvz-formation-and-morphology

Contribution of locally tangential CMB-mantle flow and cold-source subducting plates to ULVZ formation and morphology

Jie Xin[1], Huai Zhang[1*], Yaolin Shi[1], Felipe Orellana-Rovirosa[2], Zhen Zhang[3], Yimin Jin[4]

[1]Key Laboratory of Computational Geodynamics, College of Earth and Planetary Sciences, University of Chinese Academy of Sciences, Beijing 100049, China

[2]Department of Ocean Science and Engineering, Southern University of Science and Technology, Shenzhen 518055, China

[3]State Key Laboratory of Earthquake Dynamics, Institute of Geology, China Earthquake Administration, Beijing 100029, China

[4]Institute of Geophysics, China Earthquake Administration, Beijing 100081, China

Key Points:

- The stable presence of high-density partial melts as a cause of ultra-low velocity zones requires involvement of cold subducting plates.

- The morphology of stable ULVZs is related to the direction and magnitude of the local core-mantle boundary (CMB)-mantle flow.

- Flow driven by CMB topography interacting with the outer core may help form mega-ULVZs and ULVZs in the seismic-wave cold zone.

Abstract

Ultra-low velocity zones (ULVZs) above the core-mantle boundary (CMB) are significant structures that connect the lowermost mantle and outer core. As "thin patches" of dramatically low seismic-wave velocity, they are occasionally found near the base of mantle plumes and in-or-near high seismic-wave speed regions above the CMB. The causes of their morphological distribution and geodynamics remain unclear, and simulation results of high-density melts diverge from seismic observations. We introduced a two-dimensional time-dependent Stokes two-phase flow (with melt migration) numerical model to investigate the formation and morphological

characteristics of ULVZs caused by CMB-mantle tangential flows and a neighboring cold source (subducted plate). We discovered that (a) the participation of cold sources with temperature differences between ~4000 K at the plume central regions to <~3900 K at the plume-cooling mantle region, separated by horizontal distances of approximately 100 (±<50) km are necessary for the stable existence of dense melts with mass-density difference >+1–2% (even +10%) with respect to the surrounding mantle; additionally, (b) an enhanced tangential flow coincident with the internal reverse circulation within the broad plume base (with speeds >3 times the lowermost-mantle characteristic flow speed) are necessary for higher aspect-ratio-morphology lenses compatible with seismic observations. The CMB-mantle tangential flow and/or outer-core interacting with CMB-topography may help generate mega-ULVZs, particularly if they appear along the edges of large low-shear-wave-velocity provinces (LLSVPs) and in/near high seismic-speed "cold" zones. Thus, we infer that a strong link exists between ULVZ morphology and the dynamic environment of the lowermost mantle and uppermost outer core.

Plain Language Summary

The ultra-low velocity zones (ULVZs) above the core-mantle boundary (CMB) are thin patch structures of rapidly decreasing seismic-wave velocity located at the base of the mantle plume and in the seismic-wave high-speed "cold" zone. However, the cause of their formation and morphology remains unclear. We introduced a numerical model to investigate the criteria for the stable existence and formation of a high-density melt that is consistent with the observations. By modifying the model bottom boundary conditions, we introduced the effects of the CMB-mantle flow and subducting plates as cold source. Based on our findings, the stable existence of high-density melting necessitates the involvement of a cold source with a lateral temperature difference between ~4000 K in the central region of the plume and <~3900 K in the plume-cooling intermediate mantle region. ULVZs with flat top and sharp edges require a higher CMB-mantle tangential flow than in the lowermost mantle. Thus, the flow associated with the CMB topography gradient may be involved in forming ULVZs, particularly when they are spread at the superplume margins and in the seismic-wave "cold" zone. The ULVZs morphology is more closely related to the dynamic environment of the lowermost mantle and uppermost outer core.

1. Introduction

The core-mantle boundary (CMB) is the interface between the metallic-liquid outer core and the solid oxide mantle, which is an important region for heat and mass exchange on Earth. The structural and dynamical characteristics of the CMB are affected by strong physical differences such as density (mantle: ~5500 kg·m^{-3}, core: ~9900 kg·m^{-3}) and particularly viscosity (mantle: >10^{12} Pa·s, outer-core: <10^{-1} Pa·s) (J. W. Hernlund & McNamara, 2015). In ultra-low velocity zones (ULVZs), which are 5–40 km-thick zones above the CMB, the seismic wave velocity is significantly decreased locally (~10% for P-waves and ~30% for S-waves) (Garnero et al., 1998). The ULVZs are an important structure connecting the lowermost mantle to the core, similar to the key intermediary crust between the mantle and surface (J. W. Hernlund & McNamara, 2015). From the seismic waves that pass through the core (e.g., SPdKS, PKKP, and PKP), as well as reflection (ScS, ScP, and PcP), diffraction (Pdiff and Sdiff), and scattering at the CMB (Dehant et al., 2022; Yu & Garnero, 2018), it is believed that ULVZs with "thin patches" are not globally distributed. Smaller ULVZs have a lateral extent of less than 100 km, larger mega-ULVZs can extend approximately 1000 km, and most have a large aspect ratio (Table 1). Many ULVZs are located in the center and/or at the margins of large low-shear-wave-velocity provinces (LLSVPs), but a good fraction are still found in/close-to the high seismic-speed "cold zone" (M. Li et al., 2017; Yu & Garnero, 2018) (Figure 1). Less than 20% of the CMB has been explored for ULVZs, owing to the observational resolution limitations (Z. Li et al., 2022; Rost et al., 2010). The locations of certain ULVZ images are thought to be associated with convergent regions at the mantle plume base (Dannberg et al., 2021), where ULVZs may be associated with the topography of the CMB at certain wavelengths through gravitational balance (Heyn et al., 2020; Stein et al., 2020). The size and morphology of ULVZs determined from seismic observations, together with well-constrained high-density contrast, can provide insights into the dynamics and properties of the lower mantle (Rost et al., 2005), genesis of LLSVPs (Garnero et al., 2016), and nature of global mantle convection (McNamara, 2019), even providing constraints on outer-core dynamics and the geodynamo (Buffett, 2016; Deschamps & Li, 2019).
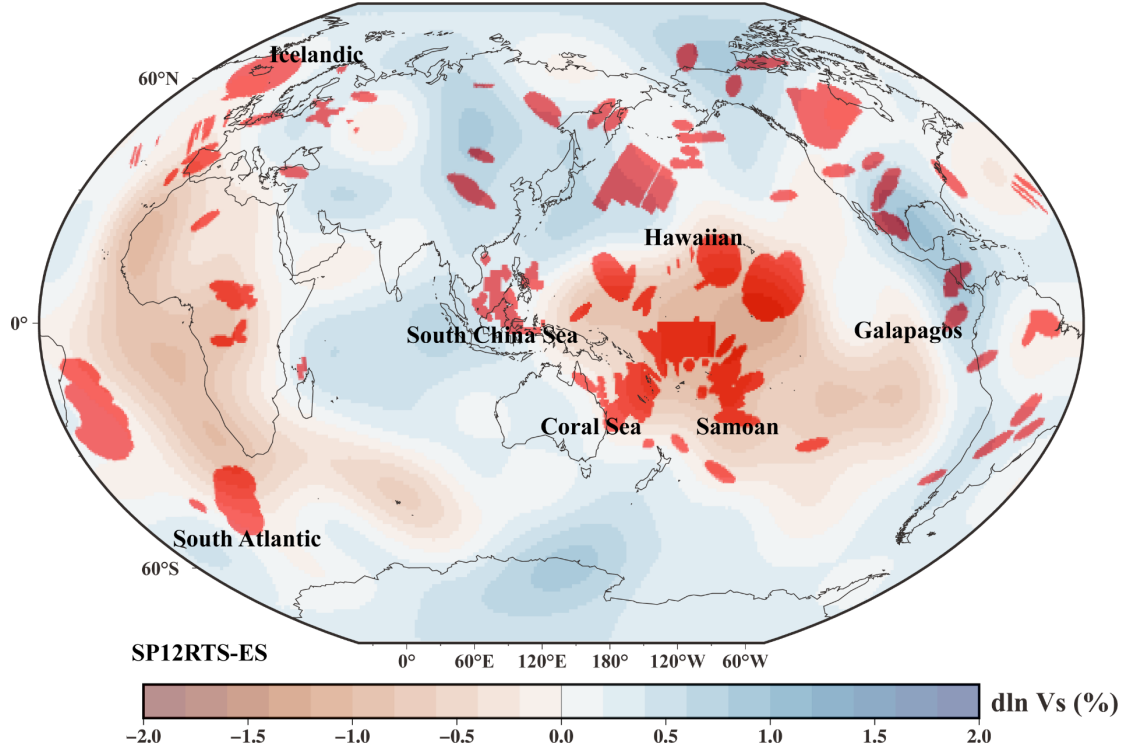
Figure 1. Global distribution of ULVZs. Red areas represent the detected ULVZ locations at/above the CMB; data from the seismic observations are summarized from (Yu & Garnero, 2017). The background color represents the shear wave velocity anomalies at 2800 km depth from the tomography model SP12RTS (Koelemeijer et al., 2016). Most area-fractions of ULVZs are located in and around low (to null) seismic-speed anomaly regions, but 30–40% of ULVZs are found in/close-to blueish, high seismic-speed "cold" regions.

Table 1. Parameters of ULVZs with good morphological constraints.

Case	Height (km)	Average lateral range/2 (km)	Aspect ratio (lateral range/2/height)	Reference
Hawaiian	30	500	16.7	(Jenkins et al., 2021)
Galapagos	20	300	15.0	(Cottaar et al., 2022)
Icelandic	15	400	26.7	(Yuan & Romanowicz, 2017)
Samoan	15	260	17.3	(Thorne et al., 2013)
Coral Sea	20	350	17.5	(Jensen et al., 2013)

South China sea	10	180	18.0	(Jensen et al., 2013)
South Atlantic	10	90	9.0	(Vanacore et al., 2016)

However, the cause of ULVZs remains controversial. It is believed that ULVZs arise from partial melting and/or chemical component anomalies, the latter possibly from early basal magma ocean crystallization residuals (Labrosse et al., 2007; Pachhai et al., 2022), core-mantle material reactions (Brandon & Walker, 2005; Kanda & Stevenson, 2006; Otsuka & Karato, 2012), and materials from subduction (Dobson & Brodholt, 2005). In most numerical simulations of the lowermost mantle, thermochemical piles have the same rheology as the background mantle (McNamara, 2019), and the ULVZs are a layer of dense chemical components (Beuchert & Schmeling, 2013; Pachhai et al., 2022). Based on seismic observations of the high-aspect-ratio low-velocity zone characteristics (Table 1) and constraints on the melt morphology and CMB topography obtained from numerical simulations (Deschamps & Li, 2019; John W. Hernlund & Tackley, 2007), researchers have found that the melt mass density that fits the observational constraints must be larger than that of the surrounding mantle phase. However, an excessively high melt density can lead to melt accumulation at the CMB. According to the equilibrium process of the melt layer under the stirring effect of mantle flow, a maximum difference of +50 kg·m^{-3} (approximately +1%) in melt-solid density difference is tolerated (John W. Hernlund & Jellinek, 2010). Based on the two-phase flow model (Dannberg & Heister, 2016) and FeO-MgO-SiO$_2$ pseudo-binary material systems (Boukaré et al., 2015), Dannberg et al. (2021) thoroughly examined the role of partial melting in the origin of ULVZs. They discovered that the tolerated melt density difference can reach approximately +120 kg·m^{-3} (~+2%) (Dannberg et al., 2021), but non-localized and high aspect-ratio melting layers were observed. Considering the seismic observations close to +10% density difference (McNamara et al., 2010; Rost et al., 2005), one question of interest is whether it is possible to enlarge the melt-solid density difference to a higher range (ρ_{melt}-ρ_{solid} ≳+(50–120) kg·m^{-3}, i.e., (ρ_{melt}-ρ_{solid})/ρ_{solid} >+1–2%) while the ULVZs melt layer remains

stable. What is the mechanism of the melt layer formation with a high aspect ratio observed in the current seismic observations? Why do certain ULVZs appear in/around high seismic-speed "cold" zone, and does the morphology and distribution of ULVZs indicate the involvement of additional dynamical mechanisms regarding lowermost mantle flow?

Most previous studies modeled the CMB as a temperature-isothermal velocity-free-slip boundary. Conversely, the CMB region may have resulted from a combination of hot and light mantle plume, dense thermochemical piles, and cold and dense subducting/subducted plates (Hansen & Yuen, 1988; Lay et al., 2008). Based on the waveform fitting results of the ScS phase, the formation of ULVZs may also be related to the thermal effects caused by the subduction of slabs and nearby high-velocity zones (Fan & Sun, 2021; Zhao et al., 2017). On the one hand, the presence of a subducting plate pushes low-viscosity material to move, deform and perhaps steepen the boundary of the LLSVPs and/or ULVZs (McNamara & Zhong, 2005; Sun et al., 2019), suggesting that the subducting plates have an effect on the genesis and morphology of the ULVZs. On the other hand, the role of the core side on the ULVZs should also be considered, such as the process of the outer core material penetrating the mantle under dynamic pressure and collapsing with gravitational diffusion (Lim et al., 2021). At the top of the outer core, studies using seismic observations (Helffrich & Kaneshima, 2010), geomagnetic observations (Buffett, 2014), and geodynamo models (Olson et al., 2017; O'Rourke & Stevenson, 2016) suggest the presence of an ~100–400 km-thick temperature and/or component-stabilized stratified layer (Fearn & Loper, 1981; Mound et al., 2019; van Tent et al., 2020), which affects thermal, chemical, and momentum exchange through the CMB (J. W. Hernlund & McNamara, 2015). Therefore, we suggest altering the velocity and temperature bottom boundary conditions of the model to introduce and incorporate the impact of cold subducting plates and the CMB-mantle tangential flow. This allowed us to study the spatial relationships of the corresponding high-density melt ULVZs in relation to hot and cold sources and provide some constraints on the plausible dynamic conditions at the CMB and the uppermost outer core.

2. Model setup

2.1. governing equations

We used the finite element software ASPECT (2.4.0) to solve the compressible two-dimensional (2D) Stokes viscous two-phase flow equation (1–4) as well as the temperature field advection-diffusion equation (5) with heat source terms from shear heating, adiabatic heating, and latent heat change from melting/freezing (Bangerth et al., 2022; Dannberg & Heister, 2016; McKENZIE, 1984).

$$\frac{\partial}{\partial t}\left[\rho_f\phi\right] + \nabla\cdot\left[\rho_f\phi\boldsymbol{u}_f\right] = \Gamma \tag{1}$$

$$\frac{\partial}{\partial t}\left[\rho_s(1-\phi)\right] + \nabla\cdot\left[\rho_s(1-\phi)\boldsymbol{u}_s\right] = -\Gamma \tag{2}$$

$$\phi(\boldsymbol{u}_f - \boldsymbol{u}_s) = -\frac{k_\phi}{\eta_f}(\nabla p_f - \rho_f\mathbf{g}) \tag{3}$$

$$-\nabla\cdot\left[2\eta\dot{\varepsilon} + \xi(\nabla\cdot\boldsymbol{u}_s)\mathbf{1}\right] + \nabla p_f = \bar{\rho}\boldsymbol{g} \tag{4}$$

$$\bar{\rho}C_p\left(\frac{\partial T}{\partial t} + \boldsymbol{u}_s\cdot\nabla\mathrm{T}\right) - \nabla\cdot k\nabla\mathrm{T} = 2\eta(\dot{\varepsilon_s}:\dot{\varepsilon_s}) + \alpha T(\boldsymbol{u}_s\cdot\nabla p_s) + T\Delta S\Gamma \tag{5}$$

We used the compositional advection equation (6) for porosity and depletion to represent the melt migration process.

$$\frac{\partial C_i}{\partial t} + \boldsymbol{u}_s\cdot\nabla C_i = \Gamma^i \tag{6}$$

where subscript f denotes fluid/melt, subscript s denotes solid, ϕ is the porosity/melt fraction, and $\bar{X}$ denotes the averaged quantities $\bar{X} = (1-\phi)X_s + \phi X_f$. ρ is the density, $\mathbf{u}$ is the velocity, Γ denotes the melt rate given by the compositional equation reaction term, and k_Φ, η, p, $\boldsymbol{g}$, $\dot{\varepsilon}$, and ξ are the permeability coefficient, shear viscosity, pressure, gravitational acceleration, strain rate, and bulk viscosity associated with material dilatation /compaction, respectively. In equation (5), C_p, T, k, and α are the specific isobaric heat capacity, temperature, thermal conductivity, the coefficient of thermal expansion, respectively. S is the entropy owing to the release or consumption of latent heat.

2.2. material model

We simplified the material parameters of the following models to describe the

differences in the melt-solid physical properties in terms of the porosity and depletion of the compositional field, in addition to utilizing the "Dannberg" model parameters as the reference model for comparison (Dannberg et al., 2021). The detailed material parameters are as follows:

Table 2. Material properties of the numerical models.

parameter	value	unit
Melting time scale	10^3	yr
depletion [a]		
Depletion density change	-180	kg·m^{-3}
Depletion solidus change	216	°K
Maximum Depletion viscosity change	10^4	——
viscosity		
Reference bulk viscosity ξ_{ref}	10^{23}	Pa·s
Reference melt viscosity $\eta_{f,\,ref}$	10	Pa·s
Reference shear viscosity η_{ref}	10^{23}	Pa·s
Exponential melt weakening factor	23	——
initial melt state		
Pressure solidus change ΔT_p	-10^{-8}	Pa^{-1}
Surface solidus $T_{sol,0}$	5100	K
Difference between liquidus and solidus T_{liquid}-T_{solid}	1900	K
permeability		
Reference permeability $k_{\Phi,\,ref}$	5×10^{-12}	m^2
Gravity acceleration $\boldsymbol{g}$	10.68	m·s^{-2}
density		
Reference melt density $\rho_{f,\,ref}$	5800	kg·m^{-3}
Reference solid density $\rho_{s,\,ref}$	5500	kg·m^{-3}
Melt compressibility	1.6×10^{-12}	Pa^{-1}
Solid compressibility	1.6×10^{-12}	Pa^{-1}
thermal dependence		
Reference temperature T_{ref}	298	K

Reference specific heat $C_{p,\,ref}$	1230	$J \cdot kg^{-1} \cdot K^{-1}$
Thermal conductivity k	8.5	$W \cdot m^{-1} \cdot K^{-1}$
Thermal expansion coefficient α	1×10^{-5}	K^{-1}
Thermal viscosity exponent	10	——
Thermal bulk viscosity exponent	10	——

[a] Based on an approximate estimate from the Dannberg model setup.

When a phase change occurs,

$$\phi_{equilibrium} = \frac{T - T_{sol}}{T_{liq} - T_{sol}} \tag{7}$$

$$T_{sol} = T_{sol,0} + \Delta T_p p + \Delta T_c C_{depletion} \tag{8}$$

where $C_{depletion}$ is composition depletion, and $\Delta T_c = 200\ °K$.

Here, the first parameter, the melting time scale, was set to be smaller than the advection time step to accurately resolve the melting/freezing process. The difference in the Fe-Mg distribution in the solid melt described by depletion (indicating the residue after melt migration) leads to variations in density and melt fraction. We refer to the physical parameters of the "Dannberg" model and let distribution coefficient $K_D = \frac{X_{Fe}^S X_{Mg}^l}{X_{Fe}^l X_{Mg}^S}$ remains constant (0.23) during the model simulation. We do not explore the viscosity change in this model; therefore, we keep the "exponential melt weakening factor" fixed, making its shear viscosity near the lowermost mantle 10^{19}–10^{22} Pa·s (Ricard, 2015). The three parameters of the initial melt state describe the initial and subsequent melting area. Combined with the geothermal line, we created a model in the initial stage ~15 km thick, with a maximum value of 0.16. The Clapeyron slope employed here was negative (Beuchert & Schmeling, 2013), and we investigated the impact of positive and negative slopes separately in Section 4.2. We used the same compression coefficient for both the solid and melt to conveniently regulate the variation in the melt-solid density and only altered the reference density during the subsequent study. The specific heat changes in the model with the temperature and melt fraction. Temperature, pressure, and melt fraction affect the latent heat in the heat source term.

A 2D Cartesian box model with dimensions 600 km (horizontal) × 200 km (vertical) was used to model the lowermost mantle (Figure 2). The initial temperature profile was adiabatic and a temperature perturbation (before melt migration was +50 K, after which it was +10 K) was continuously applied at the bottom center of the model (0 km) to trigger a mantle plume. The porosity and depletion represented by the compositional field were both zero in the initial stage.

As shown in Figure 2, our computational model is symmetric about x = 0 (the central vertical line). In the real Earth, different regions near the mantle plume do not have the same thermal-chemical structure (such as subducted plates), as prescribed here. The reason we continue to use the a full-symmetrical model, rather than using just half of it (any of the sides x≤0 or x≥0), is to verify and illustrate the accuracy of the results from the numerical modeling, that is, that any apparent asymmetry is beyond the scope of our discussion. In addition, in later parts of this article, we extract the symmetric part of the computation output by taking the averages (arithmetic mean) of approximately x=0 for selected variables; the symmetric part should have smaller numerical errors.
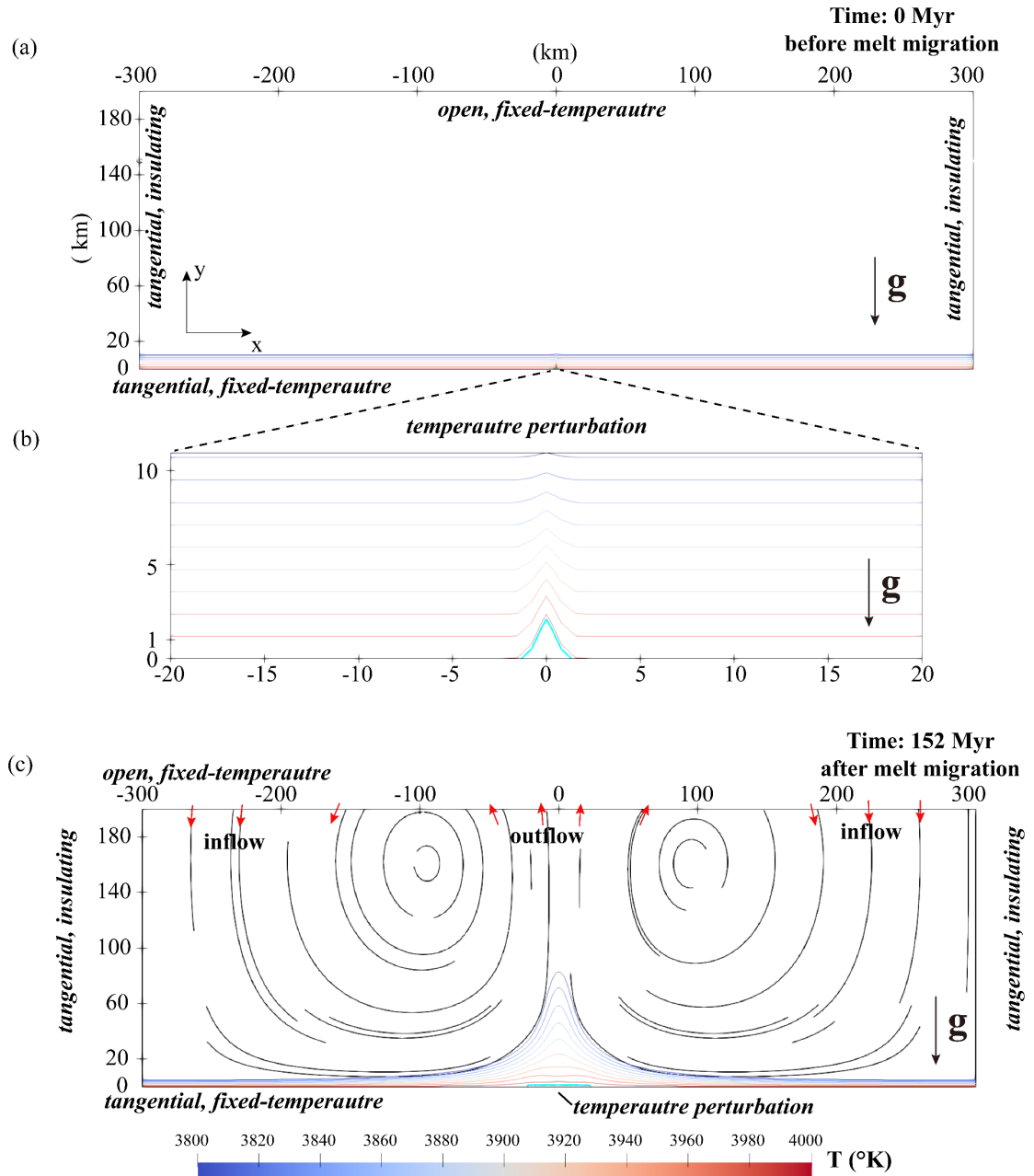
Figure 2. Reference model setup. (a) Initial condition setup before melt migration (150 Myr). The surrounding symbols represent boundary conditions, where the reference model has a fixed (in time) temperature (here 4000 K) and tangential flow at the bottom boundary. The colored contour denotes the partial temperature distribution (3800–4000 K), where a sustained temperature perturbation (before melt migration, the maximum is +50 K, after is +10 K) is applied in the bottom center to trigger the mantle plume. **(b) The initial temperature perturbation closeup.** The perturbation maximum decays exponentially as the square of the distance from the bottom boundary center. **(c) Setup after melt migration (150 Myr).** The black streamlines represent the (solid) velocity direction, and sparseness has no special meaning. Red arrows represent the flow direction at the top open boundary. The blue line represents the contour of the fixed melt fraction (0.16).

2.3. Boundary condition

The left and right boundaries of the model are adiabatic and tangential flow boundaries, that is, free-slip (zero shear stress) and no-flow-through (zero normal velocity). The upper boundary was a fixed temperature and open boundary. The bottom boundary represents the fixed (in time) CMB with a pressure of 136 GPa and temperature of 4000 K (Dziewonski & Anderson, 1981), except for a sustained temperature perturbation at the center triggering the mantle plume. The bottom velocity boundary of the reference model is also a tangential flow boundary (Figure 2). Throughout this article, we refer to the velocity of the solid phase of the mantle when we describe the velocity in the model or in the real Earth mantle. Exceptions regarding the melt are explicitly stated. We nevertheless state 'solid velocity' in a few crucial cases.
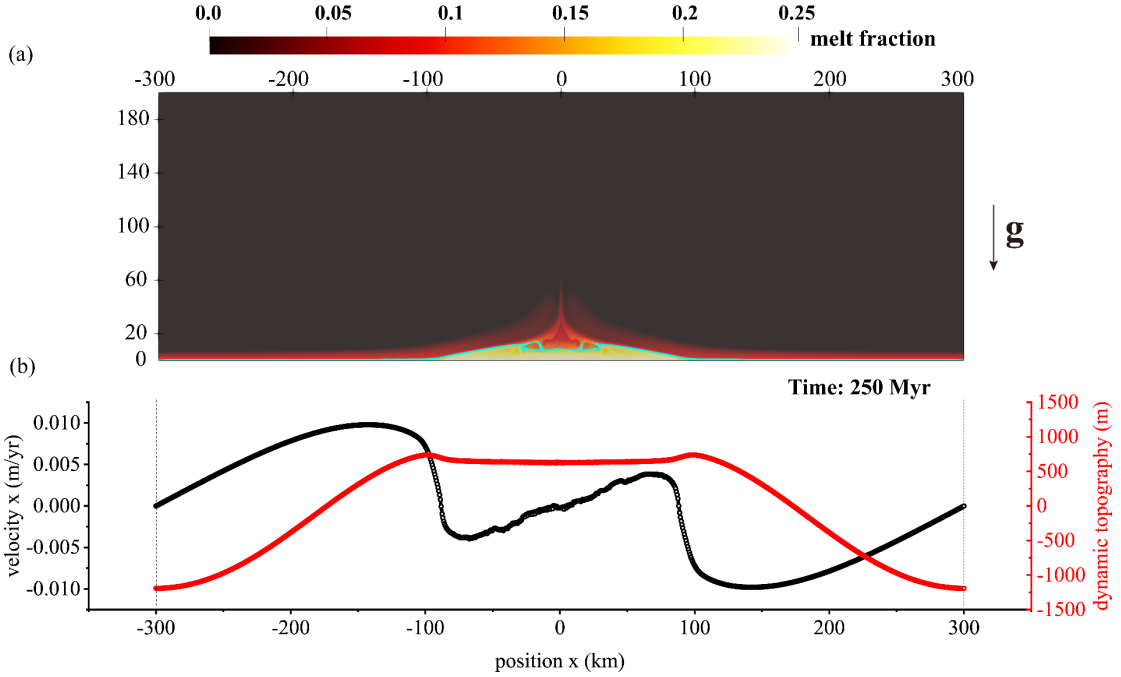

Figure 3. (a) Melt fraction of the reference model ($\rho_{melt} - \rho_{solid} = +300$ kg·m³) 250 Myr after the initial condition (which is the time when the subsequent experimental model boundary parameters start to change). The blue line is the same as in Figure 2. (b) Model tangential velocity (black, along x-direction) and dynamic topography (red) distribution on the bottom boundary (CMB) at 250 Myr; note, we use the normal stress σ_{rr} as the equivalent for dynamic topography $h=\sigma_{rr}/[(\mathbf{g}\cdot\mathbf{n})\cdot(\rho-\rho_{core})]$) (Bangerth et al., 2022; Mckenzie et al., 1974). The model is, within numerical errors, symmetric with aspect to its centerline, with velocities and topography mirrored with respect to x=0.

The subsequent model boundary setting is based on the following.

2.3.1 Bottom boundary temperature

As mentioned in section 1, considering the heat-mass exchange at the CMB, we introduced the influence exerted by a cold source, such as subducting/subducted plates in the mantle, by setting a nonuniform mantle-bottom temperature boundary in the following model. Given that several ULVZs are located in seismic cold zones and at the edges of the Pacific or Afro-Atlantic LLSVPs (Garnero & McNamara, 2008), this suggests the presence of long-lasting cold sources. According to previous estimates of the lateral temperature variation in the lowermost mantle, the peak temperature difference between the mantle plume base and the surrounding lower mantle is not expected to be greater than 500 K (Davies et al., 2015; Deschamps & Li, 2019; Solomatov & Moresi, 2002; WATSON & McKENZIE, 1991). Although the lateral temperature variation at the top of the outer core does not exceed ~1 K (Mound et al., 2019), considering the stronger heat exchange within the outer core (owing to high thermal conductivity) than in the mantle, and in reference to the ±100 K setting found in previous work (Aubert et al., 2007), we set the peak lateral temperature difference between cold source location and normal ambient mantle at the bottom boundary to be 0, -100, -200, and -300 K. This would result in both a cooling effect on the local ambient mantle outside the mantle plume and cooling of the plume itself within a few tens of kilometers (<50 km) of the plume edge (Figure S1).

2.3.2 Bottom boundary velocity

For the velocity boundary, as in previous studies, we set a velocity-free-slip bottom boundary in the reference model (Figure 3). Under the zero-shear stress assumption, this leads to a CMB velocity generated entirely by mantle convection and gravitational action. However, previous studies have shown that this cannot sufficiently explain the high-density ULVZ morphology distribution (Section 1). Therefore, in the following section, we introduce other factors that contribute to the CMB velocity. Previous observations have revealed that dense material piles within the plume spontaneously form an internal reverse circulation, allowing the mantle flow along the CMB to

converge at the edge of the plume (Kellogg & King, 1993; Luo et al., 2001; McNamara, 2019). The drag force driven by the CMB topography, as well as the net horizontal electromagnetic force from the outer core (Dehant et al., 2022; Glane & Buffett, 2018), may affect the internal reverse circulation.

In the first part of this study (Section 3.1), our reference model, utilizing the CMB dynamic boundary conditions (BCs) of zero flow-through and zero shear stress, found a self-consistent convecting-mantle flow that contained and produced a dynamically consistent mantle velocity field at the CMB. In the second part (after Section 3.1), we prescribed/imposed Dirichlet BCs on the mantle velocity field at the CMB.

For this Dirichlet velocity field, we firstly note that the velocity distribution and speeds of the mantle mass elements at the CMB and the proper Dirichlet boundary velocity field, although seemingly somewhat arbitrary or artificial, are based on the dynamically consistent mantle flow computed in the reference model. Therefore, this CMB-mantle Dirichlet velocity field adequately imitates the resulting velocity field of a system in which the velocity is a consequence of self-consistent pressure and viscous forces operating during convection, that is, the convecting-mantle pressure field and viscous field horizontal forces move the mantle-CMB mass particles at those velocities. Thus, in principle, our second-part model contains Dirichlet boundary velocities that are approximately consistent with the reasonable model settings.

Additionally, if externally driven velocities are considered, the liquid iron outer core may exert forces on the lowermost mantle, affecting its velocity field. We quickly review that (a) the CMB topography and (b) possible magnetic forces can potentially have non-negligible effects on the velocity field at the mantle CMB.

Here, we varied the bottom tangential traction to experiment with how large a force source is required to produce localized CMB-mantle flow velocities of a magnitude comparable to the lower mantle characteristic convective speed (~1 cm/yr (Flament et al., 2017)). The bottom boundary traction model simulations show that to reach velocities of that magnitude, based on the outer-core-flow drag force formula in plane laminar flow $F_{drag} = c_D \frac{\rho}{2} u^2 b l$ (Schlichting & Gersten, 2017), where at a modest

Reynolds number (Re~10^7–10^8), considering outer-core parameters η=0.01 Pa·s, u=5×10^{-4} m/s (Jones, 2015), and l as the half plume width, the drag force must be increased by a factor of 10^5 (Figure S2). The core-mantle mass exchange layer (a region where chemical exsolution is upward from the outer core and downward from the mantle, and accumulated material may reside for different amounts of time) at the uppermost outer core beneath the CMB may have a higher viscosity, and the resulting local drag effect is facilitated by CMB topography. Given length l of x × 10^1–10^2 km, and taking drag coefficient c_D = 24/Re at a small Reynolds number (< 10^3) where F_{drag} = $12\eta u l$, a sufficient non-essential condition is that the thin mass exchange layer viscosity could reach 10^3–10^5 Pa·s (an intermediate value between outer-core and lowermost mantle).

Based on these considerations, in the subsequent parts of this study, we established a Dirichlet-type velocity BC at the CMB, whose horizontal-component distribution is prescribed to have the form of the velocity distribution obtained in the free-slip-BC simulation (Figure 3) and zero in the vertical y-direction, meaning that this Dirichlet velocity field simulates the resultant velocity field dynamically obtained from the tangential BC, which is consistent with the internal reverse circulation and, furthermore, with the CMB dynamic topography. Naturally, applying traction ('Neumann' BC for velocity) at the bottom boundary produces somewhat different results than applying "Dirichlet" BC for velocity (see the bottom horizontal velocity in Figures 3b and S2). Comparison of model outputs having different types of bottom conditions for the velocity field, as seen for example in the aforementioned figures, shows differences in melt morphology between those pertaining to prescribed traction and/or velocity BC models (Figure S3).

However, to focus on the direct effects of CMB-mantle flow, we begin with the model of applied horizontal velocity that is more closely aligned with the reference free-slip-BC model.

2.4. Other model settings

To maintain calculation stability at the beginning of modeling, we divided the simulation process into two stages (Dannberg et al., 2021). In the initial stage of 0–150

Myr, we prevented melt migration from occurring by increasing the melt scaling factor (10^{20}, equivalent to virtually reducing the permeability coefficient to 0) and allowed the mantle plume to form under the initial temperature perturbation. We applied melt migration in the second stage (i.e., a smaller melt scaling factor of 10^{-8}) when the average temperature and average velocity reached a steady state. The minimum size of the model grid is 781 m × 781 m after eight adaptive refinements, and the minimum total time step is ~7000–13000 yr, the melting (migration) time step is 1000 yr, which satisfies reasonable resolution requirements of ULVZs.

We briefly summarize the idealizations and simplifications we adopted for the models in this study: (a) We utilized the bottom boundary conditions to represent our conceptual framework rather than explicitly introducing the cold subducted plates and the underlying dense liquid outer core. (b) To evaluate different boundary conditions, we employed simplified material properties associated with the melt migration model. We then compared the findings of our model with those of an unsimplified property (Dannberg) model under the same boundary conditions. (c) We utilized a 2D symmetric (along x=0) model; thus, our discussion of boundary conditions effects does not cover asymmetric outcomes; although this limits the discussion, it allows a simpler dynamics for easy understanding.

3. Results

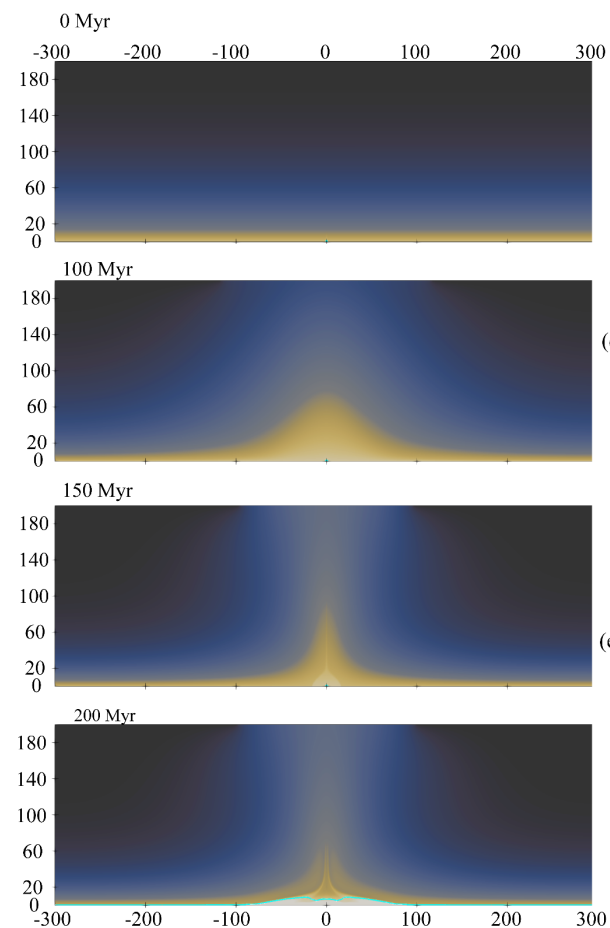### 3.1. Impact of melt-solid mass-density difference on melt formation

First, we compared the "Dannberg" model with our reference model while simplifying the material model (Figures 2 and 3) in order to control variables. We then compared the results of the reference model with those of the subsequent experimental model with modified bottom boundary conditions.

We refer to the model with the simplified material parameters, tangential flow, and constant temperature bottom boundary as "ref" in Figure 2. The binary melt system with the same bottom boundary is referred to as "Dannberg" (Dannberg et al., 2021).
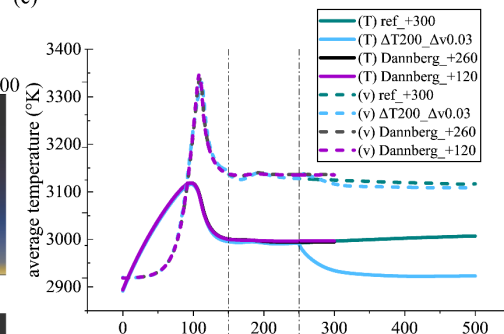
Experimental model "ΔT200_Δv0.03" depicts the model with a modified bottom boundary, whose lateral extent and velocity distribution (with direction-and-sense) are

identical to those obtained in the reference model (Figure 3), in which the CMB-mantle mass moves away from the center within the mantle plume and towards the center outside; in model "ΔT200_Δv0.03," these velocities are Dirichlet-prescribed. The peak temperature difference between the cold source location and the normal ambient mantle was -200 K ($T_{\text{bottom, peak}}$-$T_{\text{bottom, ambient}}$), and the peak horizontal velocity was 3 cm/yr (i.e., 30 km/Myr) (v_{peak}). The specific distributions along the bottom boundary are shown in Figure 7d and 7b.
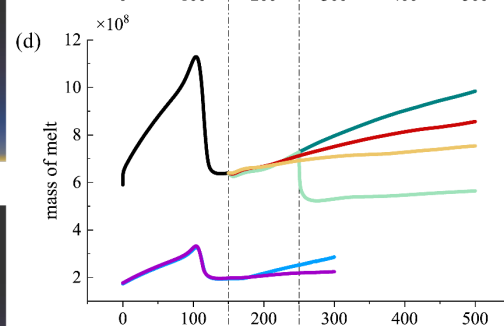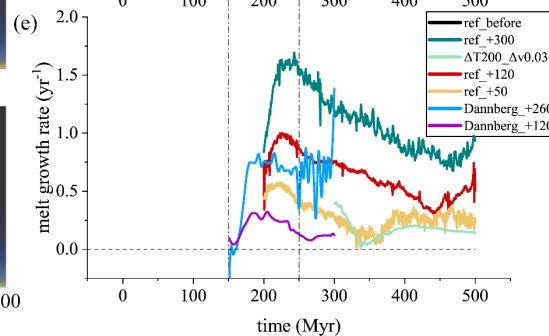
(a)

0 Myr

100 Myr

150 Myr

200 Myr

shear viscosity (Pa·s)

1e+18   5e+18 1e+19   5e+19 1e+20   5e+20 1e+21   5e+21 1e+22   1e+23

(c)

- (T) ref_+300
- (T) ΔT200_Δv0.03
- (T) Dannberg_+260
- (T) Dannberg_+120
- (v) ref_+300
- (v) ΔT200_Δv0.03
- (v) Dannberg_+260
- (v) Dannberg_+120

average temperature (°K)

root mean square velocity (m/yr)

(d)

×10⁸

mass of melt

(e)

- ref_before
- ref_+300
- ΔT200_Δv0.03
- ref_+120
- ref_+50
- Dannberg_+260
- Dannberg_+120

melt growth rate (yr⁻¹)

time (Myr)

(b)

500 Myr   Δρ = +300 kg/m³

500 Myr   Δρ = +120 kg/m³

500 Myr   Δρ = +50 kg/m³

density (kg/m³)

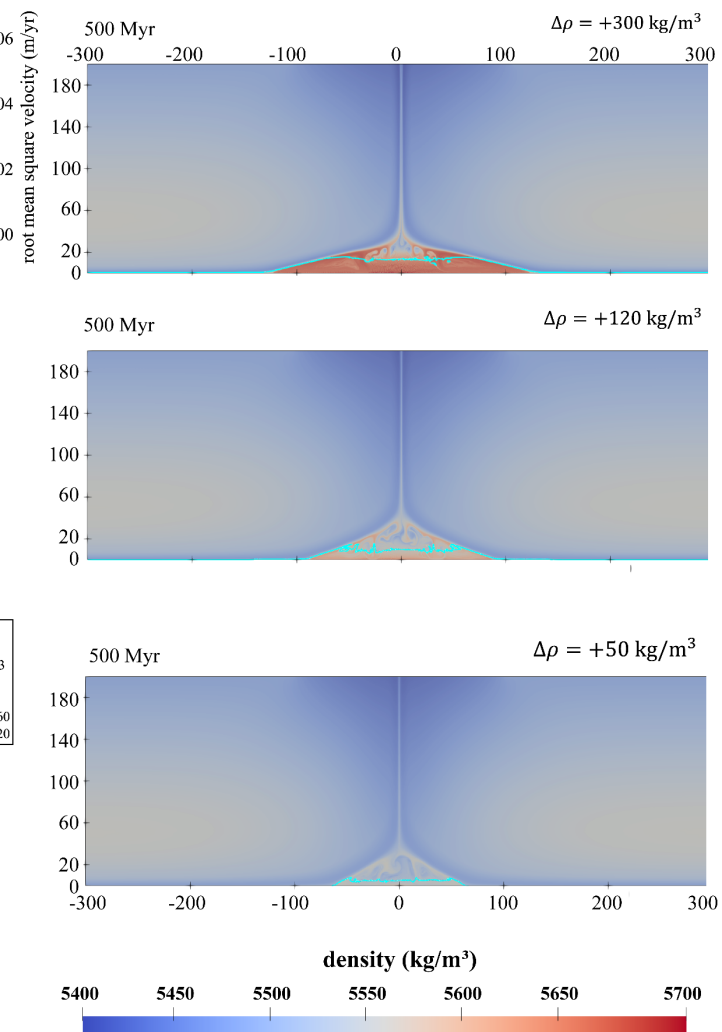5400   5450   5500   5550   5600   5650   5700

Figure 4. Comparison of the results for different melt-solid density difference models. (a) Reference model evolution shown by shear viscosity distribution, blue contour is the same as in Figure 3. **(b) Reference model comparison of the melt-solid density differences $\Delta\rho$** (ρ_{melt} - ρ_{solid} = +50, +120, and +300 kg·m^{-3}) at the simulated end time (500 Myr), shown by density distribution ($\bar{\rho}$= (1-ϕ) ρ_{solid} + $\phi\rho_{\text{melt}}$, where ϕ is the melt fraction), blue contour as in Figure 3. Center column: **Evolution of (c) the average velocity (right axis), average temperature (left axis) over the entire study area, (d) total melt mass, and (e) melt growth rate.** The number after the model name represents the melt-solid density difference (kg·m^{-3}). "ref" represents the reference model (Figure 3), "ref_before" is the stage before melt migration (150 Myr), "Dannberg" is the model from (Dannberg et al., 2021), "ΔT200_Δv0.03" is the experimental model with the density difference of 300 kg·m^{-3} and the non-uniform constant bottom boundary, with $\Delta T = T_{\text{bottom,peak}}$-$T_{\text{bottom, ambient}}$ = -200 K and $\Delta v = v_{\text{bottom, peak}}$ = 0.03 m/yr. The detailed distribution is shown in Figure 7d and 7b. We choose the melt growth rate of "Dannberg_+120" as the criteria to evaluate whether the melt has reached stability in Figure 6.

Figure 4a shows the evolution of the shear viscosity field for model "ref+300". The low-viscosity melt was initially generated at the bottom of the plume and then spread to the sides after melt migration occurred, as shown by the yellow backdrop and blue contour. Figure 4b displays the melt density distribution (density $\bar{\rho} = (1-\phi) \rho_{solid} + \phi\rho_{melt}$, where ϕ is the melt fraction) for different density differences ($\Delta\rho = \rho_{melt} - \rho_{solid}$) of the "ref" model at the simulated end time (500 Myr). As the melt-solid density difference increased, the red high-density melt structure became increasingly wider on the sides. Similar to the findings of previous studies, a smaller positive density difference makes it easier for it to be entrained in the rising mantle flow, and the negative-density melt allows it to ascend through the mantle without accumulating at its base (Garnero & McNamara, 2008).

Except for the total amount of melt (Figure 4d), the results of our reference model versus the "Dannberg" model reveal no significant difference (Figure 4c). Figure 4c depicts the evolution of the average velocity and temperature over the entire study area. The mantle flow in the model no longer varied considerably following the development of the mantle plume (150 Myr, black dashed line on the left); however, the average temperature decreased after the bottom cold source was applied (250 Myr, black dashed line on the right). Figure 4d shows the results of total melt mass growth over time. Our reference and "Dannberg" models both show that the smaller the density difference, the easier the melt stabilizes.

Although the total melt mass obtained from the "ref" model ended as 4–5 times greater than that obtained from the "Dannberg" model, it does not affect our study of their melt variation tendencies (Figure 4d and 4e). In addition, using the stable "Dannberg (+120)" shown in purple as a baseline, we see that the melt of the "ref (+50)" with lower positive density difference, as well as experimental model "$\Delta T200\_\Delta v0.03$" with a cold source and bottom tangential flow, eventually reaches stability. Then, we take the melt growth rate of "Dannberg (+120)" as the criteria for evaluating whether the melt has reached stability in Section 4.1.

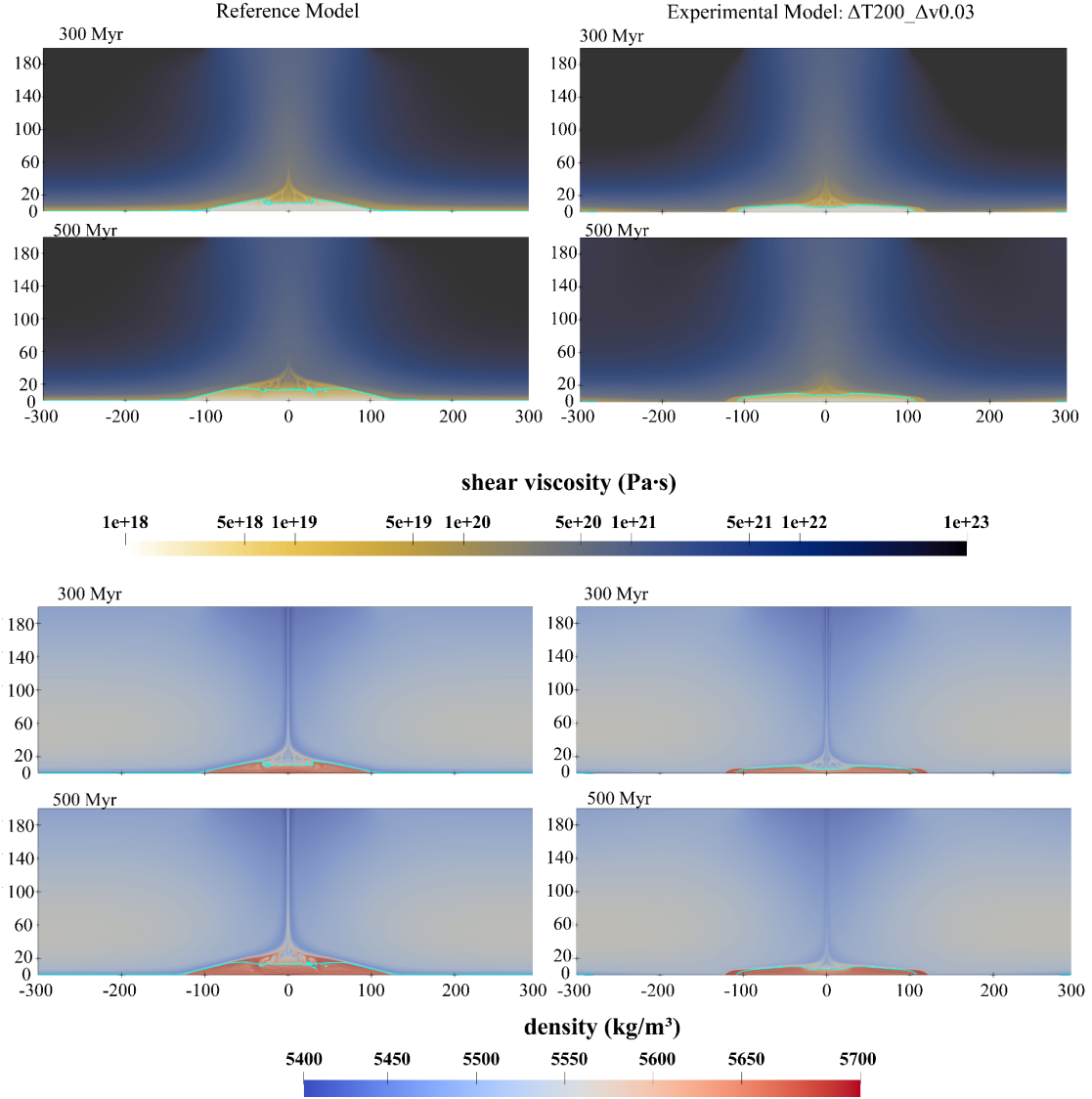## 3.2. Impact of the bottom boundary setup on melt morphology

Figure 5. Comparison of the reference and experimental model at 300 and 500 Myr, shown by shear viscosity (top) and mass density (bottom). "ref_+300" model (left column) and "ΔT200_Δv0.03" (right column) are the same as Figure 4, and the blue line as in Figure 3. In the right-column (prescribed Dirichlet-type velocity bottom boundary condition), the high-density, low-viscosity melt region has a flatter top and steeper edges than the left-column reference model.

Figure 5 depicts the model density and shear viscosity distributions without (left) and with (right) changes in the bottom boundary conditions at two instants, revealing that after the application of the cold source and bottom tangential flow, the model produces a melt with sharp edges and flat tops similar to those observed in seismic data (Rost et al., 2005, 2006), whereas the aspect ratio of the melt layer increases in the latter.

Previous interpretations of the steep edges of the LLSVP and ULVZs have emphasized the pushing effect of the subduction plate with mantle flow (Davies et al., 2015; John William Hernlund & Bonati, 2019). Our findings indicate that the thermal effect of the subduction plate as a cold source between it and the ULVZs is sufficient to generate a melt layer with sharp edges in which the internal tangential flow, enhanced by the CMB topography and the uppermost outer core, also plays a significant role.

4. Discussion

4.1. Stable conditions for high-density melts

We assumed that the conditions of this distribution near the edge of the LLSVPs allowed for lengthy durations of existence (> 100 Myr), as mentioned in Section 2.3. Hence, in this section, the boundary values remained constant during the parametric analysis. To explore the influence of varying bottom temperature and velocity parameters on the melt growth rate, we fixed the melt-solid density difference at +300 kg·m^{-3}, as shown in Figure 6.
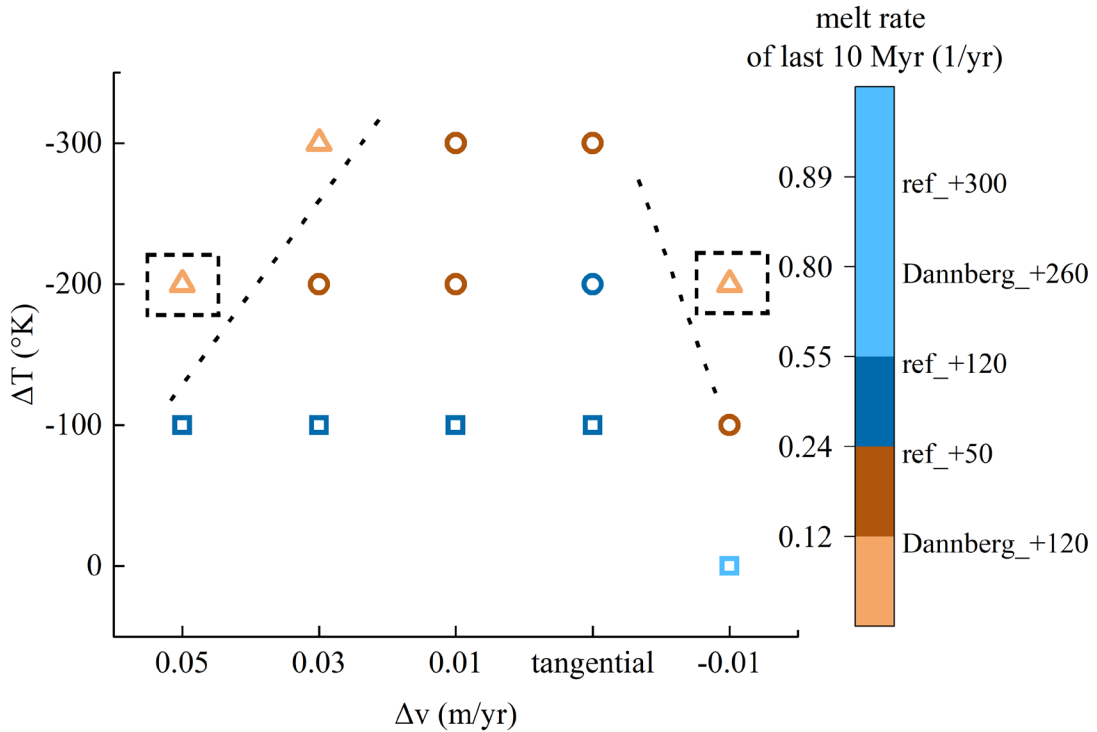

Figure 6. Phase diagram of melt growth-rate for the model bottom boundary setups. The model mass-density differences (ρ_{melt} - ρ_{solid}) are fixed at +300 kg·m^{-3}. ΔT is the peak value of the applied bottom temperature difference, between the 'cold-source' and the ambient

($\Delta T = T_{bottom,peak} - T_{bottom, ambient}$), separated by horizontal distance of approximately 100 km and defines the rows in the plot. Δv represents the peak value of applied bottom-boundary velocity (Dirichlet-type) ($\Delta v = v_{bottom, peak}$) and defines the columns in the plot. Note that for comparison, we replaced "$\Delta v = 0$" with a **tangential** (Neumann-type) velocity boundary as in the reference model (Figure 3). Each element represents one single simulation. Colors indicate the average melt growth rate within 10 Myr before the simulated end time (500 Myr). The symbols in the right-side legend indicate the classification criteria derived from the reference model results (Figure 4e). The category of melt-stability discrimination: Orange triangles indicate that model melt reached a stable state (top left and right corners), blue rectangles indicate unstable states and brown circles are transition state models. The simulations enclosed by dashed-line squares are used in Figure 7.

In Figure 6, the vertical coordinates represent the lateral temperature difference peaks between a mantle neighboring cold source and normal ambient mantle ($\Delta T = T_{bottom,cold\ peak} - T_{bottom, ambient}$) of 0, -100, -200, and -300 K. The horizontal axis indicates the velocity setup (Dirichlet-type) with positive labels for flow in the same direction of the tangential flow model (Neumann-type) (Figure 3), with maximum values ($\Delta v = v_{bottom, peak}$) of 0.01, 0.03, and 0.05 m/yr, and a single negative value of -0.01 m/yr (meaning flow in the opposite direction to that of reference). The melt growth rate for the last 10 Myr of the simulation is represented by the colors in Figure 6 and is depicted in Figure 4e. The categorization criteria for determining whether the melt reaches stability are presented in the legend. Based on previous studies (Dannberg et al., 2021; John W. Hernlund & Jellinek, 2010) and the melt results in Figure 4d and 4e, we used the melt rates of the "Dannberg+120" and "ref+50" models as the cut-off.

This indicates that the melt stabilization zone lies in the upper left positive-flow-velocity region and the upper right negative-flow-velocity region of the phase diagram. Thus, the greater the temperature differences and velocity when the velocity direction is the same as the "ref" model (positive), the easier the melt stabilizes. Additionally, a maximum velocity of 0.01 m/yr can stabilize the melt when the velocity is reversed (negative). The cold source reduced the melt fraction, and the CMB-mantle tangential flow increased the cooling effectiveness. Furthermore, stronger flow facilitates the migration of the melt towards localized "cooling zone." In the absence of a cold source,

strong bottom tangential flow cannot stabilize the melt. To stabilize a melt that has a higher density (ρ_{melt} - ρ_{solid} > 50–120 kg·m^{-3}), a cold source is necessary, with the corresponding lateral temperature difference between ~4000 K at the plume central regions to <~3900 K at the plume-cooling intermediate mantle region, separated by horizontal distances of ~100 km (approximately as shown in Figure 7).

When the density difference between the solid and melt is approximately ~+10% ((ρ_{melt}-ρ_{solid})/ρ_{solid}), the stable presence of melt still requires a cold source with a temperature difference absolute value >100 K (Table 3). However, the melt growth rate decreased for the same boundary setup when the density difference approached approximately 10%, indicating that the lower limit of the boundary conditions relaxed for additional increases in the density difference. We speculate that this may be because the Rayleigh number (Ra = $\rho g \alpha \Delta T h^3/(\eta \kappa)$) increases further through the density, which denotes enhanced local convection within the ULVZs and morphology stability of the melt.

Table 3. Model melt growth rate [a] comparison regarding the melt-solid density difference (ρ_{melt} - ρ_{solid} = +300, +500 kg·m^{-3}) under different bottom boundary conditions (Figure 6).

Density difference +300 kg·m^{-3}			
Bottom boundary condition	0.05 m/yr	0.03 m/yr	0.01 m/yr
-300 K		**0.107**	0.125
-200 K	**0.109**	0.147	0.208
-100 K	0.291	0.331	0.425
Density difference +500 kg·m^{-3}			
Bottom boundary condition	0.05 m/yr	0.03 m/yr	0.01 m/yr
-300 K	**0.057**	**0.064**	**0.080**
-200 K	**0.109**	**0.111**	0.158
-100 K	0.362		0.426

[a] The stable (bolded) upper limit of the growth rate is the same as Figure 6 ("Dannberg_+120" model: ~0.12 yr^{-1}).

4.2. Morphological characteristics of the stabilized melt

Because both positive and negative velocities can mechanically stabilize the melt, as described in Section 4.1, we selected the two models "ΔT200_Δv0.05" and "ΔT200_Δv-0.01" ringed by dashed circles in Figure 6 to study the differences in the generated melt morphology.

(a)

ΔT200_Δv-0.01

500 Myr

500 Myr

ΔT200_Δv0.05

melt fraction

0   0.05   0.1   0.15   0.2   0.25

(b)

velocity x (m/yr)

Δv0.05
Δv-0.01
ΔT200

(c)

dynamic topography (m)

(d)

melt fraction

temperature (°K)

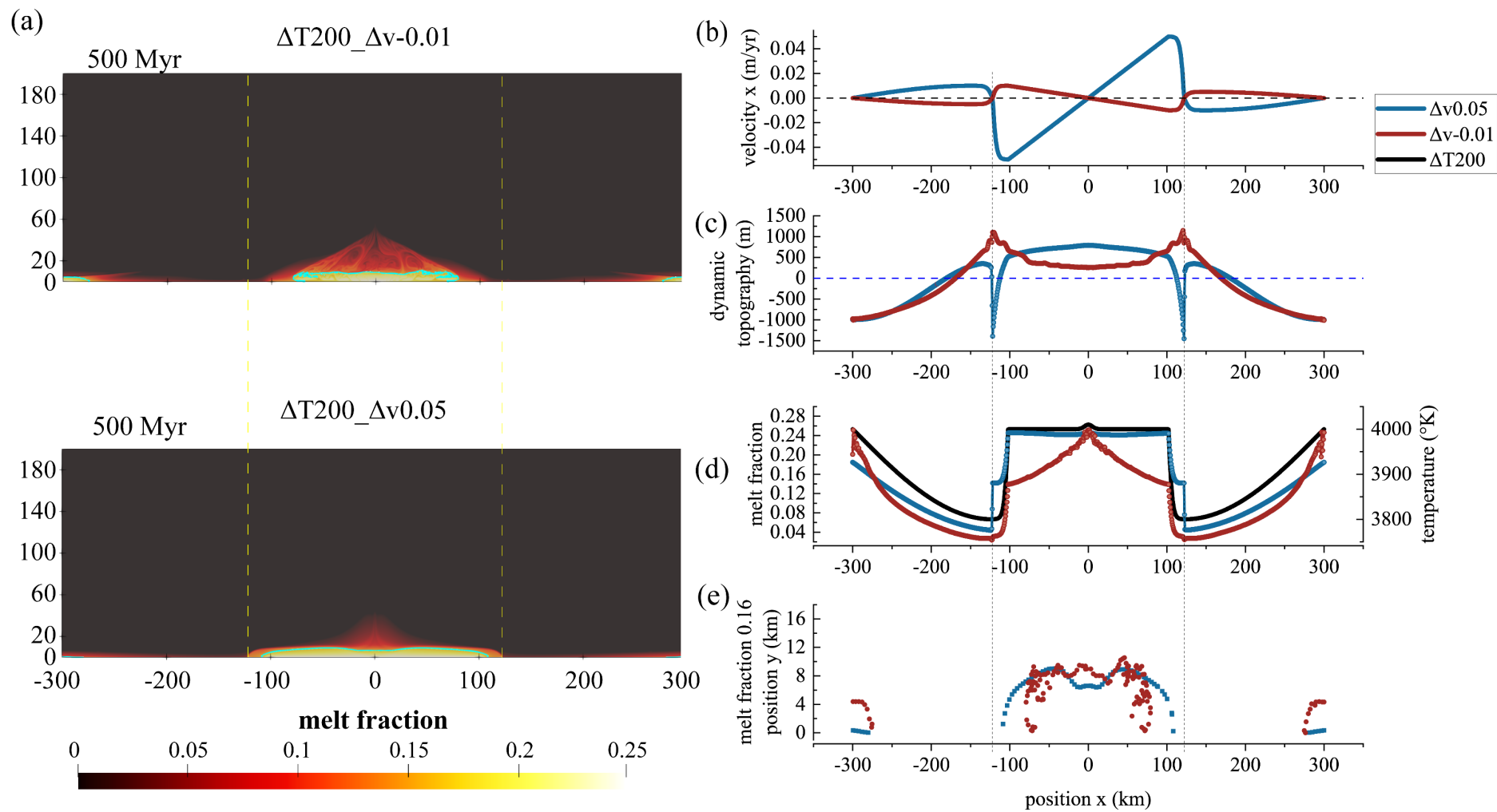(e)

melt fraction 0.16 position y (km)

position x (km)

Figure 7. Example model results illustrating the effect of the applied bottom velocity direction, distinguished and indicated by dashed-line squares in Figure 6. Symbol "-" indicates that the direction is opposite to the reference model (Figure 3). **(a) Model melt fraction at the simulated end time (500 Myr)**, blue line is the same as in Figure 3. **(b) Applied bottom horizontal velocity distribution, (c) model bottom dynamic topography** ($h=\sigma_{rr}/[(\mathbf{g}\cdot\mathbf{n})\cdot(\rho-\rho_{core})]$, where σ_{rr} is the normal stress), **(d) model bottom melt fraction (left) and applied bottom temperature distribution (right)** ($\Delta T = -200$ °K, Figure 6), **and (e) spatial distribution of the fixed melt fraction (0.16)**. Dark blue model: The bottom horizontal velocity peak value (Δv, Figure 6) is 0.05 m/yr, and the velocity direction within the plume is away from the center (same as the reference model, Figure 3). Brown model: The velocity is 0.01m/yr, and the direction within the plume is towards to the center (opposite of the reference model). The melt morphology of the dark blue model is more consistent with the seismic constraints.

Figure 7a shows the melt fraction distributions for both models at the end of the simulation (500 Myr). Figure 7b–d depict the results for the tangential velocity at the bottom boundary of the model, CMB dynamic topography, melt fraction, and applied temperature. The horizontal and vertical axes in Figure 7e are spatial coordinates indicating the contour spatial distribution for a melt fraction of 0.16. The dashed lines represent the location of ULVZ/plume edges.

The edge of the melt layer, where the mantle flow meets because of an abrupt change in the velocity direction (Figure 7b), is the area of lower melt degree depicted in Figure 7a. However, compared with the smoother border of the negative model, the edge of positive model is steeper. The dynamic topography in Figure 7c similarly reflects this sharp edge; however, the negative model lacks this feature, whereas the positive model exhibits a local topographic jump with an amplitude of 1–2 km comparable to the total value. The melt fraction depicted in Figure 7d decreased towards the edges because of the applied cold-source temperatures and thermal diffusion. In particular, the melt fraction in the model decreased by ~10% within a few kilometers, corresponding to the melt density variation and gradually increasing dynamic topography (Figure 7c). Finally, the melt fraction distribution (Figure 7a, e) shows that the lateral extent and aspect ratio of the melt layer of the positive model were substantially larger, and the top region of its low-melt-fraction zone was flatter than that of the negative model.

More specifically, studies of long-wavelength topography have demonstrated the contribution of the LLSVP to lower mantle flow (Heyn et al., 2020; Lassak et al., 2010), and our results show that when the ULVZs are engaged, the topography undulations are shorter horizontally (~20 km) and more pronounced vertically (~1–2 km). Previous study has estimated that a 1% melt corresponds to a shear wave velocity reduction of approximately 2.5% (Dannberg et al., 2021). Therefore, owing to the cold source presence, there may be a "cooling zone" for the plume (with strong lateral heat flux), with a ~10% lateral variation in shear wave velocity at the plume edge with a slightly lower melting degree. In summary, the melt layer morphologies produced by models with bottom velocities in the same direction as the internal reverse circulation were

more consistent with seismic observations (Rost et al., 2005). The local variation in the lateral melt fraction and the higher local topographic jump (gradient) at the plume edge were the main features of this model.

We then conducted a parameter analysis, as illustrated in Figure 8, to compare the precise impacts of various model bottom conditions on the ULVZ morphology (aspect ratio).
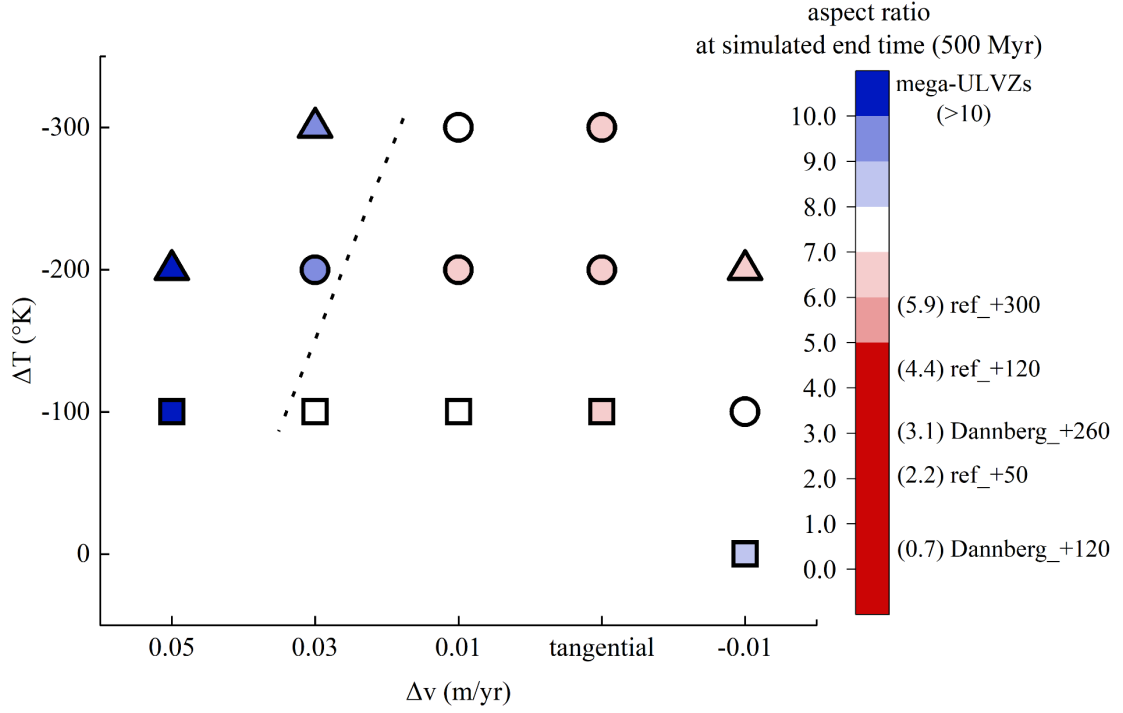

Figure 8. Phase diagram of melt aspect ratio for the model bottom boundary setups. The model density difference and plot symbols are the same as in Figure 6. *Aspect ratio* = (width / height) melt. *Melt width*: horizontal distance (left-side) from the model center to location where melt fraction contour (0.1) vertical-thickness reaches 5 km. *Melt height*: the height of the fixed melt fraction (0.1) in the model center. Colors indicate the melt aspect ratio at the simulated end time (500 Myr). The right side legend symbols show the aspect ratio of the reference models (Figure 3) and the mega-ULVZs (Figure 1 and Table 1). The aspect ratios of the reference models are ≤6 (legend right), whereas all models with changed bottom boundary setup are >6 (background). The aspect ratios of top left area models are more consistent with the seismic observational constraints.

As in Figure 6, the horizontal and vertical axes in Figure 8 represent the boundary conditions, and the symbols indicate whether the melt is stable. The color in the figure represents the melt aspect ratio at the end of the simulation. We take the height of the central melt fraction 0.1 as the ULVZ height, and the distance from the model center to

the (left) location where the thickness of melt fraction 0.1 reaches 5 km as the ULVZ width. Therefore, the aspect ratio is defined as the melt width/melt height. Because the "Dannberg" model produces less melt, the melt fraction is set to 0.16, and the thickness limit is set at 1 km.

The reference model results (Figure 5) are shown on the right side of the legend. The melt aspect ratios of these bottom tangential flow models are <6, and the smaller the density difference, the lower the aspect ratio and the more "towering" the melt region, which is consistent with the results in Section 3.1. The aspect ratios of the models with the modified bottom conditions were all >6, and the larger the velocity magnitude, the flatter the melt region in the positive model. This suggests that a stronger bottom tangential flow can suppress a wider range of mantle flows above the CMB, allowing the upper melt layer to have a greater lateral scope.

As mentioned in Table 1, the aspect ratios of the mega-ULVZs shown at the top of the legend are substantially larger (>10). Based on the thickness (5–40 km) and lateral extent ($x \times 10^2$–10^3 km) of the ULVZs observed, the majority had an aspect ratio of >5. Therefore, if the simulation results are comparable to the seismic observations, the high-density melt must be coupled to the bottom local CMB-mantle flow, where the flow velocity is in the same direction as the internal reverse circulation. Moreover, the magnitude of flow velocity is related to the morphology of the melt.

4.2.1 Other factors affecting melt morphological characteristics

In the previous sections, the peak value position of the applied cold source, approximately 100 km from the mantle plume center, was fixed. First, we considered the effect of the location of the cold source on the chemical stability of the melt. We then adjusted the distance from the peak value position of the applied cold source to the plume center, specifically, 50 km closer to and farther from the center. As a result, compared to the "$\Delta T200\_\Delta v0.03$" model in Figure 5, the melt growth rates of the different models have the following range: no cold source > cold source 50 km farther from the center > cold source -100 K at the same position > cold source 50 km closer to the center > cold source -200 K ("$\Delta T200\_\Delta v0.03$") (Figure S4). It can be observed

that the cold source, both too close and too far from the plume center, increases the melt growth rate (unstable trend).

In terms of the dynamic topography of the CMB, the distant cold source (+50 km) mitigated the impacts of local topographical undulation near the edge of the plume. In contrast, a nearby cold source (-50 km) extends the lateral extent of the undulation, with minimal effect on the maximum topographical leap amplitude. In terms of melt morphology, the sharp-edged and flat-topped melt layer features vanish as the cold source advances further from the mantle plume (+50 km). Conversely, as the cold source approaches (-50 km), the smaller low-melting degree melt zones emerge at the plume edge (Figure S5). However, the high-melting morphology at the bottom of the plume, is less affected by the nearby cold source.

As a result, the "cooling zone" for the plume must continue to be involved in the melt stabilization process. However, if the cold source is too close, it changes the low-melting morphology at the base of the plume, increasing the two edges and severely lowering the center (Figure S5).

In addition, we investigated the impact of positive and negative Clapeyron-slopes on the "$\Delta T200\_\Delta v0.03$" model results. We changed the initial melt state parameters in Table 2 such that the melt layers in the positive and negative slope models had approximately the same thickness (~15 km) at the beginning of the modeling process (Table S1). The findings demonstrate that a negative Clapeyron slope flattens the central low-melting zone but has no impact on the total melt mass and melt growth rate at the simulated end time (Clapeyron-slope+: 0.152 yr^{-1}, Clapeyron-slope-: 0.147 yr^{-1}) (Figure S6), nor does it have an impact on the dynamic topography of the CMB and its high-melting morphology (Figure S7).

4.3. CMB dynamical environment implied by the ULVZs morphology

Furthermore, based on the dynamic conditions described in the previous sections, we evaluated the characteristics of the bottom flow field from the ULVZs morphology. We previously applied a constant bottom velocity constraint, which is partly consistent with the morphological properties of the melt system once it reaches thermochemical-

mechanical stability. In this section, the bottom tangential velocity is dynamically determined using the topographic horizontal gradient.

First, the bottom dynamic topography was calculated using the normal stress, specifically, its perturbations with respect to the reference adiabatic regime hydrostatic pressure:

$$\sigma_{rr} = \hat{g}^T \left(2\eta \left(\varepsilon(\boldsymbol{u}) - \frac{1}{3}(\nabla \cdot \boldsymbol{u})\boldsymbol{I} \right) \right) \hat{g} - p_d \tag{9}$$

where $p_d = p - p_{\text{adiabatic}}$, and $\hat{g} = \frac{\boldsymbol{g}}{\|\boldsymbol{g}\|}$.

The dynamic topographic is

$$h = \frac{\sigma_{rr}}{(\rho - \rho_{\text{core}})(\boldsymbol{g} \cdot \boldsymbol{n})} \tag{10}$$

where $\rho_{\text{core}} = 9900$ kg/m³ (Dziewonski & Anderson, 1981).

We referred to the equation used to calculate the normal infiltration rate in the "Lim" model (Lim et al., 2021), in which the topographic gradient was used to calculate the tangential velocity as follows:

$$v = c \cdot \frac{\Delta \rho (\boldsymbol{g} \cdot \boldsymbol{n})}{12\eta} \cdot \nabla_x^2 h^4 \tag{11}$$

where c represents the dimensionless scaling factor.

We used $\Delta T = 0$ K and $\Delta v < 0.02$ m/yr at the initial stage (250 Myr, consistent with the setup in Figure 4) because a greater "Δv" results in numerical instability here. Because of the absence of a cold source, the melted layer did not exhibit chemical stability. The results of the opposing horizontal velocity (x) direction models are displayed in Figure 9, where "reference-consistent" indicates horizontal velocity x away from the center in the interior of the plume (consistent with the reference model in Figure 3), and "reference-opposite" indicates horizontal velocity x towards the center within the plume.

Specifically, at the simulated end time (500 Myr), "reference-consistent" was slightly smaller (0.92) than the "ref_+300" model, and "reference-opposite" was roughly equal to (1.00) the "ref_+300" model. The generated melt layer also exhibited a lower aspect ratio. Here, we focused on the evolution and duration of some melt features.
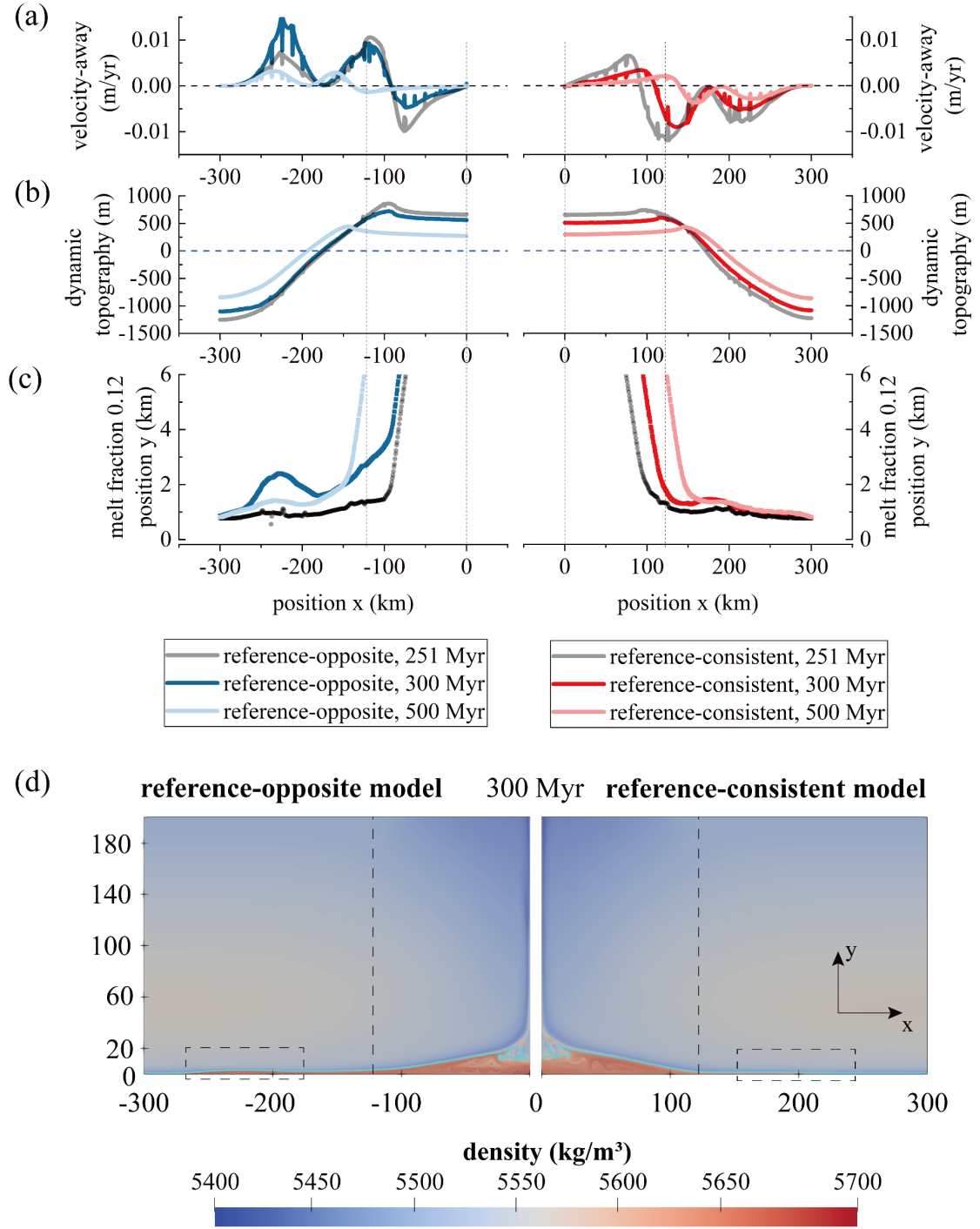
Figure 9. Model evolution results of topography-coupled bottom velocity boundary at 251 (gray, the beginning of the setup), 300 (dark color), and 500 Myr (light color). *Reference-consistent*: red, horizontal velocity (x) direction is applied away from the center within the plume, same with reference model (Figure 3). *Reference-opposite*: blue, horizontal velocity (x) direction is applied towards the center within the plume. **(a) Bottom horizontal velocity (x) distribution** (>0: away from the plume center, <0: towards the plume center)**, (b) model bottom dynamic topography,** and **(c) the spatial distribution of the fixed melt fraction (0.12). (d) Model mass-density at 300 Myr** (density $\bar{\rho} = (1-\phi)\,\rho_{\text{solid}} + \phi\rho_{\text{melt}}$, where ϕ is the melt fraction), and the blue line is the same as in Figure 3. To reduce the disturbances of numerical

errors, for panels (a, b, c) and for each model we center x = 0 km and take averages (arithmetic mean) of the values of the variables from both sides about x=0; then, we plot them on the right side of the "reference-consistent" model and on the left side of the "reference-opposite" model respectively. (d) Black dashed-line boxes indicate a possible "melt bulge" area outside the plume in the "reference-opposite" model (left), virtually absent in the "reference-consistent" model.

Figure 9a represents the bottom tangential velocity (>0: away from the plume center, <0: towards the plume center) evolution, and the velocity at the side boundaries is still artificially suppressed. In contrast to the previous model distribution, there are locations outside the plume where the velocity drops to zero under the combined influence of the topography and topographic gradient.

To reduce the influence of numerical errors, we center on vertical axis x = 0 km, average the values on both sides (Figure 9a–c); later, for the figure plots, we show the right side of "reference-consistent" and the left side of "reference-opposite" (Figure 9d). The results reveal that, owing to the larger topographic gradient, the velocity near the plume edge (dashed vertical line) can be maintained for at least 50 Myr (250–300 Myr), whereas the velocity values were reduced in other areas. As for the later stage (300–500 Myr), the results demonstrated that the bottom velocity values rapidly increased at locations of high strain rate, causing the melt layer to spread towards the outside of the plume (Figure 9d), leading to a decrease in local velocity within the plume (Figure 9a), the local topography becoming smooth (Figure 9b), and the spatial distribution of the melt increasing (Figure 9c). We believe that (a) a lack of the cold source causes outward expansion of the melt layer with plume edge movement and (b) the bottom flow velocity with simple constant scaling factor c in equation (11), both of which lead to the decay of the velocity magnitude within the plume at this stage.

Notably, the area away from the plume in the "reference-opposite" model (-250 to -200 km in Figure 9c) forms the smaller "melt bulge." Even if we intentionally suppressed the mantle velocity outside the plume close to the side boundaries, a "melt bulge" still occurred. Finally, as the simulation progresses (300–500 Myr), the dynamic topography value decreases due to the continuous growth of the melt to both sides (Figure 9b), resulting in a decrease in the bottom velocity magnitude (Figure 9a) and

the height of the "melt bulge."

The "reference-consistent" modeling results partially indicate the dynamical environment around the hot mantle plume area, validating our "Dirichlet" boundary setup described in the previous sections. However, to understand the "reference-opposite" model findings, we must start with the conceptual model. The dynamic environments of the cold-downwelling zone and ascending mantle plume are opposite, and under gravitational action, the opposite mantle flow produces opposite CMB dynamic topography. Because the topographic gradients under these regions can be comparably strong and long lasting, the CMB-mantle flow can be significantly influenced by the uppermost core flow, and the flow field direction may be opposite to that of the regional mantle flow (Figure 10). Then a CMB-mantle "opposite" flow and corresponding boundary layer may exist over several kilometers of thickness, resulting in larger local viscous stress.

Therefore, the outer-plume region of the "reference-opposite" model may indicate the CMB-mantle flow near the cold zone, and the "melt-bulge" (found in the simulation) may correspond to the ULVZs in the cold zone. By suppressing the above-adjacent mantle flow near the cold-downwelling zone, the CMB-mantle flow (in opposition) may also contribute to the creation of ULVZs. However, because the outer core cannot be properly recreated in our modeling, the "reference-opposite" model itself cannot provide robust evidence of the process, meaning a self-consistent mechanism for the generation of locally high stress that can contribute to the ULVZs development in cold zone.

Furthermore, how did the low-velocity material originate to form in the "cold zone?" For the constant-in-time velocity model, which is applied with constant extended cold source ($\Delta T = -100$ K) and tangential velocity setup (as in the "reference-opposite" model, $\Delta v = 0.01$ m/yr), the result shows that the similar appearance of the "melt bulge" outside of the plume (Figure S8). The reduced melt fraction decreased the resulting melt-solid density difference, which reduced the CMB-mantle tangential flow velocity allowed by a gravitationally more stable structure. It ultimately lowers the length-scale and magnitude of "low wave-velocity anomaly." Our further validation of the low-

velocity material sources of partial melting in the cold zone is limited by the simplified material properties of the model, such as linear solidus-liquidus. However, previous research indicates that the liquid core material can penetrate the CMB in the downwelling flow region, although the resulting "mushy layer" thickness is ~1 km (Kanda & Stevenson, 2006; Lim et al., 2021). If the local CMB-mantle flow is involved, the initial formation melt may thicken into a "low-velocity zone," as shown in the model in this section. In general, owing to limitations of the temperature and topographic gradient, the range of ULVZs developed here is narrower than that in the plume region, which may explain why certain ULVZs and "low-velocity layer" appear in the "cold zone," as shown in Figure 1 (Fan et al., 2022; Yu & Garnero, 2018) (Figure 10). Compared with ULVZs formed near the superplume edge, ULVZs in the cold zone have a smaller scale and less lateral variation in seismic-wave velocity, which can be verified by geophysical observations.

Finally, we have discussed the mechanisms of melt stabilization at the plume edge and in the cold zone. However, the localized denser melts, detected by seismic observations at the bottom center of the plume, may not be "controlled" by the CMB-mantle flow due to small CMB-topographic gradients and may continue to accumulate and grow until the lateral extent extends to a sufficiently cooled zone, where P-T conditions limit the amount of melt and preclude further melt growth-advancement, by melt-solid equilibration. From our reference modeling results (Figures 5 and 8), during this process, larger melt heights and smoother-edge ULVZ morphologies were likely the main characteristics.
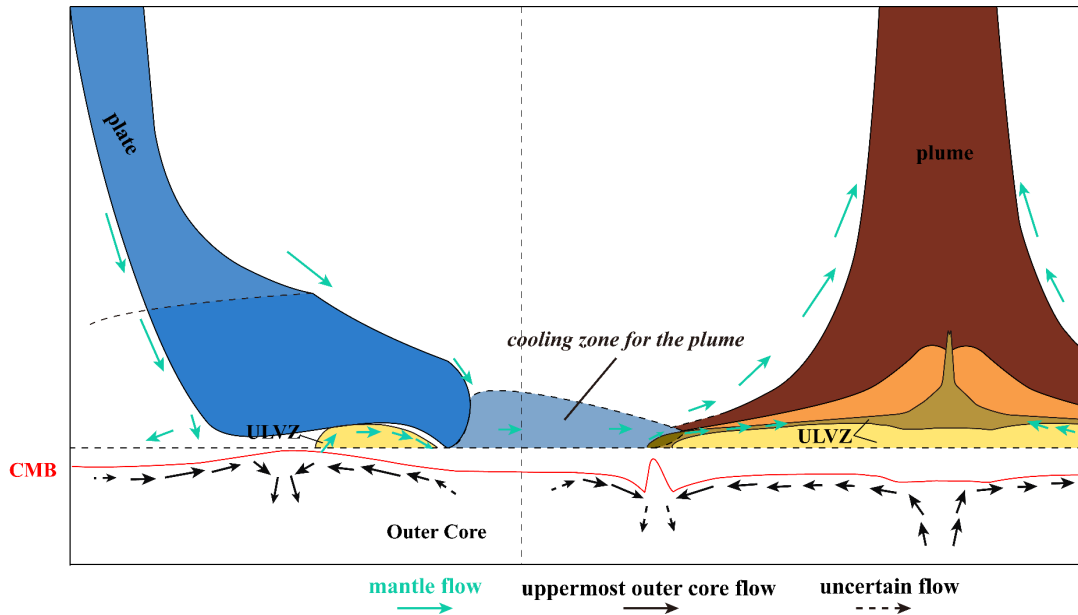
Figure 10. Schematic representation of the model conclusions. The subdomain on the right side from the vertical dashed line indicates the study area in our model, and the left side indicates the presumed environment involved in the cold downwelling. Note, the near-bottom dashed horizontal line is a simple referential CMB for ease of plotting, where the **red solid line** depicts a dynamic CMB responding to this plume-and-plate environment. **Dark brown**: the mantle plume, **orange tones**: the melting layer with increasing melt degrees (darker), **blue**: the cold subduction plate (solid line), and the high-velocity layer of the resulting cold source (dashed line). The melt fraction is lower at the area where the "cooling zone" meets the edge of the plume. **Yellow**: ULVZs, occur at the base of the plume and in areas with large CMB topographic gradients of the "cold zone". **Cyan arrows**: lowermost mantle flow direction, **black solid arrows**: flow direction near the CMB and at the uppermost outer core, **black dashed arrows**: core flow with assumed direction.

4.4. Model limitations

Our model is simplified using a 2D geometrical description and by having a constant distribution coefficient of Fe and Mg between the solid and liquid phases, as well as a linear solidus-liquidus equation curve. It was chosen to isolate the effect of the bottom boundary conditions on melt generation and speed up the simulations to compare different model setups. This simplification may lead to inaccuracies related to the following.

(1) Compared to a 3D model, the 2D model we introduced neglects heat transfers in the 3rd direction and likely underestimates the plume heat losses. Furthermore, 2D Dirichlet velocity BC would require mostly exaggerated drag forces on the CMB to

generate the tangential velocity consistent with the magnitude of the lowermost mantle flow.

(2) Compared to the "Dannberg" model, the material properties we used exaggerate the total melt mass; to avoid this, we focused on the melt growth rate and the aspect ratio of melt morphology.

(3) We did not explore the effect of viscosity. However, previous studies indicated that the height of ULVZ is not sensitive to its viscosity (Beuchert & Schmeling, 2013), and whether viscosity affects the melt morphology in the edge area requires further study.

(4) We did not directly or explicitly model the mechanical interaction between the subducting plates and ambient mantle, nor the intercoupling between the subducting plates and the low-viscosity outer core because of numerical stability limitations and to conveniently isolate the basic controlling factors. Instead, we applied different bottom boundary conditions at a certain time, which led to the resulting evolution of the ULVZs differing slightly from the corresponding geological evolution of the real Earth.

To focus on the specific problem, most of the discussion in this study is based on our numerical models, which are symmetric about x = 0. In future studies, based on the asymmetric model results (Figure S3), different scales, extents, and locations of cold sources and/or CMB-mantle flows should be considered and purposely applied to the left or right side to examine asymmetric scenarios that are closer to the real Earth.

5. Conclusions

(1) The stable existence and residence of high-density ((ρ_{melt}-ρ_{solid})/ρ_{solid} >+1–2%, reaching ~+10%) melt requires, in the scenario we studied, the participation of a cold source, and corresponding lateral temperature differences between ~4000 K at the plume central regions to <~3900 K at the plume-cooling intermediate mantle region, separated by horizontal distances of about 100 (±<50) km. The plume-cooling intermediate region is the region where heat flows from the hot plume base (at the center of our model) towards a neighboring cold source (not explicitly modeled in our settings), such as a subducted plate that advects cold isotherms from the surface (Figure 10); a configuration that may last for several hundred million years with respect to mantle

viscosities and thermal diffusivities.

(2) To obtain ULVZ results with a high aspect ratio that matches seismic observations, high-density melt requires the participation of a CMB-mantle flow that is oriented with internal reverse circulation of/inside the plume broad basal region. Furthermore, the fluid dynamics of this problem dictate that the magnitude of the velocity is related to the melt liquid-body morphology. The ULVZ morphology with a flat top and sharp edge necessitates local CMB-mantle flow horizontal speeds of approximately >3 times the characteristic convective speed of the lower mantle (~1 cm/yr), which can be attained by episodic mantle forces and/or outer core interactions (favored by CMB topography that enhances resistance and coupling of the flow stresses, and potentially/eventually magnetic forces).

(3) The local CMB-mantle flow facilitated by the CMB topography interacting with the outer core may be important (and perhaps crucial) in developing mega-ULVZs, particularly when the latter is spread or located near the edges of a superplume, phenomena that may be transient in mantle evolution of the Earth. Our point of view is related to the fact that seismic-observations studies discovered ULVZs in certain "cold zones" with higher seismic-wave speeds. However, their lateral extents were smaller owing to the limitations of temperature and topographic gradient amplitude.

Acknowledgments

Data Availability Statement

References

Aubert, J., Amit, H., & Hulot, G. (2007). Detecting thermal boundary control in surface flows from numerical dynamos. *Physics of the Earth and Planetary Interiors*, *160*(2), 143–156. https://doi.org/10.1016/j.pepi.2006.11.003

Bangerth, W., Dannberg, J., Fraters, M., Gassmoeller, R., Glerum, A., Heister, T., et al. (2022, July 25). ASPECT v2.4.0. Zenodo. https://doi.org/10.5281/zenodo.6903424

Beuchert, M. J., & Schmeling, H. (2013). A melting model for the lowermost mantle using Clapeyron slopes derived from experimental data: Consequences for the thickness of ultralow velocity zones (ULVZs). *Geochemistry, Geophysics, Geosystems*, *14*(1), 197–208. https://doi.org/10.1029/2012GC004356

Boukaré, C.-E., Ricard, Y., & Fiquet, G. (2015). Thermodynamics of the MgO-FeO-SiO2 system up to 140 GPa: Application to the crystallization of Earth's magma ocean. *Journal of Geophysical Research: Solid Earth*, *120*(9), 6085–6101. https://doi.org/10.1002/2015JB011929

Brandon, A. D., & Walker, R. J. (2005). The debate over core–mantle interaction. *Earth and Planetary Science Letters*, *232*(3), 211–225. https://doi.org/10.1016/j.epsl.2005.01.034

Buffett, B. (2014). Geomagnetic fluctuations reveal stable stratification at the top of the Earth's core. *Nature*, *507*(7493), 484–487. https://doi.org/10.1038/nature13122

Buffett, B. (2016). Another energy source for the geodynamo. *Nature*, *529*(7586), 288–289. https://doi.org/10.1038/529288a

Cottaar, S., Martin, C., Li, Z., & Parai, R. (2022). The root to the Galápagos mantle plume on the core-mantle boundary. *Seismica*, *1*(1). https://doi.org/10.26443/seismica.v1i1.197

Dannberg, J., & Heister, T. (2016). Compressible magma/mantle dynamics: 3-D, adaptive simulations in ASPECT. *Geophysical Journal International*, *207*(3), 1343–1366. https://doi.org/10.1093/gji/ggw329

Dannberg, J., Myhill, R., Gassmöller, R., & Cottaar, S. (2021). The morphology, evolution and seismic visibility of partial melt at the core–mantle boundary: implications for ULVZs. *Geophysical Journal International*, *227*(2), 1028–1059. https://doi.org/10.1093/gji/ggab242

Davies, D. R., Goes, S., & Lau, H. C. P. (2015). Thermally Dominated Deep Mantle LLSVPs: A

Review. In A. Khan & F. Deschamps (Eds.), *The Earth's Heterogeneous Mantle: A Geophysical, Geodynamical, and Geochemical Perspective* (pp. 441–477). Cham: Springer International Publishing. https://doi.org/10.1007/978-3-319-15627-9_14

Dehant, V., Campuzano, S. A., De Santis, A., & van Westrenen, W. (2022). Structure, Materials and Processes in the Earth's Core and Mantle. *Surveys in Geophysics*, *43*(1), 263–302. https://doi.org/10.1007/s10712-021-09684-y

Deschamps, F., & Li, Y. (2019). Core-Mantle Boundary Dynamic Topography: Influence of Postperovskite Viscosity. *Journal of Geophysical Research: Solid Earth*, *124*(8), 9247–9264. https://doi.org/10.1029/2019JB017859

Dobson, D. P., & Brodholt, J. P. (2005). Subducted banded iron formations as a source of ultralow-velocity zones at the core–mantle boundary. *Nature*, *434*(7031), 371–374. https://doi.org/10.1038/nature03430

Dziewonski, A. M., & Anderson, D. L. (1981). Preliminary reference Earth model. *Physics of the Earth and Planetary Interiors*, *25*(4), 297–356. https://doi.org/10.1016/0031-9201(81)90046-7

Fan, A., & Sun, X. (2021). Origin of ULVZs near the African LLSVP: Implications from their distribution and characteristics. *Earthquake Science*, *34*(4), 299–309. https://doi.org/10.29382/eqs-2021-0042

Fan, A., Sun, X., Zhang, Z., Zhang, P., & Zong, J. (2022). From Subduction to LLSVP: The Core-Mantle Boundary Heterogeneities Across North Atlantic. *Geochemistry, Geophysics, Geosystems*, *23*(1), e2021GC009879. https://doi.org/10.1029/2021GC009879

Fearn, D. R., & Loper, D. E. (1981). Compositional convection and stratification of Earth's core. *Nature*, *289*(5796), 393–394. https://doi.org/10.1038/289393a0

Flament, N., Williams, S., Müller, R. D., Gurnis, M., & Bower, D. J. (2017). Origin and evolution of the deep thermochemical structure beneath Eurasia. *Nature Communications*, *8*(1), 14164. https://doi.org/10.1038/ncomms14164

Garnero, E. J., & McNamara, A. K. (2008). Structure and Dynamics of Earth's Lower Mantle. *Science*, *320*(5876), 626–628. https://doi.org/10.1126/science.1148028

Garnero, E. J., Revenaugh, J., Williams, Q., Lay, T., & Kellogg, L. H. (1998). Ultralow Velocity Zone at the Core-Mantle Boundary. In *The Core-Mantle Boundary Region* (pp. 319–334).

American Geophysical Union (AGU). https://doi.org/10.1029/GD028p0319

Garnero, E. J., McNamara, A. K., & Shim, S.-H. (2016). Continent-sized anomalous zones with low seismic velocity at the base of Earth's mantle. *Nature Geoscience*, *9*(7), 481–489. https://doi.org/10.1038/ngeo2733

Glane, S., & Buffett, B. (2018). Enhanced Core-Mantle Coupling Due to Stratification at the Top of the Core. *Frontiers in Earth Science*, *6*. Retrieved from https://www.frontiersin.org/article/10.3389/feart.2018.00171

Hansen, U., & Yuen, D. A. (1988). Numerical simulations of thermal-chemical instabilities at the core–mantle boundary. *Nature*, *334*(6179), 237–240. https://doi.org/10.1038/334237a0

Helffrich, G., & Kaneshima, S. (2010). Outer-core compositional stratification from observed core wave speed profiles. *Nature*, *468*(7325), 807–810. https://doi.org/10.1038/nature09636

Hernlund, J. W., & McNamara, A. K. (2015). 7.11 - The Core–Mantle Boundary Region. In G. Schubert (Ed.), *Treatise on Geophysics (Second Edition)* (pp. 461–519). Oxford: Elsevier. https://doi.org/10.1016/B978-0-444-53802-4.00136-6

Hernlund, John W., & Jellinek, A. M. (2010). Dynamics and structure of a stirred partially molten ultralow-velocity zone. *Earth and Planetary Science Letters*, *296*(1), 1–8. https://doi.org/10.1016/j.epsl.2010.04.027

Hernlund, John W., & Tackley, P. J. (2007). Some dynamical consequences of partial melting in Earth's deep mantle. *Physics of the Earth and Planetary Interiors*, *162*(1), 149–163. https://doi.org/10.1016/j.pepi.2007.04.005

Hernlund, John William, & Bonati, I. (2019). Modeling Ultralow Velocity Zones as a Thin Chemically Distinct Dense Layer at the Core-Mantle Boundary. *Journal of Geophysical Research: Solid Earth*, *124*(8), 7902–7917. https://doi.org/10.1029/2018JB017218

Heyn, B. H., Conrad, C. P., & Trønnes, R. G. (2020). Core-mantle boundary topography and its relation to the viscosity structure of the lowermost mantle. *Earth and Planetary Science Letters*, *543*, 116358. https://doi.org/10.1016/j.epsl.2020.116358

Jenkins, J., Mousavi, S., Li, Z., & Cottaar, S. (2021). A high-resolution map of Hawaiian ULVZ morphology from ScS phases. *Earth and Planetary Science Letters*, *563*, 116885. https://doi.org/10.1016/j.epsl.2021.116885

Jensen, K. J., Thorne, M. S., & Rost, S. (2013). SPdKS analysis of ultralow-velocity zones beneath

the western Pacific. *Geophysical Research Letters*, *40*(17), 4574–4578. https://doi.org/10.1002/grl.50877

Jones, C. A. (2015). 8.05 - Thermal and Compositional Convection in the Outer Core. In G. Schubert (Ed.), *Treatise on Geophysics (Second Edition)* (pp. 115–159). Oxford: Elsevier. https://doi.org/10.1016/B978-0-444-53802-4.00141-X

Kanda, R. V. S., & Stevenson, D. J. (2006). Suction mechanism for iron entrainment into the lower mantle. *Geophysical Research Letters*, *33*(2). https://doi.org/10.1029/2005GL025009

Kellogg, L. H., & King, S. D. (1993). Effect of mantle plumes on the growth of D" by reaction between the core and mantle. *Geophysical Research Letters*, *20*(5), 379–382. https://doi.org/10.1029/93GL00045

Koelemeijer, P., Ritsema, J., Deuss, A., & van Heijst, H.-J. (2016). SP12RTS: a degree-12 model of shear- and compressional-wave velocity for Earth's mantle. *Geophysical Journal International*, *204*(2), 1024–1039. https://doi.org/10.1093/gji/ggv481

Labrosse, S., Hernlund, J. W., & Coltice, N. (2007). A crystallizing dense magma ocean at the base of the Earth's mantle. *Nature*, *450*(7171), 866–869. https://doi.org/10.1038/nature06355

Lassak, T. M., McNamara, A. K., Garnero, E. J., & Zhong, S. (2010). Core–mantle boundary topography as a possible constraint on lower mantle chemistry and dynamics. *Earth and Planetary Science Letters*, *289*(1), 232–241. https://doi.org/10.1016/j.epsl.2009.11.012

Lay, T., Hernlund, J., & Buffett, B. A. (2008). Core–mantle boundary heat flow. *Nature Geoscience*, *1*(1), 25–32. https://doi.org/10.1038/ngeo.2007.44

Li, M., McNamara, A. K., Garnero, E. J., & Yu, S. (2017). Compositionally-distinct ultra-low velocity zones on Earth's core-mantle boundary. *Nature Communications*, *8*(1), 177. https://doi.org/10.1038/s41467-017-00219-x

Li, Z., Leng, K., Jenkins, J., & Cottaar, S. (2022). Kilometer-scale structure on the core–mantle boundary near Hawaii. *Nature Communications*, *13*(1), 2787. https://doi.org/10.1038/s41467-022-30502-5

Lim, K. W., Bonati, I., & Hernlund, J. W. (2021). A Hybrid Mechanism for Enhanced Core-Mantle Boundary Chemical Interaction. *Geophysical Research Letters*, *48*(23), e2021GL094456. https://doi.org/10.1029/2021GL094456

Luo, S.-N., Ni, S., & Helmberger, D. V. (2001). Evidence for a sharp lateral variation of velocity at

the core–mantle boundary from multipathed PKPab. *Earth and Planetary Science Letters*, *189*(3), 155–164. https://doi.org/10.1016/S0012-821X(01)00364-8

McKENZIE, D. (1984). The Generation and Compaction of Partially Molten Rock. *Journal of Petrology*, *25*(3), 713–765. https://doi.org/10.1093/petrology/25.3.713

Mckenzie, D. P., Roberts, J. M., & Weiss, N. O. (1974). Convection in the earth's mantle: towards a numerical simulation. *Journal of Fluid Mechanics*, *62*(3), 465–538. https://doi.org/10.1017/S0022112074000784

McNamara, A. K. (2019). A review of large low shear velocity provinces and ultra low velocity zones. *Tectonophysics*, *760*, 199–220. https://doi.org/10.1016/j.tecto.2018.04.015

McNamara, A. K., & Zhong, S. (2005). Thermochemical structures beneath Africa and the Pacific Ocean. *Nature*, *437*(7062), 1136–1139. https://doi.org/10.1038/nature04066

McNamara, A. K., Garnero, E. J., & Rost, S. (2010). Tracking deep mantle reservoirs with ultra-low velocity zones. *Earth and Planetary Science Letters*, *299*(1), 1–9. https://doi.org/10.1016/j.epsl.2010.07.042

Mound, J., Davies, C., Rost, S., & Aurnou, J. (2019). Regional stratification at the top of Earth's core due to core–mantle boundary heat flux variations. *Nature Geoscience*, *12*(7), 575–580. https://doi.org/10.1038/s41561-019-0381-z

Olson, P., Landeau, M., & Reynolds, E. (2017). Dynamo tests for stratification below the core-mantle boundary. *Physics of the Earth and Planetary Interiors*, *271*, 1–18. https://doi.org/10.1016/j.pepi.2017.07.003

O'Rourke, J. G., & Stevenson, D. J. (2016). Powering Earth's dynamo with magnesium precipitation from the core. *Nature*, *529*(7586), 387–389. https://doi.org/10.1038/nature16495

Otsuka, K., & Karato, S. (2012). Deep penetration of molten iron into the mantle caused by a morphological instability. *Nature*, *492*(7428), 243–246. https://doi.org/10.1038/nature11663

Pachhai, S., Li, M., Thorne, M. S., Dettmer, J., & Tkalčić, H. (2022). Internal structure of ultralow-velocity zones consistent with origin from a basal magma ocean. *Nature Geoscience*, *15*(1), 79–84. https://doi.org/10.1038/s41561-021-00871-5

Ricard, Y. (2015). 7.02 - Physics of Mantle Convection. In G. Schubert (Ed.), *Treatise on Geophysics (Second Edition)* (pp. 23–71). Oxford: Elsevier. https://doi.org/10.1016/B978-

0-444-53802-4.00127-5

Rost, S., Garnero, E. J., Williams, Q., & Manga, M. (2005). Seismological constraints on a possible plume root at the core–mantle boundary. *Nature*, *435*(7042), 666–669. https://doi.org/10.1038/nature03620

Rost, S., Garnero, E. J., & Williams, Q. (2006). Fine-scale ultralow-velocity zone structure from high-frequency seismic array data. *Journal of Geophysical Research: Solid Earth*, *111*(B9). https://doi.org/10.1029/2005JB004088

Rost, S., Garnero, E. J., & Stefan, W. (2010). Thin and intermittent ultralow-velocity zones. *Journal of Geophysical Research: Solid Earth*, *115*(B6). https://doi.org/10.1029/2009JB006981

Schlichting, H., & Gersten, K. (2017). *Boundary-Layer Theory*. Berlin, Heidelberg: Springer. https://doi.org/10.1007/978-3-662-52919-5

Solomatov, V. S., & Moresi, L.-N. (2002). Small-scale convection in the D″ layer. *Journal of Geophysical Research: Solid Earth*, *107*(B1), ETG 3-1-ETG 3-10. https://doi.org/10.1029/2000JB000063

Stein, C., Mertens, M., & Hansen, U. (2020). A numerical study of thermal and chemical structures at the core-mantle boundary. *Earth and Planetary Science Letters*, *548*, 116498. https://doi.org/10.1016/j.epsl.2020.116498

Sun, D., Helmberger, D., Lai, V. H., Gurnis, M., Jackson, J. M., & Yang, H.-Y. (2019). Slab Control on the Northeastern Edge of the Mid-Pacific LLSVP Near Hawaii. *Geophysical Research Letters*, *46*(6), 3142–3152. https://doi.org/10.1029/2018GL081130

Thorne, M. S., Garnero, E. J., Jahnke, G., Igel, H., & McNamara, A. K. (2013). Mega ultra low velocity zone and mantle flow. *Earth and Planetary Science Letters*, *364*, 59–67. https://doi.org/10.1016/j.epsl.2012.12.034

Vanacore, E. A., Rost, S., & Thorne, M. S. (2016). Ultralow-velocity zone geometries resolved by multidimensional waveform modelling. *Geophysical Journal International*, *206*(1), 659–674. https://doi.org/10.1093/gji/ggw114

van Tent, R., Deuss, A., Kaneshima, S., & Thomas, C. (2020). The signal of outermost-core stratification in body-wave and normal-mode data. *Geophysical Journal International*, *223*(2), 1338–1354. https://doi.org/10.1093/gji/ggaa368

WATSON, S., & McKENZIE, D. (1991). Melt Generation by Plumes: A Study of Hawaiian

Volcanism. *Journal of Petrology*, *32*(3), 501–537. https://doi.org/10.1093/petrology/32.3.501

Yu, S., & Garnero, E. (2017). ULVZ Distribution Database from 54 studies [Data set]. Zenodo. https://doi.org/10.5281/zenodo.1064217

Yu, S., & Garnero, E. J. (2018). Ultralow Velocity Zone Locations: A Global Assessment. *Geochemistry, Geophysics, Geosystems*, *19*(2), 396–414. https://doi.org/10.1002/2017GC007281

Yuan, K., & Romanowicz, B. (2017). Seismic evidence for partial melting at the root of major hot spot plumes. *Science*, *357*(6349), 393–397. https://doi.org/10.1126/science.aan0760

Zhao, C., Garnero, E. J., Li, M., McNamara, A., & Yu, S. (2017). Intermittent and lateral varying ULVZ structure at the northeastern margin of the Pacific LLSVP. *Journal of Geophysical Research: Solid Earth*, *122*(2), 1198–1220. https://doi.org/10.1002/2016JB013449

Contribution of locally tangential CMB-mantle flow and cold-source subducting plates to ULVZ formation and morphology

Jie Xin[1], Huai Zhang[1*], Yaolin Shi[1], Felipe Orellana-Rovirosa[2], Zhen Zhang[3], Yimin Jin[4]

[1]Key Laboratory of Computational Geodynamics, College of Earth and Planetary Sciences, University of Chinese Academy of Sciences, Beijing 100049, China

[2]Department of Ocean Science and Engineering, Southern University of Science and Technology, Shenzhen 518055, China

[3]State Key Laboratory of Earthquake Dynamics, Institute of Geology, China Earthquake Administration, Beijing 100029, China

[4]Institute of Geophysics, China Earthquake Administration, Beijing 100081, China

Key Points:

- The stable presence of high-density partial melts as a cause of ultra-low velocity zones requires involvement of cold subducting plates.

- The morphology of stable ULVZs is related to the direction and magnitude of the local core-mantle boundary (CMB)-mantle flow.

- Flow driven by CMB topography interacting with the outer core may help form mega-ULVZs and ULVZs in the seismic-wave cold zone.

Abstract

Ultra-low velocity zones (ULVZs) above the core-mantle boundary (CMB) are significant structures that connect the lowermost mantle and outer core. As "thin patches" of dramatically low seismic-wave velocity, they are occasionally found near the base of mantle plumes and in-or-near high seismic-wave speed regions above the CMB. The causes of their morphological distribution and geodynamics remain unclear, and simulation results of high-density melts diverge from seismic observations. We introduced a two-dimensional time-dependent Stokes two-phase flow (with melt migration) numerical model to investigate the formation and morphological

characteristics of ULVZs caused by CMB-mantle tangential flows and a neighboring cold source (subducted plate). We discovered that (a) the participation of cold sources with temperature differences between ~4000 K at the plume central regions to <~3900 K at the plume-cooling mantle region, separated by horizontal distances of approximately 100 ($\pm$<50) km are necessary for the stable existence of dense melts with mass-density difference >+1–2% (even +10%) with respect to the surrounding mantle; additionally, (b) an enhanced tangential flow coincident with the internal reverse circulation within the broad plume base (with speeds >3 times the lowermost-mantle characteristic flow speed) are necessary for higher aspect-ratio-morphology lenses compatible with seismic observations. The CMB-mantle tangential flow and/or outer-core interacting with CMB-topography may help generate mega-ULVZs, particularly if they appear along the edges of large low-shear-wave-velocity provinces (LLSVPs) and in/near high seismic-speed "cold" zones. Thus, we infer that a strong link exists between ULVZ morphology and the dynamic environment of the lowermost mantle and uppermost outer core.

Plain Language Summary

The ultra-low velocity zones (ULVZs) above the core-mantle boundary (CMB) are thin patch structures of rapidly decreasing seismic-wave velocity located at the base of the mantle plume and in the seismic-wave high-speed "cold" zone. However, the cause of their formation and morphology remains unclear. We introduced a numerical model to investigate the criteria for the stable existence and formation of a high-density melt that is consistent with the observations. By modifying the model bottom boundary conditions, we introduced the effects of the CMB-mantle flow and subducting plates as cold source. Based on our findings, the stable existence of high-density melting necessitates the involvement of a cold source with a lateral temperature difference between ~4000 K in the central region of the plume and <~3900 K in the plume-cooling intermediate mantle region. ULVZs with flat top and sharp edges require a higher CMB-mantle tangential flow than in the lowermost mantle. Thus, the flow associated with the CMB topography gradient may be involved in forming ULVZs, particularly when they are spread at the superplume margins and in the seismic-wave "cold" zone. The ULVZs morphology is more closely related to the dynamic environment of the lowermost mantle and uppermost outer core.

1. Introduction

The core-mantle boundary (CMB) is the interface between the metallic-liquid outer core and the solid oxide mantle, which is an important region for heat and mass exchange on Earth. The structural and dynamical characteristics of the CMB are affected by strong physical differences such as density (mantle: ~5500 kg·m^{-3}, core: ~9900 kg·m^{-3}) and particularly viscosity (mantle: >10^{12} Pa·s, outer-core: <10^{-1} Pa·s) (J. W. Hernlund & McNamara, 2015). In ultra-low velocity zones (ULVZs), which are 5–40 km-thick zones above the CMB, the seismic wave velocity is significantly decreased locally (~10% for P-waves and ~30% for S-waves) (Garnero et al., 1998). The ULVZs are an important structure connecting the lowermost mantle to the core, similar to the key intermediary crust between the mantle and surface (J. W. Hernlund & McNamara, 2015). From the seismic waves that pass through the core (e.g., SPdKS, PKKP, and PKP), as well as reflection (ScS, ScP, and PcP), diffraction (Pdiff and Sdiff), and scattering at the CMB (Dehant et al., 2022; Yu & Garnero, 2018), it is believed that ULVZs with "thin patches" are not globally distributed. Smaller ULVZs have a lateral extent of less than 100 km, larger mega-ULVZs can extend approximately 1000 km, and most have a large aspect ratio (Table 1). Many ULVZs are located in the center and/or at the margins of large low-shear-wave-velocity provinces (LLSVPs), but a good fraction are still found in/close-to the high seismic-speed "cold zone" (M. Li et al., 2017; Yu & Garnero, 2018) (Figure 1). Less than 20% of the CMB has been explored for ULVZs, owing to the observational resolution limitations (Z. Li et al., 2022; Rost et al., 2010). The locations of certain ULVZ images are thought to be associated with convergent regions at the mantle plume base (Dannberg et al., 2021), where ULVZs may be associated with the topography of the CMB at certain wavelengths through gravitational balance (Heyn et al., 2020; Stein et al., 2020). The size and morphology of ULVZs determined from seismic observations, together with well-constrained high-density contrast, can provide insights into the dynamics and properties of the lower mantle (Rost et al., 2005), genesis of LLSVPs (Garnero et al., 2016), and nature of global mantle convection (McNamara, 2019), even providing constraints on outer-core dynamics and the geodynamo (Buffett, 2016; Deschamps & Li, 2019).
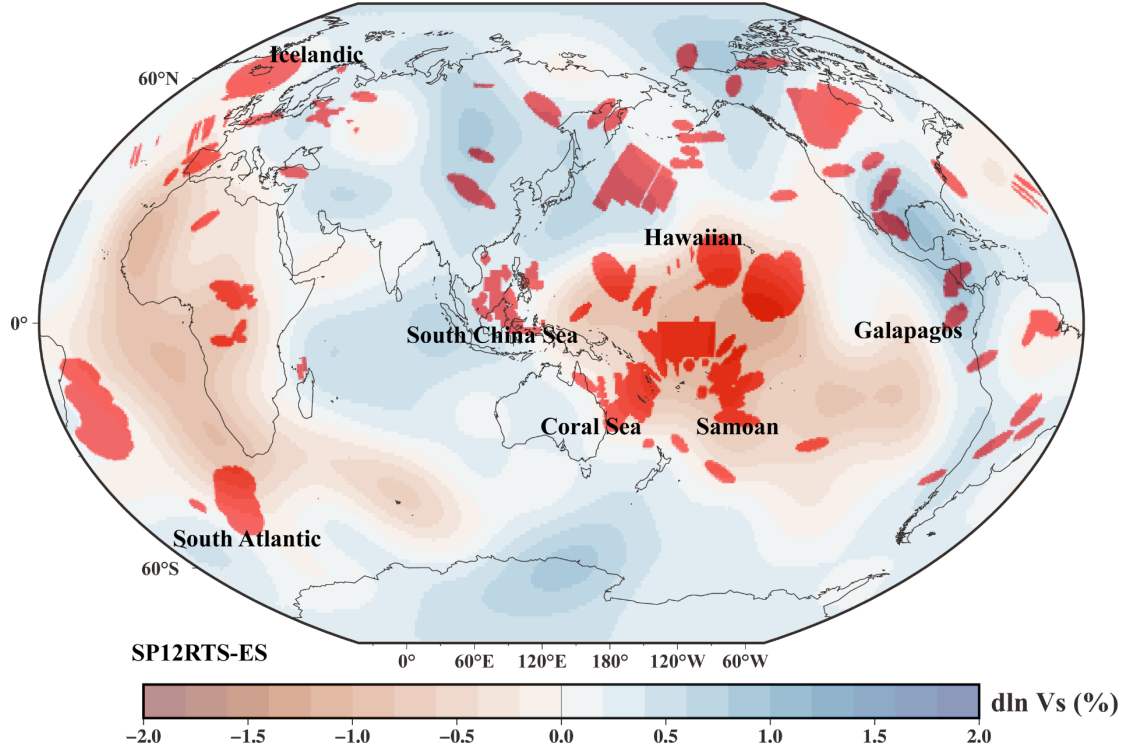
Figure 1. Global distribution of ULVZs. Red areas represent the detected ULVZ locations at/above the CMB; data from the seismic observations are summarized from (Yu & Garnero, 2017). The background color represents the shear wave velocity anomalies at 2800 km depth from the tomography model SP12RTS (Koelemeijer et al., 2016). Most area-fractions of ULVZs are located in and around low (to null) seismic-speed anomaly regions, but 30–40% of ULVZs are found in/close-to blueish, high seismic-speed "cold" regions.

Table 1. Parameters of ULVZs with good morphological constraints.

Case	Height (km)	Average lateral range/2 (km)	Aspect ratio (lateral range/2/height)	Reference
Hawaiian	30	500	16.7	(Jenkins et al., 2021)
Galapagos	20	300	15.0	(Cottaar et al., 2022)
Icelandic	15	400	26.7	(Yuan & Romanowicz, 2017)
Samoan	15	260	17.3	(Thorne et al., 2013)
Coral Sea	20	350	17.5	(Jensen et al., 2013)

South China sea	10	180	18.0	(Jensen et al., 2013)
South Atlantic	10	90	9.0	(Vanacore et al., 2016)

However, the cause of ULVZs remains controversial. It is believed that ULVZs arise from partial melting and/or chemical component anomalies, the latter possibly from early basal magma ocean crystallization residuals (Labrosse et al., 2007; Pachhai et al., 2022), core-mantle material reactions (Brandon & Walker, 2005; Kanda & Stevenson, 2006; Otsuka & Karato, 2012), and materials from subduction (Dobson & Brodholt, 2005). In most numerical simulations of the lowermost mantle, thermochemical piles have the same rheology as the background mantle (McNamara, 2019), and the ULVZs are a layer of dense chemical components (Beuchert & Schmeling, 2013; Pachhai et al., 2022). Based on seismic observations of the high-aspect-ratio low-velocity zone characteristics (Table 1) and constraints on the melt morphology and CMB topography obtained from numerical simulations (Deschamps & Li, 2019; John W. Hernlund & Tackley, 2007), researchers have found that the melt mass density that fits the observational constraints must be larger than that of the surrounding mantle phase. However, an excessively high melt density can lead to melt accumulation at the CMB. According to the equilibrium process of the melt layer under the stirring effect of mantle flow, a maximum difference of +50 kg·m^{-3} (approximately +1%) in melt-solid density difference is tolerated (John W. Hernlund & Jellinek, 2010). Based on the two-phase flow model (Dannberg & Heister, 2016) and FeO-MgO-SiO$_2$ pseudo-binary material systems (Boukaré et al., 2015), Dannberg et al. (2021) thoroughly examined the role of partial melting in the origin of ULVZs. They discovered that the tolerated melt density difference can reach approximately +120 kg·m^{-3} (~+2%) (Dannberg et al., 2021), but non-localized and high aspect-ratio melting layers were observed. Considering the seismic observations close to +10% density difference (McNamara et al., 2010; Rost et al., 2005), one question of interest is whether it is possible to enlarge the melt-solid density difference to a higher range (ρ_{melt}-ρ_{solid} $\gtrsim$+(50–120) kg·m^{-3}, i.e., (ρ_{melt}-ρ_{solid})/ρ_{solid} >+1–2%) while the ULVZs melt layer remains

stable. What is the mechanism of the melt layer formation with a high aspect ratio observed in the current seismic observations? Why do certain ULVZs appear in/around high seismic-speed "cold" zone, and does the morphology and distribution of ULVZs indicate the involvement of additional dynamical mechanisms regarding lowermost mantle flow?

Most previous studies modeled the CMB as a temperature-isothermal velocity-free-slip boundary. Conversely, the CMB region may have resulted from a combination of hot and light mantle plume, dense thermochemical piles, and cold and dense subducting/subducted plates (Hansen & Yuen, 1988; Lay et al., 2008). Based on the waveform fitting results of the ScS phase, the formation of ULVZs may also be related to the thermal effects caused by the subduction of slabs and nearby high-velocity zones (Fan & Sun, 2021; Zhao et al., 2017). On the one hand, the presence of a subducting plate pushes low-viscosity material to move, deform and perhaps steepen the boundary of the LLSVPs and/or ULVZs (McNamara & Zhong, 2005; Sun et al., 2019), suggesting that the subducting plates have an effect on the genesis and morphology of the ULVZs. On the other hand, the role of the core side on the ULVZs should also be considered, such as the process of the outer core material penetrating the mantle under dynamic pressure and collapsing with gravitational diffusion (Lim et al., 2021). At the top of the outer core, studies using seismic observations (Helffrich & Kaneshima, 2010), geomagnetic observations (Buffett, 2014), and geodynamo models (Olson et al., 2017; O'Rourke & Stevenson, 2016) suggest the presence of an ~100–400 km-thick temperature and/or component-stabilized stratified layer (Fearn & Loper, 1981; Mound et al., 2019; van Tent et al., 2020), which affects thermal, chemical, and momentum exchange through the CMB (J. W. Hernlund & McNamara, 2015). Therefore, we suggest altering the velocity and temperature bottom boundary conditions of the model to introduce and incorporate the impact of cold subducting plates and the CMB-mantle tangential flow. This allowed us to study the spatial relationships of the corresponding high-density melt ULVZs in relation to hot and cold sources and provide some constraints on the plausible dynamic conditions at the CMB and the uppermost outer core.

2. Model setup

2.1. governing equations

We used the finite element software ASPECT (2.4.0) to solve the compressible two-dimensional (2D) Stokes viscous two-phase flow equation (1–4) as well as the temperature field advection-diffusion equation (5) with heat source terms from shear heating, adiabatic heating, and latent heat change from melting/freezing (Bangerth et al., 2022; Dannberg & Heister, 2016; McKENZIE, 1984).

$$\frac{\partial}{\partial t}\left[\rho_f \phi\right] + \nabla \cdot \left[\rho_f \phi \boldsymbol{u}_f\right] = \Gamma \tag{1}$$

$$\frac{\partial}{\partial t}\left[\rho_s(1 - \phi)\right] + \nabla \cdot \left[\rho_s(1 - \phi)\boldsymbol{u}_s\right] = -\Gamma \tag{2}$$

$$\phi(\boldsymbol{u}_f - \boldsymbol{u}_s) = -\frac{k_\phi}{\eta_f}(\nabla p_f - \rho_f \mathbf{g}) \tag{3}$$

$$-\nabla \cdot \left[2\eta\dot{\varepsilon} + \xi(\nabla \cdot \boldsymbol{u}_s)\mathbf{1}\right] + \nabla p_f = \bar{\rho}\boldsymbol{g} \tag{4}$$

$$\bar{\rho}C_p\left(\frac{\partial T}{\partial t} + \boldsymbol{u}_s \cdot \nabla \mathrm{T}\right) - \nabla \cdot k\nabla \mathrm{T} = 2\eta(\dot{\varepsilon_s}:\dot{\varepsilon_s}) + \alpha T(\boldsymbol{u}_s \cdot \nabla p_s) + T\Delta S\Gamma \tag{5}$$

We used the compositional advection equation (6) for porosity and depletion to represent the melt migration process.

$$\frac{\partial C_i}{\partial t} + \boldsymbol{u}_s \cdot \nabla C_i = \Gamma^i \tag{6}$$

where subscript f denotes fluid/melt, subscript s denotes solid, ϕ is the porosity/melt fraction, and $\bar{X}$ denotes the averaged quantities $\bar{X} = (1\text{-}\phi) X_s + \phi X_f$. ρ is the density, $\mathbf{u}$ is the velocity, Γ denotes the melt rate given by the compositional equation reaction term, and k_Φ, η, p, $\boldsymbol{g}$, $\dot{\varepsilon}$, and ξ are the permeability coefficient, shear viscosity, pressure, gravitational acceleration, strain rate, and bulk viscosity associated with material dilatation /compaction, respectively. In equation (5), C_p, T, k, and α are the specific isobaric heat capacity, temperature, thermal conductivity, the coefficient of thermal expansion, respectively. S is the entropy owing to the release or consumption of latent heat.

2.2. material model

We simplified the material parameters of the following models to describe the

differences in the melt-solid physical properties in terms of the porosity and depletion of the compositional field, in addition to utilizing the "Dannberg" model parameters as the reference model for comparison (Dannberg et al., 2021). The detailed material parameters are as follows:

Table 2. Material properties of the numerical models.

parameter	value	unit
Melting time scale	10^3	yr
depletion [a]		
Depletion density change	-180	$kg \cdot m^{-3}$
Depletion solidus change	216	°K
Maximum Depletion viscosity change	10^4	——
viscosity		
Reference bulk viscosity ξ_{ref}	10^{23}	Pa·s
Reference melt viscosity $\eta_{f, ref}$	10	Pa·s
Reference shear viscosity η_{ref}	10^{23}	Pa·s
Exponential melt weakening factor	23	——
initial melt state		
Pressure solidus change ΔT_p	-10^{-8}	Pa^{-1}
Surface solidus $T_{sol,0}$	5100	K
Difference between liquidus and solidus T_{liquid}-T_{solid}	1900	K
permeability		
Reference permeability $k_{\Phi, ref}$	5×10^{-12}	m^2
Gravity acceleration $\boldsymbol{g}$	10.68	$m \cdot s^{-2}$
density		
Reference melt density $\rho_{f, ref}$	5800	$kg \cdot m^{-3}$
Reference solid density $\rho_{s, ref}$	5500	$kg \cdot m^{-3}$
Melt compressibility	1.6×10^{-12}	Pa^{-1}
Solid compressibility	1.6×10^{-12}	Pa^{-1}
thermal dependence		
Reference temperature T_{ref}	298	K

Reference specific heat $C_{p, ref}$	1230	$J \cdot kg^{-1} \cdot K^{-1}$
Thermal conductivity k	8.5	$W \cdot m^{-1} \cdot K^{-1}$
Thermal expansion coefficient α	1×10^{-5}	K^{-1}
Thermal viscosity exponent	10	——
Thermal bulk viscosity exponent	10	——

[a] Based on an approximate estimate from the Dannberg model setup.

When a phase change occurs,

$$\phi_{equilibrium} = \frac{T - T_{sol}}{T_{liq} - T_{sol}} \tag{7}$$

$$T_{sol} = T_{sol,0} + \Delta T_p p + \Delta T_c C_{depletion} \tag{8}$$

where $C_{depletion}$ is composition depletion, and $\Delta T_c = 200$ °K.

Here, the first parameter, the melting time scale, was set to be smaller than the advection time step to accurately resolve the melting/freezing process. The difference in the Fe-Mg distribution in the solid melt described by depletion (indicating the residue after melt migration) leads to variations in density and melt fraction. We refer to the physical parameters of the "Dannberg" model and let distribution coefficient $K_D = \frac{X_{Fe}^S X_{Mg}^l}{X_{Fe}^l X_{Mg}^S}$ remains constant (0.23) during the model simulation. We do not explore the viscosity change in this model; therefore, we keep the "exponential melt weakening factor" fixed, making its shear viscosity near the lowermost mantle 10^{19}–10^{22} Pa·s (Ricard, 2015). The three parameters of the initial melt state describe the initial and subsequent melting area. Combined with the geothermal line, we created a model in the initial stage ~15 km thick, with a maximum value of 0.16. The Clapeyron slope employed here was negative (Beuchert & Schmeling, 2013), and we investigated the impact of positive and negative slopes separately in Section 4.2. We used the same compression coefficient for both the solid and melt to conveniently regulate the variation in the melt-solid density and only altered the reference density during the subsequent study. The specific heat changes in the model with the temperature and melt fraction. Temperature, pressure, and melt fraction affect the latent heat in the heat source term.

A 2D Cartesian box model with dimensions 600 km (horizontal) × 200 km (vertical) was used to model the lowermost mantle (Figure 2). The initial temperature profile was adiabatic and a temperature perturbation (before melt migration was +50 K, after which it was +10 K) was continuously applied at the bottom center of the model (0 km) to trigger a mantle plume. The porosity and depletion represented by the compositional field were both zero in the initial stage.

As shown in Figure 2, our computational model is symmetric about x = 0 (the central vertical line). In the real Earth, different regions near the mantle plume do not have the same thermal-chemical structure (such as subducted plates), as prescribed here. The reason we continue to use the a full-symmetrical model, rather than using just half of it (any of the sides x≤0 or x≥0), is to verify and illustrate the accuracy of the results from the numerical modeling, that is, that any apparent asymmetry is beyond the scope of our discussion. In addition, in later parts of this article, we extract the symmetric part of the computation output by taking the averages (arithmetic mean) of approximately x=0 for selected variables; the symmetric part should have smaller numerical errors.
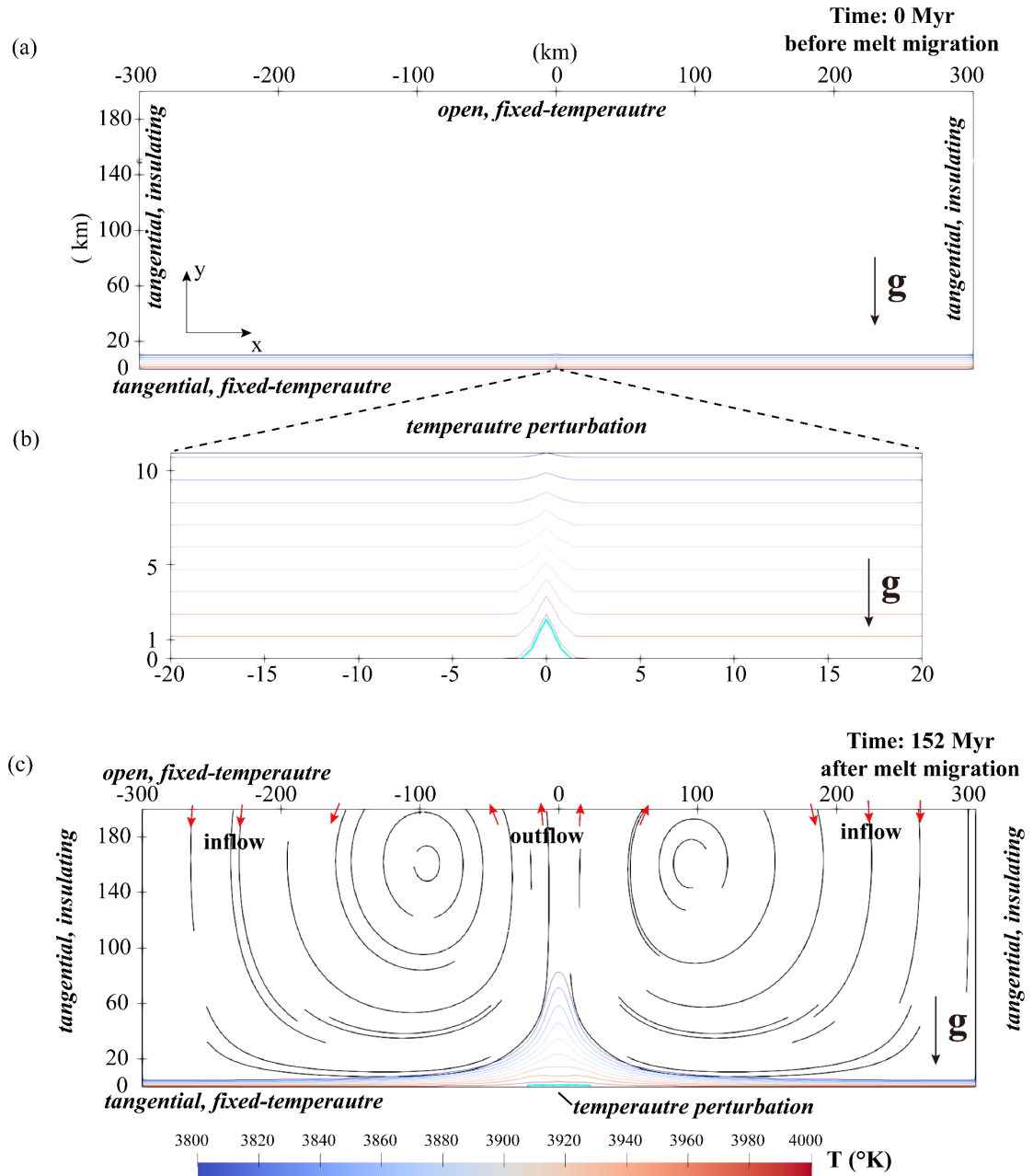
Figure 2. Reference model setup. (a) Initial condition setup before melt migration (150 Myr). The surrounding symbols represent boundary conditions, where the reference model has a fixed (in time) temperature (here 4000 K) and tangential flow at the bottom boundary. The colored contour denotes the partial temperature distribution (3800–4000 K), where a sustained temperature perturbation (before melt migration, the maximum is +50 K, after is +10 K) is applied in the bottom center to trigger the mantle plume. **(b) The initial temperature perturbation closeup.** The perturbation maximum decays exponentially as the square of the distance from the bottom boundary center. **(c) Setup after melt migration (150 Myr).** The black streamlines represent the (solid) velocity direction, and sparseness has no special meaning. Red arrows represent the flow direction at the top open boundary. The blue line represents the contour of the fixed melt fraction (0.16).

2.3. Boundary condition

The left and right boundaries of the model are adiabatic and tangential flow boundaries, that is, free-slip (zero shear stress) and no-flow-through (zero normal velocity). The upper boundary was a fixed temperature and open boundary. The bottom boundary represents the fixed (in time) CMB with a pressure of 136 GPa and temperature of 4000 K (Dziewonski & Anderson, 1981), except for a sustained temperature perturbation at the center triggering the mantle plume. The bottom velocity boundary of the reference model is also a tangential flow boundary (Figure 2). Throughout this article, we refer to the velocity of the solid phase of the mantle when we describe the velocity in the model or in the real Earth mantle. Exceptions regarding the melt are explicitly stated. We nevertheless state 'solid velocity' in a few crucial cases.
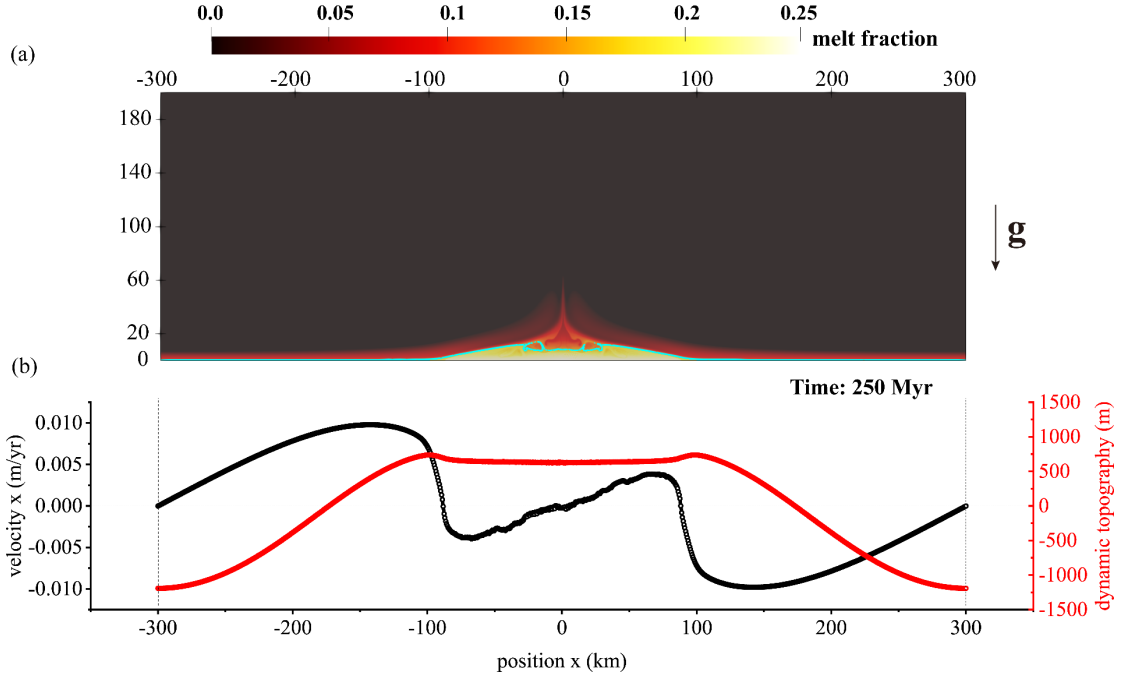

Figure 3. (a) Melt fraction of the reference model (ρ_{melt} - ρ_{solid} = +300 kg·m^3) 250 Myr after the initial condition (which is the time when the subsequent experimental model boundary parameters start to change). The blue line is the same as in Figure 2. (b) Model tangential velocity (black, along x-direction) and dynamic topography (red) distribution on the bottom boundary (CMB) at 250 Myr; note, we use the normal stress σ_{rr} as the equivalent for dynamic topography $h=\sigma_{rr}/[(\mathbf{g}\cdot\mathbf{n})\cdot(\rho-\rho_{core})]$) (Bangerth et al., 2022; Mckenzie et al., 1974). The model is, within numerical errors, symmetric with aspect to its centerline, with velocities and topography mirrored with respect to x=0.

The subsequent model boundary setting is based on the following.

2.3.1 Bottom boundary temperature

As mentioned in section 1, considering the heat-mass exchange at the CMB, we introduced the influence exerted by a cold source, such as subducting/subducted plates in the mantle, by setting a nonuniform mantle-bottom temperature boundary in the following model. Given that several ULVZs are located in seismic cold zones and at the edges of the Pacific or Afro-Atlantic LLSVPs (Garnero & McNamara, 2008), this suggests the presence of long-lasting cold sources. According to previous estimates of the lateral temperature variation in the lowermost mantle, the peak temperature difference between the mantle plume base and the surrounding lower mantle is not expected to be greater than 500 K (Davies et al., 2015; Deschamps & Li, 2019; Solomatov & Moresi, 2002; WATSON & McKENZIE, 1991). Although the lateral temperature variation at the top of the outer core does not exceed ~1 K (Mound et al., 2019), considering the stronger heat exchange within the outer core (owing to high thermal conductivity) than in the mantle, and in reference to the ±100 K setting found in previous work (Aubert et al., 2007), we set the peak lateral temperature difference between cold source location and normal ambient mantle at the bottom boundary to be 0, -100, -200, and -300 K. This would result in both a cooling effect on the local ambient mantle outside the mantle plume and cooling of the plume itself within a few tens of kilometers (<50 km) of the plume edge (Figure S1).

2.3.2 Bottom boundary velocity

For the velocity boundary, as in previous studies, we set a velocity-free-slip bottom boundary in the reference model (Figure 3). Under the zero-shear stress assumption, this leads to a CMB velocity generated entirely by mantle convection and gravitational action. However, previous studies have shown that this cannot sufficiently explain the high-density ULVZ morphology distribution (Section 1). Therefore, in the following section, we introduce other factors that contribute to the CMB velocity. Previous observations have revealed that dense material piles within the plume spontaneously form an internal reverse circulation, allowing the mantle flow along the CMB to

converge at the edge of the plume (Kellogg & King, 1993; Luo et al., 2001; McNamara, 2019). The drag force driven by the CMB topography, as well as the net horizontal electromagnetic force from the outer core (Dehant et al., 2022; Glane & Buffett, 2018), may affect the internal reverse circulation.

In the first part of this study (Section 3.1), our reference model, utilizing the CMB dynamic boundary conditions (BCs) of zero flow-through and zero shear stress, found a self-consistent convecting-mantle flow that contained and produced a dynamically consistent mantle velocity field at the CMB. In the second part (after Section 3.1), we prescribed/imposed Dirichlet BCs on the mantle velocity field at the CMB.

For this Dirichlet velocity field, we firstly note that the velocity distribution and speeds of the mantle mass elements at the CMB and the proper Dirichlet boundary velocity field, although seemingly somewhat arbitrary or artificial, are based on the dynamically consistent mantle flow computed in the reference model. Therefore, this CMB-mantle Dirichlet velocity field adequately imitates the resulting velocity field of a system in which the velocity is a consequence of self-consistent pressure and viscous forces operating during convection, that is, the convecting-mantle pressure field and viscous field horizontal forces move the mantle-CMB mass particles at those velocities. Thus, in principle, our second-part model contains Dirichlet boundary velocities that are approximately consistent with the reasonable model settings.

Additionally, if externally driven velocities are considered, the liquid iron outer core may exert forces on the lowermost mantle, affecting its velocity field. We quickly review that (a) the CMB topography and (b) possible magnetic forces can potentially have non-negligible effects on the velocity field at the mantle CMB.

Here, we varied the bottom tangential traction to experiment with how large a force source is required to produce localized CMB-mantle flow velocities of a magnitude comparable to the lower mantle characteristic convective speed (~1 cm/yr (Flament et al., 2017)). The bottom boundary traction model simulations show that to reach velocities of that magnitude, based on the outer-core-flow drag force formula in plane laminar flow $F_{drag} = c_D \frac{\rho}{2} u^2 bl$ (Schlichting & Gersten, 2017), where at a modest

Reynolds number (Re~10^7–10^8), considering outer-core parameters η=0.01 Pa·s, u=5×10^{-4} m/s (Jones, 2015), and l as the half plume width, the drag force must be increased by a factor of 10^5 (Figure S2). The core-mantle mass exchange layer (a region where chemical exsolution is upward from the outer core and downward from the mantle, and accumulated material may reside for different amounts of time) at the uppermost outer core beneath the CMB may have a higher viscosity, and the resulting local drag effect is facilitated by CMB topography. Given length l of x × 10^1–10^2 km, and taking drag coefficient $c_D = 24/Re$ at a small Reynolds number (< 10^3) where $F_{drag} = 12\eta ul$, a sufficient non-essential condition is that the thin mass exchange layer viscosity could reach 10^3–10^5 Pa·s (an intermediate value between outer-core and lowermost mantle).

Based on these considerations, in the subsequent parts of this study, we established a Dirichlet-type velocity BC at the CMB, whose horizontal-component distribution is prescribed to have the form of the velocity distribution obtained in the free-slip-BC simulation (Figure 3) and zero in the vertical y-direction, meaning that this Dirichlet velocity field simulates the resultant velocity field dynamically obtained from the tangential BC, which is consistent with the internal reverse circulation and, furthermore, with the CMB dynamic topography. Naturally, applying traction ('Neumann' BC for velocity) at the bottom boundary produces somewhat different results than applying "Dirichlet" BC for velocity (see the bottom horizontal velocity in Figures 3b and S2). Comparison of model outputs having different types of bottom conditions for the velocity field, as seen for example in the aforementioned figures, shows differences in melt morphology between those pertaining to prescribed traction and/or velocity BC models (Figure S3).

However, to focus on the direct effects of CMB-mantle flow, we begin with the model of applied horizontal velocity that is more closely aligned with the reference free-slip-BC model.

2.4. Other model settings

To maintain calculation stability at the beginning of modeling, we divided the simulation process into two stages (Dannberg et al., 2021). In the initial stage of 0–150

Myr, we prevented melt migration from occurring by increasing the melt scaling factor (10^{20}, equivalent to virtually reducing the permeability coefficient to 0) and allowed the mantle plume to form under the initial temperature perturbation. We applied melt migration in the second stage (i.e., a smaller melt scaling factor of 10^{-8}) when the average temperature and average velocity reached a steady state. The minimum size of the model grid is 781 m × 781 m after eight adaptive refinements, and the minimum total time step is ~7000–13000 yr, the melting (migration) time step is 1000 yr, which satisfies reasonable resolution requirements of ULVZs.

We briefly summarize the idealizations and simplifications we adopted for the models in this study: (a) We utilized the bottom boundary conditions to represent our conceptual framework rather than explicitly introducing the cold subducted plates and the underlying dense liquid outer core. (b) To evaluate different boundary conditions, we employed simplified material properties associated with the melt migration model. We then compared the findings of our model with those of an unsimplified property (Dannberg) model under the same boundary conditions. (c) We utilized a 2D symmetric (along x=0) model; thus, our discussion of boundary conditions effects does not cover asymmetric outcomes; although this limits the discussion, it allows a simpler dynamics for easy understanding.

3. Results

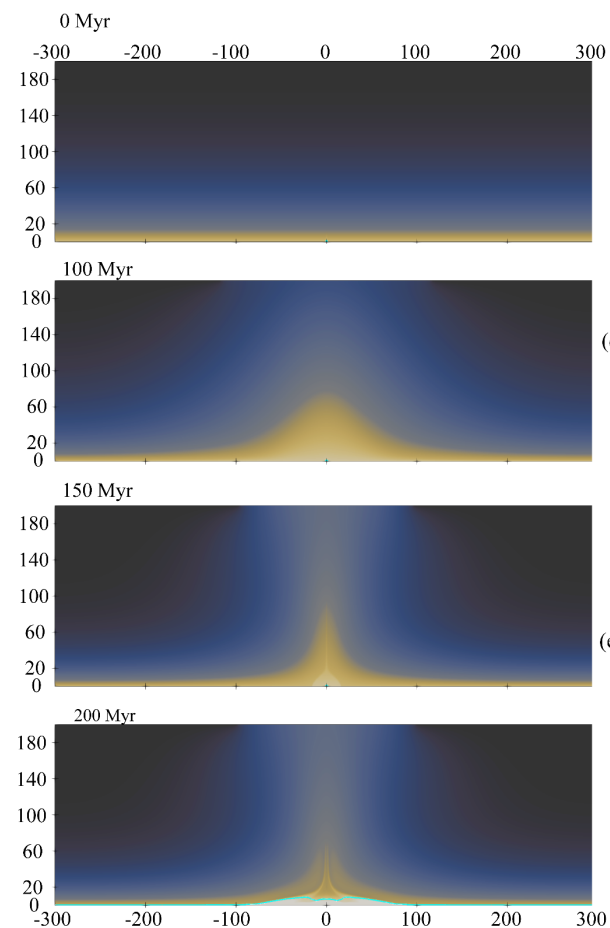### 3.1. Impact of melt-solid mass-density difference on melt formation

First, we compared the "Dannberg" model with our reference model while simplifying the material model (Figures 2 and 3) in order to control variables. We then compared the results of the reference model with those of the subsequent experimental model with modified bottom boundary conditions.

We refer to the model with the simplified material parameters, tangential flow, and constant temperature bottom boundary as "ref" in Figure 2. The binary melt system with the same bottom boundary is referred to as "Dannberg" (Dannberg et al., 2021).
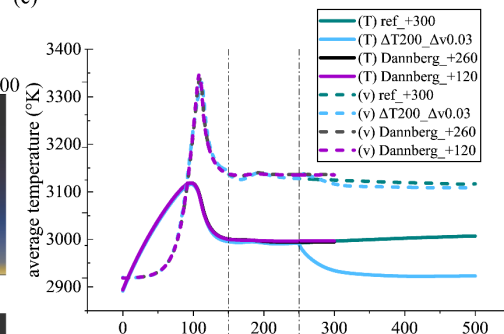
Experimental model "ΔT200_Δv0.03" depicts the model with a modified bottom boundary, whose lateral extent and velocity distribution (with direction-and-sense) are

identical to those obtained in the reference model (Figure 3), in which the CMB-mantle mass moves away from the center within the mantle plume and towards the center outside; in model "ΔT200_Δv0.03," these velocities are Dirichlet-prescribed. The peak temperature difference between the cold source location and the normal ambient mantle was -200 K ($T_{bottom, peak}$-$T_{bottom, ambient}$), and the peak horizontal velocity was 3 cm/yr (i.e., 30 km/Myr) (v_{peak}). The specific distributions along the bottom boundary are shown in Figure 7d and 7b.
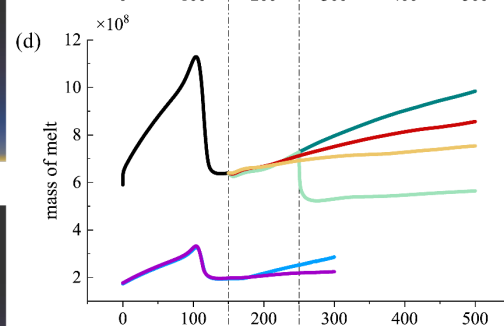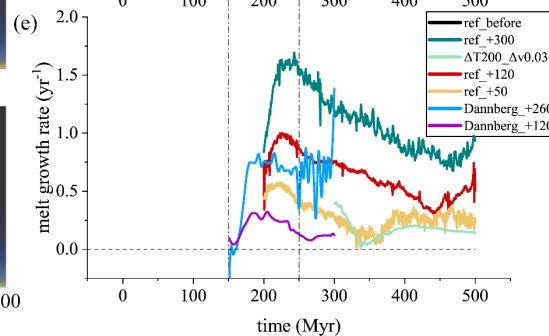
(a)

0 Myr

100 Myr

150 Myr

200 Myr

(c)

(d)

(e)

(b)

500 Myr $\Delta\rho = +300$ kg/m³

500 Myr $\Delta\rho = +120$ kg/m³

500 Myr $\Delta\rho = +50$ kg/m³

shear viscosity (Pa·s)

1e+18   5e+18 1e+19   5e+19 1e+20   5e+20 1e+21   5e+21 1e+22   1e+23

density (kg/m³)

5400   5450   5500   5550   5600   5650   5700

(c) legend:
- (T) ref_+300
- (T) ΔT200_Δv0.03
- (T) Dannberg_+260
- (T) Dannberg_+120
- (v) ref_+300
- (v) ΔT200_Δv0.03
- (v) Dannberg_+260
- (v) Dannberg_+120

average temperature (°K)

root mean square velocity (m/yr)

mass of melt $\times 10^8$

(e) legend:
- ref_before
- ref_+300
- ΔT200_Δv0.03
- ref_+120
- ref_+50
- Dannberg_+260
- Dannberg_+120
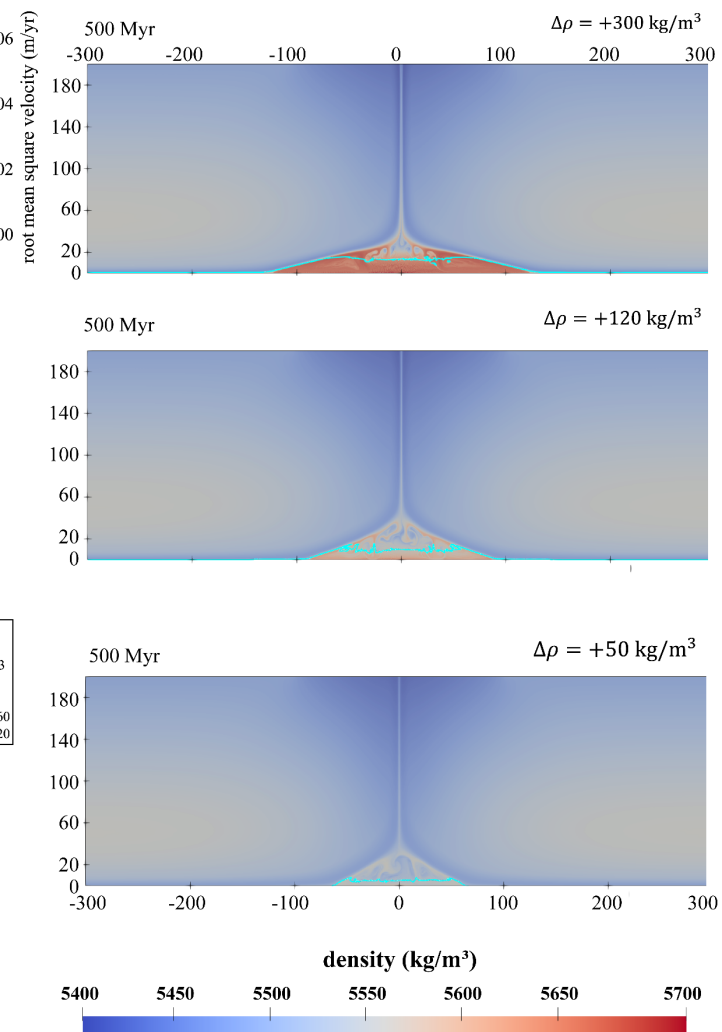
melt growth rate (yr⁻¹)

time (Myr)

Figure 4. Comparison of the results for different melt-solid density difference models. (a) Reference model evolution shown by shear viscosity distribution, blue contour is the same as in Figure 3. **(b) Reference model comparison of the melt-solid density differences $\Delta\rho$** (ρ_{melt} - ρ_{solid} = +50, +120, and +300 kg·m^{-3}) at the simulated end time (500 Myr), shown by density distribution ($\bar{\rho}$= (1-ϕ) ρ_{solid} + $\phi\rho_{\text{melt}}$, where ϕ is the melt fraction), blue contour as in Figure 3. Center column: **Evolution of (c) the average velocity (right axis), average temperature (left axis) over the entire study area, (d) total melt mass, and (e) melt growth rate.** The number after the model name represents the melt-solid density difference (kg·m^{-3}). "ref" represents the reference model (Figure 3), "ref_before" is the stage before melt migration (150 Myr), "Dannberg" is the model from (Dannberg et al., 2021), "ΔT200_Δv0.03" is the experimental model with the density difference of 300 kg·m^{-3} and the non-uniform constant bottom boundary, with ΔT = $T_{\text{bottom,peak}}$-$T_{\text{bottom, ambient}}$ = -200 K and Δv = $v_{\text{bottom, peak}}$ = 0.03 m/yr. The detailed distribution is shown in Figure 7d and 7b. We choose the melt growth rate of "Dannberg_+120" as the criteria to evaluate whether the melt has reached stability in Figure 6.

Figure 4a shows the evolution of the shear viscosity field for model "ref+300". The low-viscosity melt was initially generated at the bottom of the plume and then spread to the sides after melt migration occurred, as shown by the yellow backdrop and blue contour. Figure 4b displays the melt density distribution (density $\bar{\rho}= (1\text{-}\phi)\,\rho_{solid} + \phi\rho_{melt}$, where ϕ is the melt fraction) for different density differences ($\Delta\rho = \rho_{melt} - \rho_{solid}$) of the "ref" model at the simulated end time (500 Myr). As the melt-solid density difference increased, the red high-density melt structure became increasingly wider on the sides. Similar to the findings of previous studies, a smaller positive density difference makes it easier for it to be entrained in the rising mantle flow, and the negative-density melt allows it to ascend through the mantle without accumulating at its base (Garnero & McNamara, 2008).

Except for the total amount of melt (Figure 4d), the results of our reference model versus the "Dannberg" model reveal no significant difference (Figure 4c). Figure 4c depicts the evolution of the average velocity and temperature over the entire study area. The mantle flow in the model no longer varied considerably following the development of the mantle plume (150 Myr, black dashed line on the left); however, the average temperature decreased after the bottom cold source was applied (250 Myr, black dashed line on the right). Figure 4d shows the results of total melt mass growth over time. Our reference and "Dannberg" models both show that the smaller the density difference, the easier the melt stabilizes.

Although the total melt mass obtained from the "ref" model ended as 4–5 times greater than that obtained from the "Dannberg" model, it does not affect our study of their melt variation tendencies (Figure 4d and 4e). In addition, using the stable "Dannberg (+120)" shown in purple as a baseline, we see that the melt of the "ref (+50)" with lower positive density difference, as well as experimental model "$\Delta T200\_\Delta v0.03$" with a cold source and bottom tangential flow, eventually reaches stability. Then, we take the melt growth rate of "Dannberg (+120)" as the criteria for evaluating whether the melt has reached stability in Section 4.1.

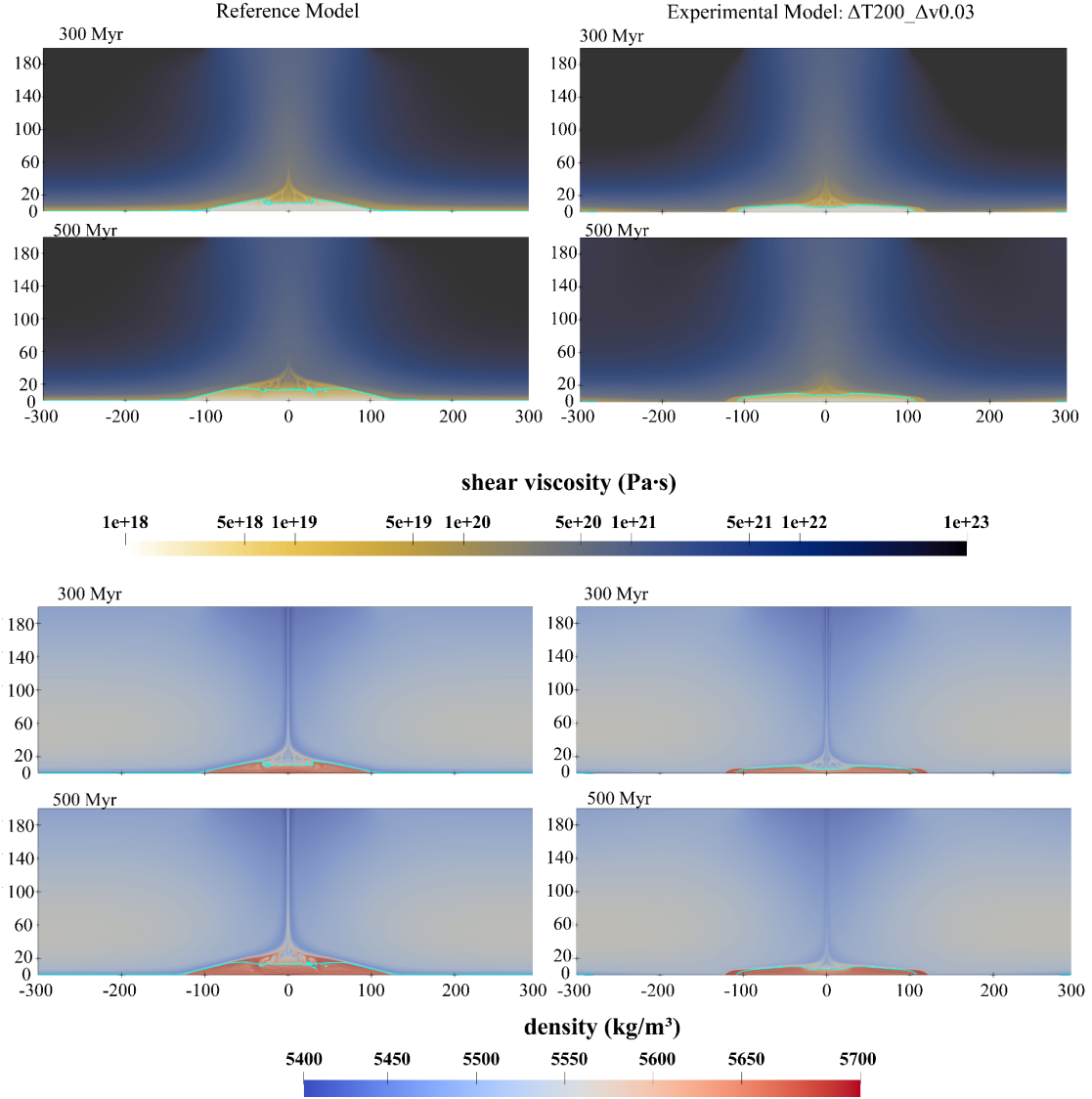## 3.2. Impact of the bottom boundary setup on melt morphology

Figure 5. Comparison of the reference and experimental model at 300 and 500 Myr, shown by shear viscosity (top) and mass density (bottom). "ref_+300" model (left column) and "ΔT200_Δv0.03" (right column) are the same as Figure 4, and the blue line as in Figure 3. In the right-column (prescribed Dirichlet-type velocity bottom boundary condition), the high-density, low-viscosity melt region has a flatter top and steeper edges than the left-column reference model.

Figure 5 depicts the model density and shear viscosity distributions without (left) and with (right) changes in the bottom boundary conditions at two instants, revealing that after the application of the cold source and bottom tangential flow, the model produces a melt with sharp edges and flat tops similar to those observed in seismic data (Rost et al., 2005, 2006), whereas the aspect ratio of the melt layer increases in the latter.

Previous interpretations of the steep edges of the LLSVP and ULVZs have emphasized the pushing effect of the subduction plate with mantle flow (Davies et al., 2015; John William Hernlund & Bonati, 2019). Our findings indicate that the thermal effect of the subduction plate as a cold source between it and the ULVZs is sufficient to generate a melt layer with sharp edges in which the internal tangential flow, enhanced by the CMB topography and the uppermost outer core, also plays a significant role.

4. Discussion

4.1. Stable conditions for high-density melts

We assumed that the conditions of this distribution near the edge of the LLSVPs allowed for lengthy durations of existence (> 100 Myr), as mentioned in Section 2.3. Hence, in this section, the boundary values remained constant during the parametric analysis. To explore the influence of varying bottom temperature and velocity parameters on the melt growth rate, we fixed the melt-solid density difference at +300 kg·m^{-3}, as shown in Figure 6.
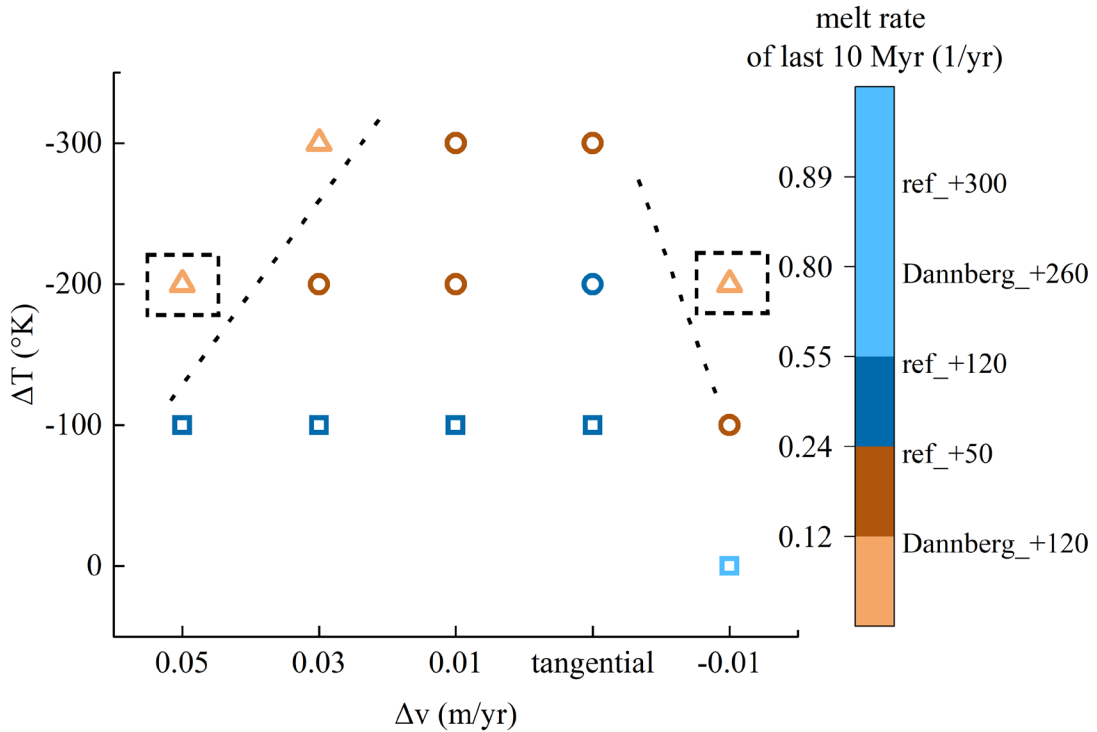

Figure 6. Phase diagram of melt growth-rate for the model bottom boundary setups. The model mass-density differences (ρ_{melt} - ρ_{solid}) are fixed at +300 kg·m^{-3}. ΔT is the peak value of the applied bottom temperature difference, between the 'cold-source' and the ambient

($\Delta T = T_{\text{bottom,peak}} - T_{\text{bottom, ambient}}$), separated by horizontal distance of approximately 100 km and defines the rows in the plot. Δv represents the peak value of applied bottom-boundary velocity (Dirichlet-type) ($\Delta v = v_{\text{bottom, peak}}$) and defines the columns in the plot. Note that for comparison, we replaced "$\Delta v=0$" with a **tangential** (Neumann-type) velocity boundary as in the reference model (Figure 3). Each element represents one single simulation. Colors indicate the average melt growth rate within 10 Myr before the simulated end time (500 Myr). The symbols in the right-side legend indicate the classification criteria derived from the reference model results (Figure 4e). The category of melt-stability discrimination: Orange triangles indicate that model melt reached a stable state (top left and right corners), blue rectangles indicate unstable states and brown circles are transition state models. The simulations enclosed by dashed-line squares are used in Figure 7.

In Figure 6, the vertical coordinates represent the lateral temperature difference peaks between a mantle neighboring cold source and normal ambient mantle ($\Delta T = T_{\text{bottom,cold peak}} - T_{\text{bottom, ambient}}$) of 0, -100, -200, and -300 K. The horizontal axis indicates the velocity setup (Dirichlet-type) with positive labels for flow in the same direction of the tangential flow model (Neumann-type) (Figure 3), with maximum values ($\Delta v = v_{\text{bottom, peak}}$) of 0.01, 0.03, and 0.05 m/yr, and a single negative value of -0.01 m/yr (meaning flow in the opposite direction to that of reference). The melt growth rate for the last 10 Myr of the simulation is represented by the colors in Figure 6 and is depicted in Figure 4e. The categorization criteria for determining whether the melt reaches stability are presented in the legend. Based on previous studies (Dannberg et al., 2021; John W. Hernlund & Jellinek, 2010) and the melt results in Figure 4d and 4e, we used the melt rates of the "Dannberg+120" and "ref+50" models as the cut-off.

This indicates that the melt stabilization zone lies in the upper left positive-flow-velocity region and the upper right negative-flow-velocity region of the phase diagram. Thus, the greater the temperature differences and velocity when the velocity direction is the same as the "ref" model (positive), the easier the melt stabilizes. Additionally, a maximum velocity of 0.01 m/yr can stabilize the melt when the velocity is reversed (negative). The cold source reduced the melt fraction, and the CMB-mantle tangential flow increased the cooling effectiveness. Furthermore, stronger flow facilitates the migration of the melt towards localized "cooling zone." In the absence of a cold source,

strong bottom tangential flow cannot stabilize the melt. To stabilize a melt that has a higher density (ρ_{melt} - ρ_{solid} > 50–120 kg·m^{-3}), a cold source is necessary, with the corresponding lateral temperature difference between ~4000 K at the plume central regions to <~3900 K at the plume-cooling intermediate mantle region, separated by horizontal distances of ~100 km (approximately as shown in Figure 7).

When the density difference between the solid and melt is approximately ~+10% ((ρ_{melt}-ρ_{solid})/ρ_{solid}), the stable presence of melt still requires a cold source with a temperature difference absolute value >100 K (Table 3). However, the melt growth rate decreased for the same boundary setup when the density difference approached approximately 10%, indicating that the lower limit of the boundary conditions relaxed for additional increases in the density difference. We speculate that this may be because the Rayleigh number (Ra = $\rho g \alpha \Delta T h^3/(\eta \kappa)$) increases further through the density, which denotes enhanced local convection within the ULVZs and morphology stability of the melt.

Table 3. Model melt growth rate [a] comparison regarding the melt-solid density difference (ρ_{melt} - ρ_{solid} = +300, +500 kg·m^{-3}) under different bottom boundary conditions (Figure 6).

Density difference +300 kg·m^{-3}		
Bottom boundary condition	0.05 m/yr	0.03 m/yr	0.01 m/yr
---	---	---	---
-300 K		**0.107**	0.125
-200 K	**0.109**	0.147	0.208
-100 K	0.291	0.331	0.425
Density difference +500 kg·m^{-3}		
Bottom boundary condition	0.05 m/yr	0.03 m/yr	0.01 m/yr
-300 K	**0.057**	**0.064**	**0.080**
-200 K	**0.109**	**0.111**	0.158
-100 K	0.362		0.426

[a] The stable (bolded) upper limit of the growth rate is the same as Figure 6 ("Dannberg_+120" model: ~0.12 yr^{-1}).

4.2. Morphological characteristics of the stabilized melt

Because both positive and negative velocities can mechanically stabilize the melt, as described in Section 4.1, we selected the two models "ΔT200_Δv0.05" and "ΔT200_Δv-0.01" ringed by dashed circles in Figure 6 to study the differences in the generated melt morphology.

(a)

ΔT200_Δv-0.01

500 Myr

melt fraction

0   0.05   0.1   0.15   0.2   0.25

ΔT200_Δv0.05

500 Myr

(b)

velocity x (m/yr)

Δv0.05
Δv-0.01
ΔT200

(c)

dynamic topography (m)

(d)

melt fraction

temperature (°K)

(e)

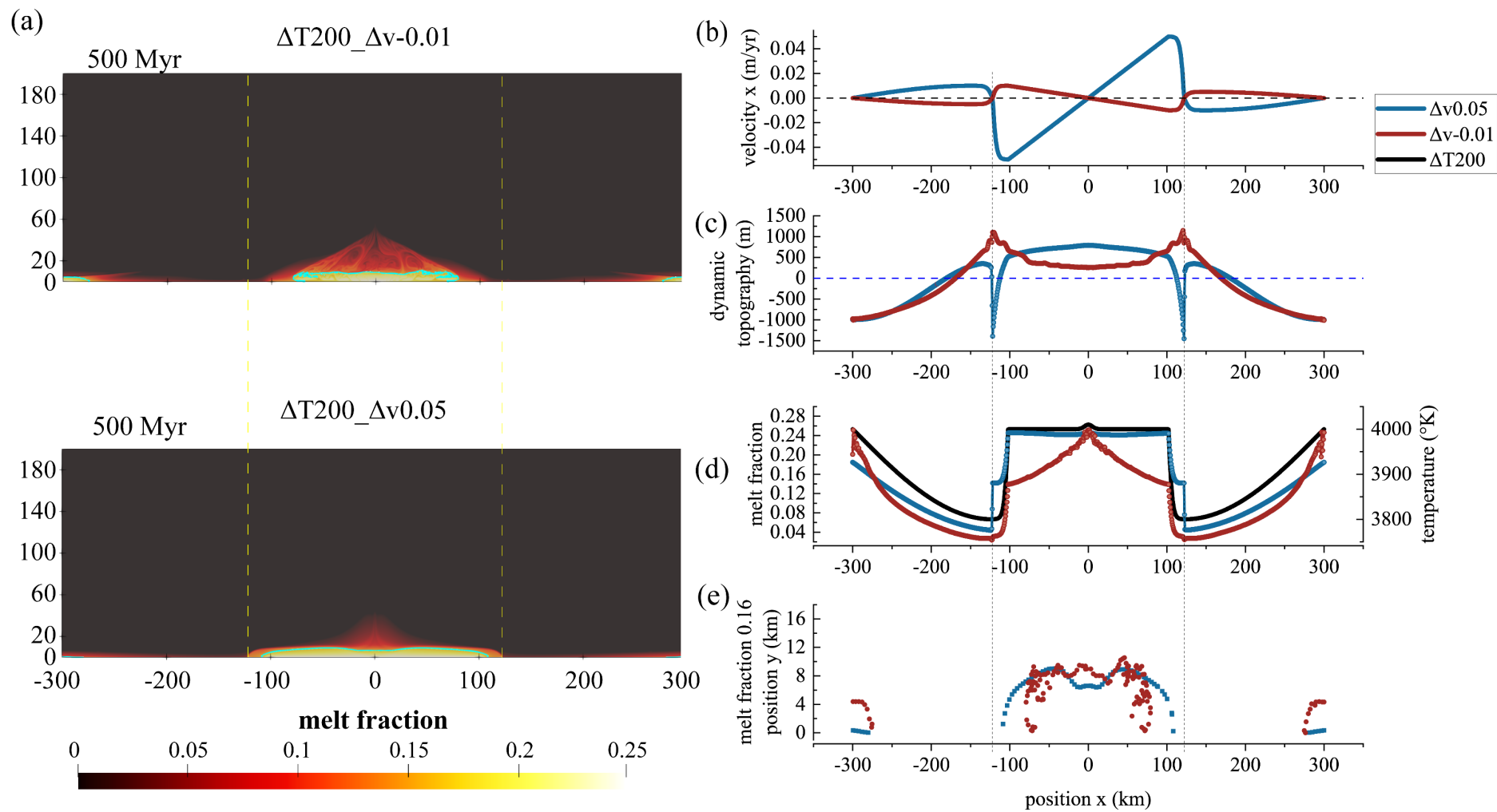melt fraction 0.16 position y (km)

position x (km)

Figure 7. Example model results illustrating the effect of the applied bottom velocity direction, distinguished and indicated by dashed-line squares in Figure 6. Symbol "-" indicates that the direction is opposite to the reference model (Figure 3). **(a) Model melt fraction at the simulated end time (500 Myr)**, blue line is the same as in Figure 3. **(b) Applied bottom horizontal velocity distribution**, **(c) model bottom dynamic topography** ($h=\sigma_{rr}/[(\mathbf{g}\cdot\mathbf{n})\cdot(\rho-\rho_{core})]$, where σ_{rr} is the normal stress), **(d) model bottom melt fraction (left) and applied bottom temperature distribution (right)** ($\Delta T = -200$ °K, Figure 6), **and (e) spatial distribution of the fixed melt fraction (0.16)**. Dark blue model: The bottom horizontal velocity peak value (Δv, Figure 6) is 0.05 m/yr, and the velocity direction within the plume is away from the center (same as the reference model, Figure 3). Brown model: The velocity is 0.01m/yr, and the direction within the plume is towards to the center (opposite of the reference model). The melt morphology of the dark blue model is more consistent with the seismic constraints.

Figure 7a shows the melt fraction distributions for both models at the end of the simulation (500 Myr). Figure 7b–d depict the results for the tangential velocity at the bottom boundary of the model, CMB dynamic topography, melt fraction, and applied temperature. The horizontal and vertical axes in Figure 7e are spatial coordinates indicating the contour spatial distribution for a melt fraction of 0.16. The dashed lines represent the location of ULVZ/plume edges.

The edge of the melt layer, where the mantle flow meets because of an abrupt change in the velocity direction (Figure 7b), is the area of lower melt degree depicted in Figure 7a. However, compared with the smoother border of the negative model, the edge of positive model is steeper. The dynamic topography in Figure 7c similarly reflects this sharp edge; however, the negative model lacks this feature, whereas the positive model exhibits a local topographic jump with an amplitude of 1–2 km comparable to the total value. The melt fraction depicted in Figure 7d decreased towards the edges because of the applied cold-source temperatures and thermal diffusion. In particular, the melt fraction in the model decreased by ~10% within a few kilometers, corresponding to the melt density variation and gradually increasing dynamic topography (Figure 7c). Finally, the melt fraction distribution (Figure 7a, e) shows that the lateral extent and aspect ratio of the melt layer of the positive model were substantially larger, and the top region of its low-melt-fraction zone was flatter than that of the negative model.

More specifically, studies of long-wavelength topography have demonstrated the contribution of the LLSVP to lower mantle flow (Heyn et al., 2020; Lassak et al., 2010), and our results show that when the ULVZs are engaged, the topography undulations are shorter horizontally (~20 km) and more pronounced vertically (~1–2 km). Previous study has estimated that a 1% melt corresponds to a shear wave velocity reduction of approximately 2.5% (Dannberg et al., 2021). Therefore, owing to the cold source presence, there may be a "cooling zone" for the plume (with strong lateral heat flux), with a ~10% lateral variation in shear wave velocity at the plume edge with a slightly lower melting degree. In summary, the melt layer morphologies produced by models with bottom velocities in the same direction as the internal reverse circulation were

more consistent with seismic observations (Rost et al., 2005). The local variation in the lateral melt fraction and the higher local topographic jump (gradient) at the plume edge were the main features of this model.

We then conducted a parameter analysis, as illustrated in Figure 8, to compare the precise impacts of various model bottom conditions on the ULVZ morphology (aspect ratio).
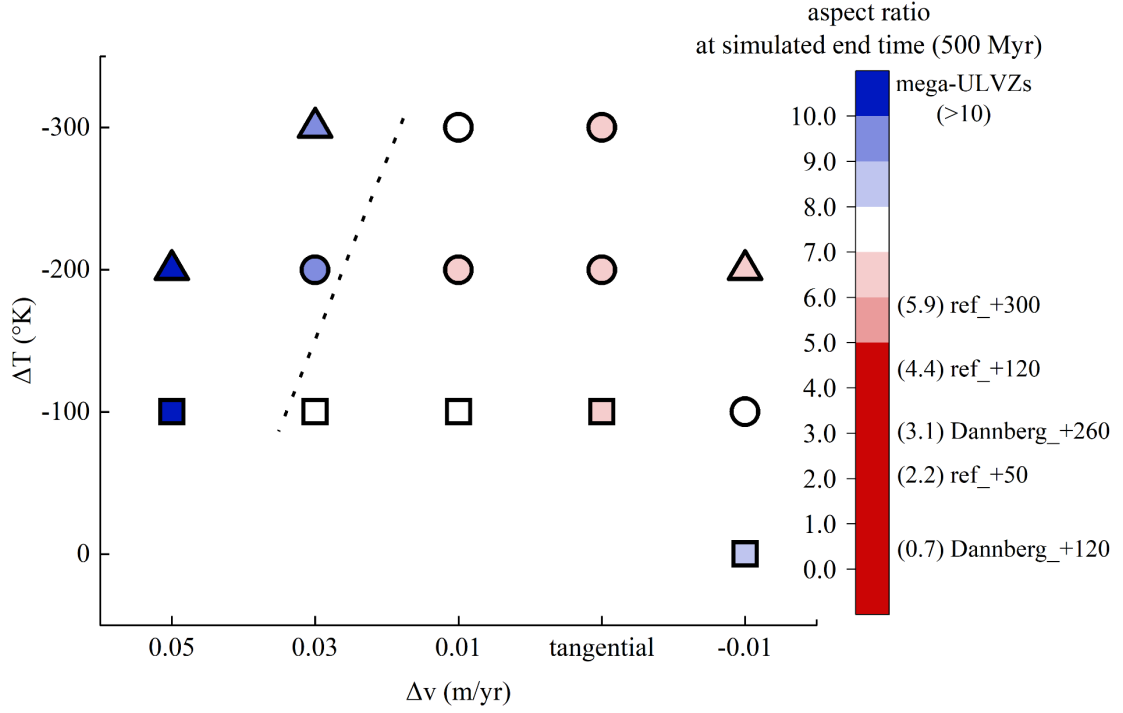

Figure 8. Phase diagram of melt aspect ratio for the model bottom boundary setups. The model density difference and plot symbols are the same as in Figure 6. *Aspect ratio* = (width / height) $_{melt}$. *Melt width*: horizontal distance (left-side) from the model center to location where melt fraction contour (0.1) vertical-thickness reaches 5 km. *Melt height*: the height of the fixed melt fraction (0.1) in the model center. Colors indicate the melt aspect ratio at the simulated end time (500 Myr). The right side legend symbols show the aspect ratio of the reference models (Figure 3) and the mega-ULVZs (Figure 1 and Table 1). The aspect ratios of the reference models are ≤6 (legend right), whereas all models with changed bottom boundary setup are >6 (background). The aspect ratios of top left area models are more consistent with the seismic observational constraints.

As in Figure 6, the horizontal and vertical axes in Figure 8 represent the boundary conditions, and the symbols indicate whether the melt is stable. The color in the figure represents the melt aspect ratio at the end of the simulation. We take the height of the central melt fraction 0.1 as the ULVZ height, and the distance from the model center to

the (left) location where the thickness of melt fraction 0.1 reaches 5 km as the ULVZ width. Therefore, the aspect ratio is defined as the melt width/melt height. Because the "Dannberg" model produces less melt, the melt fraction is set to 0.16, and the thickness limit is set at 1 km.

The reference model results (Figure 5) are shown on the right side of the legend. The melt aspect ratios of these bottom tangential flow models are <6, and the smaller the density difference, the lower the aspect ratio and the more "towering" the melt region, which is consistent with the results in Section 3.1. The aspect ratios of the models with the modified bottom conditions were all >6, and the larger the velocity magnitude, the flatter the melt region in the positive model. This suggests that a stronger bottom tangential flow can suppress a wider range of mantle flows above the CMB, allowing the upper melt layer to have a greater lateral scope.

As mentioned in Table 1, the aspect ratios of the mega-ULVZs shown at the top of the legend are substantially larger (>10). Based on the thickness (5–40 km) and lateral extent ($x \times 10^2 – 10^3$ km) of the ULVZs observed, the majority had an aspect ratio of >5. Therefore, if the simulation results are comparable to the seismic observations, the high-density melt must be coupled to the bottom local CMB-mantle flow, where the flow velocity is in the same direction as the internal reverse circulation. Moreover, the magnitude of flow velocity is related to the morphology of the melt.

4.2.1 Other factors affecting melt morphological characteristics

In the previous sections, the peak value position of the applied cold source, approximately 100 km from the mantle plume center, was fixed. First, we considered the effect of the location of the cold source on the chemical stability of the melt. We then adjusted the distance from the peak value position of the applied cold source to the plume center, specifically, 50 km closer to and farther from the center. As a result, compared to the "$\Delta T200\_\Delta v0.03$" model in Figure 5, the melt growth rates of the different models have the following range: no cold source > cold source 50 km farther from the center > cold source -100 K at the same position > cold source 50 km closer to the center > cold source -200 K ("$\Delta T200\_\Delta v0.03$") (Figure S4). It can be observed

that the cold source, both too close and too far from the plume center, increases the melt growth rate (unstable trend).

In terms of the dynamic topography of the CMB, the distant cold source (+50 km) mitigated the impacts of local topographical undulation near the edge of the plume. In contrast, a nearby cold source (-50 km) extends the lateral extent of the undulation, with minimal effect on the maximum topographical leap amplitude. In terms of melt morphology, the sharp-edged and flat-topped melt layer features vanish as the cold source advances further from the mantle plume (+50 km). Conversely, as the cold source approaches (-50 km), the smaller low-melting degree melt zones emerge at the plume edge (Figure S5). However, the high-melting morphology at the bottom of the plume, is less affected by the nearby cold source.

As a result, the "cooling zone" for the plume must continue to be involved in the melt stabilization process. However, if the cold source is too close, it changes the low-melting morphology at the base of the plume, increasing the two edges and severely lowering the center (Figure S5).

In addition, we investigated the impact of positive and negative Clapeyron-slopes on the "$\Delta T200\_\Delta v0.03$" model results. We changed the initial melt state parameters in Table 2 such that the melt layers in the positive and negative slope models had approximately the same thickness (~15 km) at the beginning of the modeling process (Table S1). The findings demonstrate that a negative Clapeyron slope flattens the central low-melting zone but has no impact on the total melt mass and melt growth rate at the simulated end time (Clapeyron-slope+: 0.152 yr^{-1}, Clapeyron-slope-: 0.147 yr^{-1}) (Figure S6), nor does it have an impact on the dynamic topography of the CMB and its high-melting morphology (Figure S7).

4.3. CMB dynamical environment implied by the ULVZs morphology

Furthermore, based on the dynamic conditions described in the previous sections, we evaluated the characteristics of the bottom flow field from the ULVZs morphology. We previously applied a constant bottom velocity constraint, which is partly consistent with the morphological properties of the melt system once it reaches thermochemical-

mechanical stability. In this section, the bottom tangential velocity is dynamically determined using the topographic horizontal gradient.

First, the bottom dynamic topography was calculated using the normal stress, specifically, its perturbations with respect to the reference adiabatic regime hydrostatic pressure:

$$\sigma_{rr} = \hat{g}^T \left(2\eta \left(\varepsilon(\boldsymbol{u}) - \frac{1}{3}(\nabla \cdot \boldsymbol{u})\boldsymbol{I} \right) \right) \hat{g} - p_d \tag{9}$$

where $p_d = p - p_{adiabatic}$, and $\hat{g} = \frac{\boldsymbol{g}}{\|\boldsymbol{g}\|}$.

The dynamic topographic is

$$h = \frac{\sigma_{rr}}{(\rho - \rho_{core})(\boldsymbol{g} \cdot \boldsymbol{n})} \tag{10}$$

where $\rho_{core} = 9900$ kg/m^3 (Dziewonski & Anderson, 1981).

We referred to the equation used to calculate the normal infiltration rate in the "Lim" model (Lim et al., 2021), in which the topographic gradient was used to calculate the tangential velocity as follows:

$$v = c \cdot \frac{\Delta\rho(\boldsymbol{g} \cdot \boldsymbol{n})}{12\eta} \cdot \nabla_x^2 h^4 \tag{11}$$

where c represents the dimensionless scaling factor.

We used $\Delta T = 0$ K and $\Delta v < 0.02$ m/yr at the initial stage (250 Myr, consistent with the setup in Figure 4) because a greater "Δv" results in numerical instability here. Because of the absence of a cold source, the melted layer did not exhibit chemical stability. The results of the opposing horizontal velocity (x) direction models are displayed in Figure 9, where "reference-consistent" indicates horizontal velocity x away from the center in the interior of the plume (consistent with the reference model in Figure 3), and "reference-opposite" indicates horizontal velocity x towards the center within the plume.

Specifically, at the simulated end time (500 Myr), "reference-consistent" was slightly smaller (0.92) than the "ref_+300" model, and "reference-opposite" was roughly equal to (1.00) the "ref_+300" model. The generated melt layer also exhibited a lower aspect ratio. Here, we focused on the evolution and duration of some melt features.
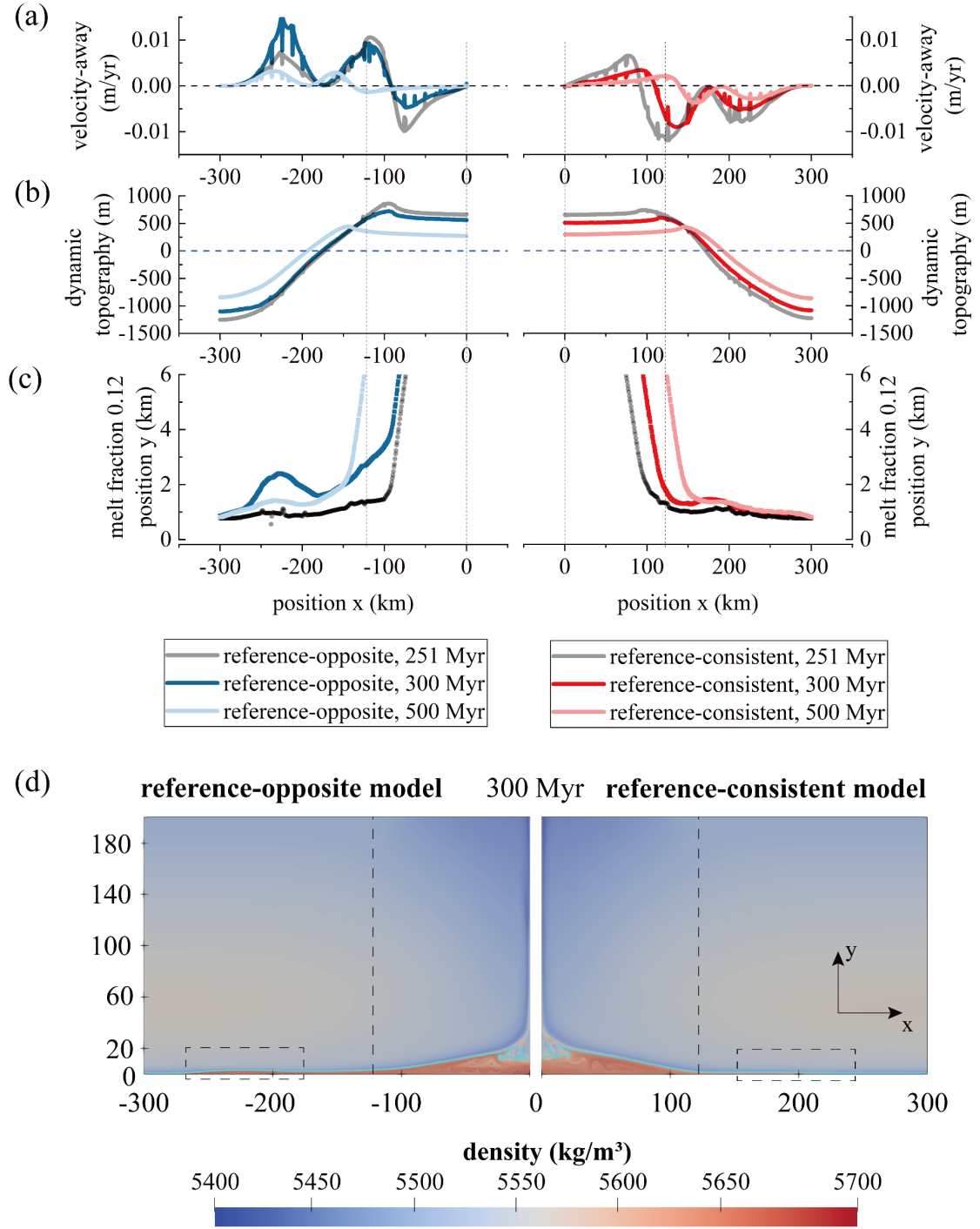
Figure 9. Model evolution results of topography-coupled bottom velocity boundary at 251 (gray, the beginning of the setup), 300 (dark color), and 500 Myr (light color). *Reference-consistent*: red, horizontal velocity (x) direction is applied away from the center within the plume, same with reference model (Figure 3). *Reference-opposite*: blue, horizontal velocity (x) direction is applied towards the center within the plume. **(a) Bottom horizontal velocity (x) distribution** (>0: away from the plume center, <0: towards the plume center)**, (b) model bottom dynamic topography,** and **(c) the spatial distribution of the fixed melt fraction (0.12). (d) Model mass-density at 300 Myr** (density $\bar{\rho} = (1-\phi)\rho_{solid} + \phi\rho_{melt}$, where ϕ is the melt fraction), and the blue line is the same as in Figure 3. To reduce the disturbances of numerical

errors, for panels (a, b, c) and for each model we center x = 0 km and take averages (arithmetic mean) of the values of the variables from both sides about x=0; then, we plot them on the right side of the "reference-consistent" model and on the left side of the "reference-opposite" model respectively. (d) Black dashed-line boxes indicate a possible "melt bulge" area outside the plume in the "reference-opposite" model (left), virtually absent in the "reference-consistent" model.

Figure 9a represents the bottom tangential velocity (>0: away from the plume center, <0: towards the plume center) evolution, and the velocity at the side boundaries is still artificially suppressed. In contrast to the previous model distribution, there are locations outside the plume where the velocity drops to zero under the combined influence of the topography and topographic gradient.

To reduce the influence of numerical errors, we center on vertical axis x = 0 km, average the values on both sides (Figure 9a–c); later, for the figure plots, we show the right side of "reference-consistent" and the left side of "reference-opposite" (Figure 9d). The results reveal that, owing to the larger topographic gradient, the velocity near the plume edge (dashed vertical line) can be maintained for at least 50 Myr (250–300 Myr), whereas the velocity values were reduced in other areas. As for the later stage (300–500 Myr), the results demonstrated that the bottom velocity values rapidly increased at locations of high strain rate, causing the melt layer to spread towards the outside of the plume (Figure 9d), leading to a decrease in local velocity within the plume (Figure 9a), the local topography becoming smooth (Figure 9b), and the spatial distribution of the melt increasing (Figure 9c). We believe that (a) a lack of the cold source causes outward expansion of the melt layer with plume edge movement and (b) the bottom flow velocity with simple constant scaling factor c in equation (11), both of which lead to the decay of the velocity magnitude within the plume at this stage.

Notably, the area away from the plume in the "reference-opposite" model (-250 to -200 km in Figure 9c) forms the smaller "melt bulge." Even if we intentionally suppressed the mantle velocity outside the plume close to the side boundaries, a "melt bulge" still occurred. Finally, as the simulation progresses (300–500 Myr), the dynamic topography value decreases due to the continuous growth of the melt to both sides (Figure 9b), resulting in a decrease in the bottom velocity magnitude (Figure 9a) and

the height of the "melt bulge."

The "reference-consistent" modeling results partially indicate the dynamical environment around the hot mantle plume area, validating our "Dirichlet" boundary setup described in the previous sections. However, to understand the "reference-opposite" model findings, we must start with the conceptual model. The dynamic environments of the cold-downwelling zone and ascending mantle plume are opposite, and under gravitational action, the opposite mantle flow produces opposite CMB dynamic topography. Because the topographic gradients under these regions can be comparably strong and long lasting, the CMB-mantle flow can be significantly influenced by the uppermost core flow, and the flow field direction may be opposite to that of the regional mantle flow (Figure 10). Then a CMB-mantle "opposite" flow and corresponding boundary layer may exist over several kilometers of thickness, resulting in larger local viscous stress.

Therefore, the outer-plume region of the "reference-opposite" model may indicate the CMB-mantle flow near the cold zone, and the "melt-bulge" (found in the simulation) may correspond to the ULVZs in the cold zone. By suppressing the above-adjacent mantle flow near the cold-downwelling zone, the CMB-mantle flow (in opposition) may also contribute to the creation of ULVZs. However, because the outer core cannot be properly recreated in our modeling, the "reference-opposite" model itself cannot provide robust evidence of the process, meaning a self-consistent mechanism for the generation of locally high stress that can contribute to the ULVZs development in cold zone.

Furthermore, how did the low-velocity material originate to form in the "cold zone?" For the constant-in-time velocity model, which is applied with constant extended cold source ($\Delta T = -100$ K) and tangential velocity setup (as in the "reference-opposite" model, $\Delta v = 0.01$ m/yr), the result shows that the similar appearance of the "melt bulge" outside of the plume (Figure S8). The reduced melt fraction decreased the resulting melt-solid density difference, which reduced the CMB-mantle tangential flow velocity allowed by a gravitationally more stable structure. It ultimately lowers the length-scale and magnitude of "low wave-velocity anomaly." Our further validation of the low-

velocity material sources of partial melting in the cold zone is limited by the simplified material properties of the model, such as linear solidus-liquidus. However, previous research indicates that the liquid core material can penetrate the CMB in the downwelling flow region, although the resulting "mushy layer" thickness is ~1 km (Kanda & Stevenson, 2006; Lim et al., 2021). If the local CMB-mantle flow is involved, the initial formation melt may thicken into a "low-velocity zone," as shown in the model in this section. In general, owing to limitations of the temperature and topographic gradient, the range of ULVZs developed here is narrower than that in the plume region, which may explain why certain ULVZs and "low-velocity layer" appear in the "cold zone," as shown in Figure 1 (Fan et al., 2022; Yu & Garnero, 2018) (Figure 10). Compared with ULVZs formed near the superplume edge, ULVZs in the cold zone have a smaller scale and less lateral variation in seismic-wave velocity, which can be verified by geophysical observations.

Finally, we have discussed the mechanisms of melt stabilization at the plume edge and in the cold zone. However, the localized denser melts, detected by seismic observations at the bottom center of the plume, may not be "controlled" by the CMB-mantle flow due to small CMB-topographic gradients and may continue to accumulate and grow until the lateral extent extends to a sufficiently cooled zone, where P-T conditions limit the amount of melt and preclude further melt growth-advancement, by melt-solid equilibration. From our reference modeling results (Figures 5 and 8), during this process, larger melt heights and smoother-edge ULVZ morphologies were likely the main characteristics.
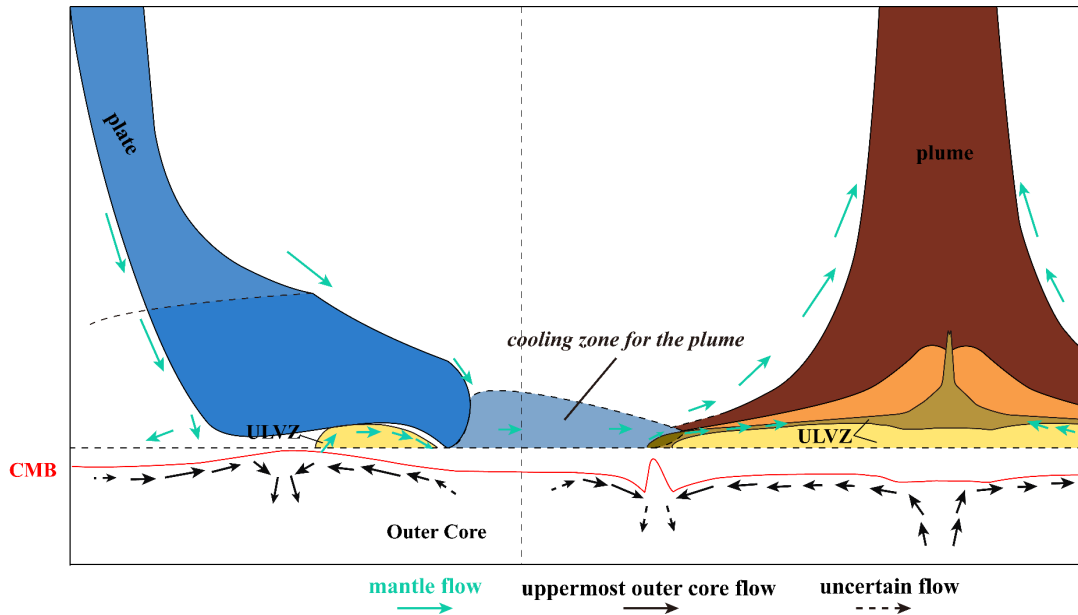
Figure 10. Schematic representation of the model conclusions. The subdomain on the right side from the vertical dashed line indicates the study area in our model, and the left side indicates the presumed environment involved in the cold downwelling. Note, the near-bottom dashed horizontal line is a simple referential CMB for ease of plotting, where the **red solid line** depicts a dynamic CMB responding to this plume-and-plate environment. **Dark brown**: the mantle plume, **orange tones**: the melting layer with increasing melt degrees (darker), **blue**: the cold subduction plate (solid line), and the high-velocity layer of the resulting cold source (dashed line). The melt fraction is lower at the area where the "cooling zone" meets the edge of the plume. **Yellow**: ULVZs, occur at the base of the plume and in areas with large CMB topographic gradients of the "cold zone". **Cyan arrows**: lowermost mantle flow direction, **black solid arrows**: flow direction near the CMB and at the uppermost outer core, **black dashed arrows**: core flow with assumed direction.

4.4. Model limitations

Our model is simplified using a 2D geometrical description and by having a constant distribution coefficient of Fe and Mg between the solid and liquid phases, as well as a linear solidus-liquidus equation curve. It was chosen to isolate the effect of the bottom boundary conditions on melt generation and speed up the simulations to compare different model setups. This simplification may lead to inaccuracies related to the following.

(1) Compared to a 3D model, the 2D model we introduced neglects heat transfers in the 3rd direction and likely underestimates the plume heat losses. Furthermore, 2D Dirichlet velocity BC would require mostly exaggerated drag forces on the CMB to

generate the tangential velocity consistent with the magnitude of the lowermost mantle flow.

(2) Compared to the "Dannberg" model, the material properties we used exaggerate the total melt mass; to avoid this, we focused on the melt growth rate and the aspect ratio of melt morphology.

(3) We did not explore the effect of viscosity. However, previous studies indicated that the height of ULVZ is not sensitive to its viscosity (Beuchert & Schmeling, 2013), and whether viscosity affects the melt morphology in the edge area requires further study.

(4) We did not directly or explicitly model the mechanical interaction between the subducting plates and ambient mantle, nor the intercoupling between the subducting plates and the low-viscosity outer core because of numerical stability limitations and to conveniently isolate the basic controlling factors. Instead, we applied different bottom boundary conditions at a certain time, which led to the resulting evolution of the ULVZs differing slightly from the corresponding geological evolution of the real Earth.

To focus on the specific problem, most of the discussion in this study is based on our numerical models, which are symmetric about x = 0. In future studies, based on the asymmetric model results (Figure S3), different scales, extents, and locations of cold sources and/or CMB-mantle flows should be considered and purposely applied to the left or right side to examine asymmetric scenarios that are closer to the real Earth.

5. Conclusions

(1) The stable existence and residence of high-density ((ρ_{melt}-ρ_{solid})/ρ_{solid} >+1–2%, reaching ~+10%) melt requires, in the scenario we studied, the participation of a cold source, and corresponding lateral temperature differences between ~4000 K at the plume central regions to <~3900 K at the plume-cooling intermediate mantle region, separated by horizontal distances of about 100 (±<50) km. The plume-cooling intermediate region is the region where heat flows from the hot plume base (at the center of our model) towards a neighboring cold source (not explicitly modeled in our settings), such as a subducted plate that advects cold isotherms from the surface (Figure 10); a configuration that may last for several hundred million years with respect to mantle

viscosities and thermal diffusivities.

(2) To obtain ULVZ results with a high aspect ratio that matches seismic observations, high-density melt requires the participation of a CMB-mantle flow that is oriented with internal reverse circulation of/inside the plume broad basal region. Furthermore, the fluid dynamics of this problem dictate that the magnitude of the velocity is related to the melt liquid-body morphology. The ULVZ morphology with a flat top and sharp edge necessitates local CMB-mantle flow horizontal speeds of approximately >3 times the characteristic convective speed of the lower mantle (~1 cm/yr), which can be attained by episodic mantle forces and/or outer core interactions (favored by CMB topography that enhances resistance and coupling of the flow stresses, and potentially/eventually magnetic forces).

(3) The local CMB-mantle flow facilitated by the CMB topography interacting with the outer core may be important (and perhaps crucial) in developing mega-ULVZs, particularly when the latter is spread or located near the edges of a superplume, phenomena that may be transient in mantle evolution of the Earth. Our point of view is related to the fact that seismic-observations studies discovered ULVZs in certain "cold zones" with higher seismic-wave speeds. However, their lateral extents were smaller owing to the limitations of temperature and topographic gradient amplitude.

Data Availability Statement

Our modeling results, ASPECT input file and plugin are available at (https://zenodo.org/records/10006400). Version 2.4.0 of the numerical software ASPECT used for modeling is available via https://zenodo.org/record/6903424, the visualization software ParaView is available via https://www.paraview.org/. Figure 1 is plotted with GMT https://www.generic-mapping-tools.org/.

References

Aubert, J., Amit, H., & Hulot, G. (2007). Detecting thermal boundary control in surface flows from numerical dynamos. *Physics of the Earth and Planetary Interiors*, *160*(2), 143–156. https://doi.org/10.1016/j.pepi.2006.11.003

Bangerth, W., Dannberg, J., Fraters, M., Gassmoeller, R., Glerum, A., Heister, T., et al. (2022, July 25). ASPECT v2.4.0. Zenodo. https://doi.org/10.5281/zenodo.6903424

Beuchert, M. J., & Schmeling, H. (2013). A melting model for the lowermost mantle using Clapeyron slopes derived from experimental data: Consequences for the thickness of ultralow velocity zones (ULVZs). *Geochemistry, Geophysics, Geosystems*, *14*(1), 197–208. https://doi.org/10.1029/2012GC004356

Boukaré, C.-E., Ricard, Y., & Fiquet, G. (2015). Thermodynamics of the MgO-FeO-SiO2 system up to 140 GPa: Application to the crystallization of Earth's magma ocean. *Journal of Geophysical Research: Solid Earth*, *120*(9), 6085–6101. https://doi.org/10.1002/2015JB011929

Brandon, A. D., & Walker, R. J. (2005). The debate over core–mantle interaction. *Earth and Planetary Science Letters*, *232*(3), 211–225. https://doi.org/10.1016/j.epsl.2005.01.034

Buffett, B. (2014). Geomagnetic fluctuations reveal stable stratification at the top of the Earth's core. *Nature*, *507*(7493), 484–487. https://doi.org/10.1038/nature13122

Buffett, B. (2016). Another energy source for the geodynamo. *Nature*, *529*(7586), 288–289. https://doi.org/10.1038/529288a

Cottaar, S., Martin, C., Li, Z., & Parai, R. (2022). The root to the Galápagos mantle plume on the core-mantle boundary. *Seismica*, *1*(1). https://doi.org/10.26443/seismica.v1i1.197

Dannberg, J., & Heister, T. (2016). Compressible magma/mantle dynamics: 3-D, adaptive simulations in ASPECT. *Geophysical Journal International*, *207*(3), 1343–1366. https://doi.org/10.1093/gji/ggw329

Dannberg, J., Myhill, R., Gassmöller, R., & Cottaar, S. (2021). The morphology, evolution and seismic visibility of partial melt at the core–mantle boundary: implications for ULVZs. *Geophysical Journal International*, *227*(2), 1028–1059. https://doi.org/10.1093/gji/ggab242

Davies, D. R., Goes, S., & Lau, H. C. P. (2015). Thermally Dominated Deep Mantle LLSVPs: A

Review. In A. Khan & F. Deschamps (Eds.), *The Earth's Heterogeneous Mantle: A Geophysical, Geodynamical, and Geochemical Perspective* (pp. 441–477). Cham: Springer International Publishing. https://doi.org/10.1007/978-3-319-15627-9_14

Dehant, V., Campuzano, S. A., De Santis, A., & van Westrenen, W. (2022). Structure, Materials and Processes in the Earth's Core and Mantle. *Surveys in Geophysics*, *43*(1), 263–302. https://doi.org/10.1007/s10712-021-09684-y

Deschamps, F., & Li, Y. (2019). Core-Mantle Boundary Dynamic Topography: Influence of Postperovskite Viscosity. *Journal of Geophysical Research: Solid Earth*, *124*(8), 9247–9264. https://doi.org/10.1029/2019JB017859

Dobson, D. P., & Brodholt, J. P. (2005). Subducted banded iron formations as a source of ultralow-velocity zones at the core–mantle boundary. *Nature*, *434*(7031), 371–374. https://doi.org/10.1038/nature03430

Dziewonski, A. M., & Anderson, D. L. (1981). Preliminary reference Earth model. *Physics of the Earth and Planetary Interiors*, *25*(4), 297–356. https://doi.org/10.1016/0031-9201(81)90046-7

Fan, A., & Sun, X. (2021). Origin of ULVZs near the African LLSVP: Implications from their distribution and characteristics. *Earthquake Science*, *34*(4), 299–309. https://doi.org/10.29382/eqs-2021-0042

Fan, A., Sun, X., Zhang, Z., Zhang, P., & Zong, J. (2022). From Subduction to LLSVP: The Core-Mantle Boundary Heterogeneities Across North Atlantic. *Geochemistry, Geophysics, Geosystems*, *23*(1), e2021GC009879. https://doi.org/10.1029/2021GC009879

Fearn, D. R., & Loper, D. E. (1981). Compositional convection and stratification of Earth's core. *Nature*, *289*(5796), 393–394. https://doi.org/10.1038/289393a0

Flament, N., Williams, S., Müller, R. D., Gurnis, M., & Bower, D. J. (2017). Origin and evolution of the deep thermochemical structure beneath Eurasia. *Nature Communications*, *8*(1), 14164. https://doi.org/10.1038/ncomms14164

Garnero, E. J., & McNamara, A. K. (2008). Structure and Dynamics of Earth's Lower Mantle. *Science*, *320*(5876), 626–628. https://doi.org/10.1126/science.1148028

Garnero, E. J., Revenaugh, J., Williams, Q., Lay, T., & Kellogg, L. H. (1998). Ultralow Velocity Zone at the Core-Mantle Boundary. In *The Core-Mantle Boundary Region* (pp. 319–334).

American Geophysical Union (AGU). https://doi.org/10.1029/GD028p0319

Garnero, E. J., McNamara, A. K., & Shim, S.-H. (2016). Continent-sized anomalous zones with low seismic velocity at the base of Earth's mantle. *Nature Geoscience*, *9*(7), 481–489. https://doi.org/10.1038/ngeo2733

Glane, S., & Buffett, B. (2018). Enhanced Core-Mantle Coupling Due to Stratification at the Top of the Core. *Frontiers in Earth Science*, *6*. Retrieved from https://www.frontiersin.org/article/10.3389/feart.2018.00171

Hansen, U., & Yuen, D. A. (1988). Numerical simulations of thermal-chemical instabilities at the core–mantle boundary. *Nature*, *334*(6179), 237–240. https://doi.org/10.1038/334237a0

Helffrich, G., & Kaneshima, S. (2010). Outer-core compositional stratification from observed core wave speed profiles. *Nature*, *468*(7325), 807–810. https://doi.org/10.1038/nature09636

Hernlund, J. W., & McNamara, A. K. (2015). 7.11 - The Core–Mantle Boundary Region. In G. Schubert (Ed.), *Treatise on Geophysics (Second Edition)* (pp. 461–519). Oxford: Elsevier. https://doi.org/10.1016/B978-0-444-53802-4.00136-6

Hernlund, John W., & Jellinek, A. M. (2010). Dynamics and structure of a stirred partially molten ultralow-velocity zone. *Earth and Planetary Science Letters*, *296*(1), 1–8. https://doi.org/10.1016/j.epsl.2010.04.027

Hernlund, John W., & Tackley, P. J. (2007). Some dynamical consequences of partial melting in Earth's deep mantle. *Physics of the Earth and Planetary Interiors*, *162*(1), 149–163. https://doi.org/10.1016/j.pepi.2007.04.005

Hernlund, John William, & Bonati, I. (2019). Modeling Ultralow Velocity Zones as a Thin Chemically Distinct Dense Layer at the Core-Mantle Boundary. *Journal of Geophysical Research: Solid Earth*, *124*(8), 7902–7917. https://doi.org/10.1029/2018JB017218

Heyn, B. H., Conrad, C. P., & Trønnes, R. G. (2020). Core-mantle boundary topography and its relation to the viscosity structure of the lowermost mantle. *Earth and Planetary Science Letters*, *543*, 116358. https://doi.org/10.1016/j.epsl.2020.116358

Jenkins, J., Mousavi, S., Li, Z., & Cottaar, S. (2021). A high-resolution map of Hawaiian ULVZ morphology from ScS phases. *Earth and Planetary Science Letters*, *563*, 116885. https://doi.org/10.1016/j.epsl.2021.116885

Jensen, K. J., Thorne, M. S., & Rost, S. (2013). SPdKS analysis of ultralow-velocity zones beneath

the western Pacific. *Geophysical Research Letters*, *40*(17), 4574–4578. https://doi.org/10.1002/grl.50877

Jones, C. A. (2015). 8.05 - Thermal and Compositional Convection in the Outer Core. In G. Schubert (Ed.), *Treatise on Geophysics (Second Edition)* (pp. 115–159). Oxford: Elsevier. https://doi.org/10.1016/B978-0-444-53802-4.00141-X

Kanda, R. V. S., & Stevenson, D. J. (2006). Suction mechanism for iron entrainment into the lower mantle. *Geophysical Research Letters*, *33*(2). https://doi.org/10.1029/2005GL025009

Kellogg, L. H., & King, S. D. (1993). Effect of mantle plumes on the growth of D" by reaction between the core and mantle. *Geophysical Research Letters*, *20*(5), 379–382. https://doi.org/10.1029/93GL00045

Koelemeijer, P., Ritsema, J., Deuss, A., & van Heijst, H.-J. (2016). SP12RTS: a degree-12 model of shear- and compressional-wave velocity for Earth's mantle. *Geophysical Journal International*, *204*(2), 1024–1039. https://doi.org/10.1093/gji/ggv481

Labrosse, S., Hernlund, J. W., & Coltice, N. (2007). A crystallizing dense magma ocean at the base of the Earth's mantle. *Nature*, *450*(7171), 866–869. https://doi.org/10.1038/nature06355

Lassak, T. M., McNamara, A. K., Garnero, E. J., & Zhong, S. (2010). Core–mantle boundary topography as a possible constraint on lower mantle chemistry and dynamics. *Earth and Planetary Science Letters*, *289*(1), 232–241. https://doi.org/10.1016/j.epsl.2009.11.012

Lay, T., Hernlund, J., & Buffett, B. A. (2008). Core–mantle boundary heat flow. *Nature Geoscience*, *1*(1), 25–32. https://doi.org/10.1038/ngeo.2007.44

Li, M., McNamara, A. K., Garnero, E. J., & Yu, S. (2017). Compositionally-distinct ultra-low velocity zones on Earth's core-mantle boundary. *Nature Communications*, *8*(1), 177. https://doi.org/10.1038/s41467-017-00219-x

Li, Z., Leng, K., Jenkins, J., & Cottaar, S. (2022). Kilometer-scale structure on the core–mantle boundary near Hawaii. *Nature Communications*, *13*(1), 2787. https://doi.org/10.1038/s41467-022-30502-5

Lim, K. W., Bonati, I., & Hernlund, J. W. (2021). A Hybrid Mechanism for Enhanced Core-Mantle Boundary Chemical Interaction. *Geophysical Research Letters*, *48*(23), e2021GL094456. https://doi.org/10.1029/2021GL094456

Luo, S.-N., Ni, S., & Helmberger, D. V. (2001). Evidence for a sharp lateral variation of velocity at

the core–mantle boundary from multipathed PKPab. *Earth and Planetary Science Letters*, *189*(3), 155–164. https://doi.org/10.1016/S0012-821X(01)00364-8

McKENZIE, D. (1984). The Generation and Compaction of Partially Molten Rock. *Journal of Petrology*, *25*(3), 713–765. https://doi.org/10.1093/petrology/25.3.713

Mckenzie, D. P., Roberts, J. M., & Weiss, N. O. (1974). Convection in the earth's mantle: towards a numerical simulation. *Journal of Fluid Mechanics*, *62*(3), 465–538. https://doi.org/10.1017/S0022112074000784

McNamara, A. K. (2019). A review of large low shear velocity provinces and ultra low velocity zones. *Tectonophysics*, *760*, 199–220. https://doi.org/10.1016/j.tecto.2018.04.015

McNamara, A. K., & Zhong, S. (2005). Thermochemical structures beneath Africa and the Pacific Ocean. *Nature*, *437*(7062), 1136–1139. https://doi.org/10.1038/nature04066

McNamara, A. K., Garnero, E. J., & Rost, S. (2010). Tracking deep mantle reservoirs with ultra-low velocity zones. *Earth and Planetary Science Letters*, *299*(1), 1–9. https://doi.org/10.1016/j.epsl.2010.07.042

Mound, J., Davies, C., Rost, S., & Aurnou, J. (2019). Regional stratification at the top of Earth's core due to core–mantle boundary heat flux variations. *Nature Geoscience*, *12*(7), 575–580. https://doi.org/10.1038/s41561-019-0381-z

Olson, P., Landeau, M., & Reynolds, E. (2017). Dynamo tests for stratification below the core-mantle boundary. *Physics of the Earth and Planetary Interiors*, *271*, 1–18. https://doi.org/10.1016/j.pepi.2017.07.003

O'Rourke, J. G., & Stevenson, D. J. (2016). Powering Earth's dynamo with magnesium precipitation from the core. *Nature*, *529*(7586), 387–389. https://doi.org/10.1038/nature16495

Otsuka, K., & Karato, S. (2012). Deep penetration of molten iron into the mantle caused by a morphological instability. *Nature*, *492*(7428), 243–246. https://doi.org/10.1038/nature11663

Pachhai, S., Li, M., Thorne, M. S., Dettmer, J., & Tkalčić, H. (2022). Internal structure of ultralow-velocity zones consistent with origin from a basal magma ocean. *Nature Geoscience*, *15*(1), 79–84. https://doi.org/10.1038/s41561-021-00871-5

Ricard, Y. (2015). 7.02 - Physics of Mantle Convection. In G. Schubert (Ed.), *Treatise on Geophysics (Second Edition)* (pp. 23–71). Oxford: Elsevier. https://doi.org/10.1016/B978-

0-444-53802-4.00127-5

Rost, S., Garnero, E. J., Williams, Q., & Manga, M. (2005). Seismological constraints on a possible plume root at the core–mantle boundary. *Nature*, *435*(7042), 666–669. https://doi.org/10.1038/nature03620

Rost, S., Garnero, E. J., & Williams, Q. (2006). Fine-scale ultralow-velocity zone structure from high-frequency seismic array data. *Journal of Geophysical Research: Solid Earth*, *111*(B9). https://doi.org/10.1029/2005JB004088

Rost, S., Garnero, E. J., & Stefan, W. (2010). Thin and intermittent ultralow-velocity zones. *Journal of Geophysical Research: Solid Earth*, *115*(B6). https://doi.org/10.1029/2009JB006981

Schlichting, H., & Gersten, K. (2017). *Boundary-Layer Theory*. Berlin, Heidelberg: Springer. https://doi.org/10.1007/978-3-662-52919-5

Solomatov, V. S., & Moresi, L.-N. (2002). Small-scale convection in the D″ layer. *Journal of Geophysical Research: Solid Earth*, *107*(B1), ETG 3-1-ETG 3-10. https://doi.org/10.1029/2000JB000063

Stein, C., Mertens, M., & Hansen, U. (2020). A numerical study of thermal and chemical structures at the core-mantle boundary. *Earth and Planetary Science Letters*, *548*, 116498. https://doi.org/10.1016/j.epsl.2020.116498

Sun, D., Helmberger, D., Lai, V. H., Gurnis, M., Jackson, J. M., & Yang, H.-Y. (2019). Slab Control on the Northeastern Edge of the Mid-Pacific LLSVP Near Hawaii. *Geophysical Research Letters*, *46*(6), 3142–3152. https://doi.org/10.1029/2018GL081130

Thorne, M. S., Garnero, E. J., Jahnke, G., Igel, H., & McNamara, A. K. (2013). Mega ultra low velocity zone and mantle flow. *Earth and Planetary Science Letters*, *364*, 59–67. https://doi.org/10.1016/j.epsl.2012.12.034

Vanacore, E. A., Rost, S., & Thorne, M. S. (2016). Ultralow-velocity zone geometries resolved by multidimensional waveform modelling. *Geophysical Journal International*, *206*(1), 659–674. https://doi.org/10.1093/gji/ggw114

van Tent, R., Deuss, A., Kaneshima, S., & Thomas, C. (2020). The signal of outermost-core stratification in body-wave and normal-mode data. *Geophysical Journal International*, *223*(2), 1338–1354. https://doi.org/10.1093/gji/ggaa368

WATSON, S., & McKENZIE, D. (1991). Melt Generation by Plumes: A Study of Hawaiian

Volcanism. *Journal of Petrology*, *32*(3), 501–537. https://doi.org/10.1093/petrology/32.3.501

Yu, S., & Garnero, E. (2017). ULVZ Distribution Database from 54 studies [Data set]. Zenodo. https://doi.org/10.5281/zenodo.1064217

Yu, S., & Garnero, E. J. (2018). Ultralow Velocity Zone Locations: A Global Assessment. *Geochemistry, Geophysics, Geosystems*, *19*(2), 396–414. https://doi.org/10.1002/2017GC007281

Yuan, K., & Romanowicz, B. (2017). Seismic evidence for partial melting at the root of major hot spot plumes. *Science*, *357*(6349), 393–397. https://doi.org/10.1126/science.aan0760

Zhao, C., Garnero, E. J., Li, M., McNamara, A., & Yu, S. (2017). Intermittent and lateral varying ULVZ structure at the northeastern margin of the Pacific LLSVP. *Journal of Geophysical Research: Solid Earth*, *122*(2), 1198–1220. https://doi.org/10.1002/2016JB013449